Winter 2001

Ensemble Monte Carlo Based Simulation Analysis of GaN HEMTs for High-Power Microwave Device Applications

Tao Li
Old Dominion University

ENSEMBLE MONTE CARLO BASED SIMULATION ANALYSIS OF GAN HEMTS FOR HIGH POWER MICROWAVE DEVICE APPLICATIONS

by

Tao Li
B. S. University of Electronic Science & Technology of China (UESTC)
M. S. University of Electronic Science & Technology of China (UESTC)

A Dissertation submitted to the Faculty of
Old Dominion University in Partial Fulfillment
Of the Requirement for the Degree of

DOCTOR OF PHILOSOPHY

ELECTRICAL ENGINEERING

OLD DOMINION UNIVERSITY

December 2001

Approved by

Ravindra P. Joshi (Director)

Duc T. Nguyen (Member)

Linda L. Vahala (Member)

ABSTRACT

ENSEMBLE MONTE CARLO BASED SIMULATION ANALYSIS OF
GAN HEMTS FOR HIGH POWER MICROWAVE DEVICE APPLICATIONS

Tao Li
Old Dominion University, 2001
Director: Dr. Ravindra P. Joshi

The high electron mobility transistors (HEMTs) fabricated using wide-bandgap semiconductors show promise as high-gain, low-noise devices with superior frequency response. The structure and operation principle of HEMT are first briefly discussed. The distinguishing and unique properties of GaN are reviewed and compared with those of GaAs. Calculations of the electronic mobility and drift velocity have been carried out for bulk GaN based on a Monte Carlo approach, which serves as a validity check for the simulation model.

By taking account of polarization effects, degeneracy and interface roughness scattering, important microwave performance measures such as the dynamic range, harmonic distortion and inter-modulation characteristics are fully studied. Monte Carlo based calculations of the large-signal nonlinear response characteristics of GaN-AlGaN HEMTs with particular emphasis on intermodulation distortion (IMD) have been performed. The nonlinear electrical transport is treated on first principles, including all scattering mechanisms. Both memory and distributed effects are built into the model. The results demonstrate an optimal operating point for low intermodulation distortion (IMD) at reasonably large output power due to the exist of a minima in the IMD curve. Dependence of the nonlinear characteristics on the barrier mole fraction "x" is also

demonstrated and analyzed. High-temperature predictions of the IMD have also been made by carrying out the simulations at 600 K. Due to a relative suppression of interface roughness scattering, an increase in dynamic range with temperature is predicted.

Finally, towards the end of the research, real-space transfer (RST) phenomena are included in the Monte Carlo simulator to accurately describe the electron transport behavior in HEMTs. The RST is shown to affect the velocity overshoot and inter-modulation distortion behavior and to lead to enhanced substrate leakage current as well as lowered overall performance speed. The potential for drain current compression has also been examined through simulations. Comparisons with and without RST have been performed based on Monte Carlo simulations. Results show that the velocity, IMD and dynamic range are all affected by the applied bias, temperature, internal electric field and gate length characteristics.

ACKNOWLEDGMENTS

I am immensely grateful to my advisor, Dr. R. P. Joshi, for his valuable academic guidance and encouragement throughout the course of this study. His insight and wisdom greatly inspired me. To a great extent, my work ethic has been shaped by his professionalism, an invaluable example to me. I would also like to thank my research committee members, Dr. Linda L. Vahala and Dr. Duc T. Nguyen, for their review and valuable comments.

Great thanks to Dr. James Liu at Filtronic Solid State for his concern and ever-available support, which made it possible to finish the dissertation.

I would like to thank my parents for their supports both emotionally and financially. They gifted me not only intelligence, health, perseverance, but also the courage to pull through difficulties.

Special thanks to my best friends, Dr. Bo Jiang and Ms. Hong Sun. Their lifelong friendship and great faith in my ambition always light up my life.

TABLE OF CONTENTS

LIST OF TABLES

LIST OF FIGURES

CHAPTER 1
INTRODUCTION

1.1 Background of GaN

After over five decades of technological development, semiconductor-based devices have become the mainstream of modern solid-state electronic circuits. In this area, Silicon technology is the most developed, yielding low cost, extremely reliable devices. About 90 percent of the solid-state devices manufactured worldwide today are based on silicon material. However, some disadvantages are intrinsically associated with silicon technology. The main drawbacks are its relatively small bandgap of 1.12 eV. The small bandgap leads to higher intrinsic carrier densities, fuels large "dark currents" for detector systems, and increases noise. Also, it makes devices intolerant to high temperature operation because the intrinsic carrier density increases exponentially with temperature. Thus, this material cannot be used for many applications involving high temperature operation. The problem is made worse by the fact that the thermal conductivity of Si is not very high. This presents an inherent limitation to efficient device cooling through heat removal.

In addition, the small bandgap of silicon reduces the energy threshold for band-to-band impact ionization. Subsequently, the device breakdown is fairly small compared to the other materials, such as GaAs, which is an important III-V compound semiconductor. As a result, devices made of Si impact ionize easily and are unable to withstand high values of electric fields and external voltages. This limits the upper range of voltage operation and

---

The journal model for this work is the *Journal of Applied Physics.*

makes Si based technology unsuited for high-power, high-voltage applications. The low threshold for impact ionization also implies that the material is not "radiation hard" and will deteriorate relatively quickly under the influence of external ionizing radiation. All the space applications have to deal with the external radiation problem very seriously.

Summarizing the above shortcomings, the existing silicon semiconductor technology is not suitable for the requirements of the entire semiconductor industry. It becomes necessary and essential, therefore, to find and develop other suitable materials for many of the high-temperature, high-voltage applications. Ideally, such materials should also have the favorable property of "survivability" through radiation hardness.

In terms of the potential industrial, military, and space applications, the need for electronic devices capable of operating at high electric fields, with the ability to withstand elevated temperatures and harsh environments has been increasing dramatically [1-3]. This has given rise to the recent surge of research activity in wide-band-gap semiconductors. For example, pollution control and the monitoring of toxic gases in the environment are becoming important concerns both for industry and the government. In particular, the measurement and control of toxic gas emissions from automobile exhausts and airplane jet engines is a vital issue. However, for efficient space-effective monitoring and control of the emissions, the sensors need to be positioned close to the hot engines. Proximity placement eliminates the need for costly fiber optic links and greatly helps reduce overhead space for compactness. Weight reduction is also an important related consideration, especially for aircraft and space applications and hence favors compact semiconductor devices. The development of such an emissions sensor for the above application will require a semiconductor-based device for compactness that is capable of operating at elevated

temperatures. Another potential application of high-temperature electronic devices capable of operating under harsh environments is for circuits used in spacecrafts and armored vehicles for the military. In the former case, the harsh environment would arise from cosmic rays and other high-energy particles in space, while the possibility of electromagnetic pulses on the battlefield would present adverse conditions in the latter situation. Finally, in regard to high-power and high-voltage applications, the need to generate high power microwaves and communication electronics for radar would drive the need for developing a suitable semiconductor. Apart from military and space applications, there is also a demand for high power electronic components and semiconductor devices in the commercial sector. The power companies and utilities need to develop compact switching devices capable of manipulating electric distribution and changing power factor loads to optimize performance and reduce the power losses. Apart from the power handling capacity, the semiconductor devices for such applications need to be reliable under rugged conditions [4].

Materials other than silicon are being explored at the present time so that promising new technologies can be developed. One of the more exciting classes of materials being exploited for new technological breakthroughs is the III-V compound semiconductor. These materials are especially noteworthy in that they make possible the fabrication of "superlattices" based on alternating layers of lattice-matched heterojunction III-V semiconductor alloys. Lattice-matched heterojunctions are produced by Molecular Beam Epitaxy (MBE) and Metal-Organic Chemical Vapor Deposition (MOCVD) crystal-growth methods, as both techniques permit the growth of alternating semiconductor layers with extraordinarily abrupt boundaries and extremely small feature sizes.

GaAs, GaN, InP, etc., are direct-gap semiconductors that can emit light more efficiently than the indirect-gap semiconductors, such as silicon (Si) and germanium (Ge). Thus, it is not surprising that III-V compound semiconductors are finding increasing and extensive use in optoelectronic applications. These materials also provide for negative-differential conductance (NDC) that can effectively be used for developing solid-state oscillators and microwave frequency sources. The high-mobility valley to low-mobility valley transfer process is an important component of NDC, and also leads to a very high-velocity enhancement through transient velocity overshoot. Theory demonstrates that the highest speeds, at constant voltage, can be achieved if the electrons are initially injected into the Γ valley at energies just slightly below the X- and L-valleys and are maintained at this energy by moderate electric fields.

Wide-bandage semiconductor technology is a emerging as the superior alternative for a variety of micro- and nano-electronic devices that need to satisfy stringent and rigorous performance requirements. This is mainly due to some very unique and appealing material properties of wide bandgap semiconductor in general, and the III-nitrides in particular. For example, the III-V nitrides have a high thermal stability due to a large thermal conductivity parameter that allows for greater heat dissipation and helps alleviate the thermal management problem. Hence, these materials are projected to be strong candidates for the fabrication of power semiconductor devices. The materials also have a high breakdown voltage due to their wide band-gap. Hence, devices made from the III-nitrides, for example, should withstand much larger electric fields than the conventional III-V devices. This should lend the device structures to size down-scaling which is intended to increase the packing density, decrease costs per device and reduce

the internal carrier transit times. The saturation (or high-field) carrier drift velocities have also recently been shown to be higher than the GaAs-based systems currently in use, which should lead to a higher frequency response. Furthermore, the III-nitrides have a direct bandgaps that extend their utility to optoelectronics. Other benefits of a larger bandgap include a smaller thermal generation rate and higher intrinsic impedance, which reduces dark-currents and noise in these materials by orders of magnitude. Devices are also projected to operate at much higher temperature, as the intrinsic carrier densities are significantly smaller. These features make the III-nitrides prime candidates for high-power, high-temperature, high-frequency electronic devices. In this regard, $Al_xGa_{1-x}N/GaN$ multi-quantum well devices, $Al_xGa_{1-x}N/GaN$ super-lattice structures, $Al_xGa_{1-x}N/GaN$ heterostructure field effect transistor and $InGaN/GaN$ based light emitting diode have recently been demonstrated with success [2, 5-7].

Wide-bandage semiconductors hold the promise of a single new technology that can aid conventional implementations and create affordable new configurations. The III-V nitrides are very appealing because their high thermal stability, high breakdown voltage (due to the wide band-gap), and their high electron velocities make these materials suitable for high power and high temperature electronic devices. $GaN/Al_xGa_{1-x}N$ multi-quantum well devices, $GaN/Al_xGa_{1-x}N$ super-lattice structures, $GaN/Al_xGa_{1-x}N$ heterostructure field effect transistor and $GaN/InGaN$ based light emitting diode has been demonstrated recently.

Compared to $GaAs$, the GaN material has the following advantages [8-21]. Being direct bandgap materials, they lend themselves to a variety of optoelectronic applications. Bandgaps of the nitride material system consisting of GaN, InN, AlN and their ternary and quaternary compounds range from 1.9 eV (for InN) to 6.2 eV for AlN. Advantages

associated with a large bandgap include higher breakdown voltages, the ability to sustain large electric fields (which bodes well for device downscaling), lower generation noise, radiation hardness and high-temperature operation. Typically, GaN possesses attractive electronic material properties with a large bandgap ($3.4eV$), high breakdown field ($3\times10^6 V/cm$), the existence of modulation-doped $Al_xGa_{1-x}N/GaN$ structures with attendant high electron mobility ($1500cm^2/V\cdot s$) and extremely high peak ($3\times10^7 cm/s$).

1.2 Advantages of GaN HEMT

With the development of modern power devices, the goal is to push the limits for ultrahigh power, high efficiency, high speed, manufacturability and low cost. An important endeavor is to improve the speed of devices. The speed with which a switching operation takes place is determined by how fast an input pulse can be transmitted to the output. The switching time includes the transit time, which the electrons take to pass through the device, and the input- and output-capacitance charging times. Therefore, the transit time and the capacitance charging times need to be reduced to achieve fast switching. The transit time can be made shorter either by decreasing the current path length, bringing the terminals closer or by increasing the speed at which the carrier travels. Based on the short channel effect, the internal electric field can get quite high so that the velocity can easily reach the saturation value. High mobility materials are preferred as they decrease the transit time. A larger current is needed to charge and discharge the capacitance faster. Hence, the carrier density must be increased, as the current is proportional to the carrier density. Since electrons have a larger mobility than holes, devices with electrons as the active current carriers are always preferred.

The high electron mobility transistors (HEMTs) fabricated using wide-bandgap semiconductors show promise as a high-gain, low-noise device with superior frequency response. In 1969, Esaki and Tsu [22] proposed the concept of separating the charge carriers from the parent donors by growing a modulation doped heterostructure (MDH).

A brief list of the potential benefits of GaN based HEMTs is given below. These potential benefits demonstrate the need for focusing on an in-depth study of GaN material itself, its electronic behavior and its HEMT response.

(a) Due to the good thermal conductivity and hence better thermal management, the current handling capacity of GaN HEMT devices is expected to be superior. This should lead to compactness and higher on-chip packing densities.

(b) Low noise and extremely small leakage currents. This should make GaN an excellent material for the fabrication of high-energy detectors.

(c) The high field electron drift velocity is predicted to be higher than most other semiconductor materials such as GaAs and Si. This should lead to inherently high switching speeds and superior cut-off frequency values. Hence, GaN HEMT based transistors would be very useful for signal amplification for high power microwaves.

(d) Due to the low leakage currents, GaN HEMT can be expected to be very efficient and could have applications such as non-linear rectification of power signals, heterodyning and signal mixing and multiple frequency generation.

(e) The large bandgap of GaN will allow for higher doping levels than in Si. This should help reduce the "on-state resistance" leading to smaller power losses and faster "RC" time constants.

(f) The high breakdown electric field will allow the fabrication of thinner layers at higher doping levels for a given voltage than Si or GaAs devices. This should reduce the physical device size without adversely affecting the internal resistance. Power MOSFET and BJT structures should benefit.

1.3 Definition of Objectives

GaN is a relatively new material for semiconductor devices and not much research has been done in this area. Though the material has not been fully explored, the trends show promise. Research on GaN, however, is still in its infancy, and many of the predicted advantages of GaN have yet to be fully realized. The material has also not been fully characterized and modeled, and most of the merits of GaN devices are based on guesses, estimates and extrapolations from the GaAs material properties. A detailed understanding of this material and its properties has not yet fully emerged. However for a more realistic outlook, it becomes necessary to correctly model and understand the electrical response behavior of GaN before venturing into costly fabrication.

Results from research work that has been carried out so far identify several important issues. These issues have a broad scope and cover many areas which include processing technology and crystal growth, material characterization, the evaluation of intrinsic GaN properties, device physics, electronic transport behavior and predictions of the electrical response characteristics. This research will focus on only a small part related to electrical transport and predictions of the transient response of simple GaN HEMT devices. The main issues and research objectives are given below. For completeness, however, some of the other interesting problems and research areas are also briefly discussed.

The first is the issue relating to the large polarization of the GaN material. For instance, polarization-related modifications to the internal fields could affect ionization rates in quantum-well devices or alter electronic injection at the gate contacts of HFETs. Furthermore, carrier mobility should also be affected by the polarization-induced field enhancements since carrier wave functions and the scattering rates are directly modified in the process. In HEMTs, large values of the polarization fields would lead to large changes in the carrier density within the two-dimensional conducting channel. For example, electron densities much larger than those attainable in GaAs can be produced even in the absence of strong external doping.

Secondly, interface roughness scattering is expected to increase due to the close proximity of the 2DEG, with the barrier layer at the higher electric fields. The interface roughness scattering is typically quantified on the basis of weak-perturbation theory, in terms of two parameters: the root-mean-square value of fluctuations at the interface, and the correlation length L between fluctuations. These parameter values are not well known for AlGaN/GaN HFETs and need to be determined.

Thirdly, the degeneracy effects associated with the higher electron density need to be carefully evaluated because of the high 2DEG density. There have been no studies of the role and extent of Pauli exclusion on the mobility in GaN HFETs, to the best of our knowledge. These are expected to influence scattering rates and electronic transitions in response to external laser excitation.

Assessment of the impact on the electrical response due to the material parameters and device geometry. For example, changes in the mole fraction of the AlGaN barrier layer, the spacer thickness or the barrier width all alter the polarization field, the carrier

density and, thus, the electrical response characteristics. The response to high-frequency ac signals is also not known, and needs to be studied.

Finally, it is also important to study the GaN HEMT response at high frequencies for microwave applications. The important aspects include: harmonic distortion, third-order inter-modulation of signals and the dependence of the response on operating temperature, large-signal swing and applied bias.

It is important to obtain quantitative predictions in order to optimize the device operating characteristics. In the future, by taking the above-discussed factors into account, the following results will be obtained:

(a) Numerical evaluations for the drift velocity as a function of the applied gate voltage and longitudinal electrical field in high-voltage, high-temperature, high-frequency;

(b) Using Discrete Fourier Transform (DFT) for harmonic analysis and non-linear behavior. Predictions of important RF characteristics for GaN HEMTs such as third-order intercept point (IP3), linearity performance, the dynamic range, two-tone inter-modulation distortion (IMD);

(c) Suitable comparison with GaAs/AlGaAs HEMT system;

(d) Real space transfer phenomenon, and its implications for microwave amplification. The roles of drain biasing and operating temperature need to be probed.

The expected research contributions and analytical studies in this dissertation work would include the following as given below.

(1) To develop, debug and validate Monte Carlo software codes for the analysis of electron transport in GaN. Two codes will be written. The first will be for bulk material

since some experimental data is available in the literature for direct comparison. The second would be a code for two-dimensional electron flow for a 2DEG in a GaN-AlGaN HEMT structures that are of interest here.

(2) Calculations of transport parameters and characteristics such as electron mobility and drift velocity based on the simulation codes. Both transient and steady-state conditions will be probed. The effects of features peculiar to the GaN-AlGaN system such as polarization, interface roughness scattering and degeneracy associated with Pauli exclusion at high 2DEG density would be probed. The effects of longitudinal drain fields and perpendicular gate voltages on the electron drift velocity will be probed.

(3) The response of GaN HEMTs to RF signals applied at the gate terminal. The output drain currents will be analyzed for harmonic distortion and inter-modulation. High-field non-linearities and high-temperature behavior under large signal RF conditions will be studied as well. Methods such as the Fast Fourier and Wavelet Transforms will be used for a numerical analysis of the high-frequency characteristics of GaN HEMTs. Other parameters that would be obtained include the third-order intercept point (IP3), linearity performance, the dynamic range, device transconductance and the two-tone intermodulation distortion (IMD).

(4) To provide the comprehensive comparisons between GaN/AlGaN and GaAs/AlGaAs. Such as different parameters on gate voltage, longitudinal electrical field, real space transport, temperature as well as frequency.

Monte Carlo method will be used although the whole research work. Some simulation results will be processed with MATLAB application software.

1.4 Summary

GaN HEMTs appear to be a promising device for high-power, high-temperature, high-frequency applications. However, there is crude and insufficient knowledge on its transport properties. There is also a relative technological immaturity of the *GaN* material system. GaN is quite different from the traditional GaAs-based material systems that have a mature history and knowledge-base. A number of issues somewhat unique to the GaN-based heterostructure system arise and can be expected to have important bearing on the transport behavior. They include internal polarization arising from the strong piezo-electric effect, interface roughness scattering and degeneracy associated with Pauli exclusion at high 2DEG density, as well as the real space transport and noise behaviors, and are all expected to be important. The high-frequency response of GaN-based devices, such as the HEMT, has not been studied. Such high-frequency, large-signal behavior is important in the context of microwave amplification. Consequently, this dissertation attempts to make a contribution in understanding and evaluating the electrical response characteristics of GaN HEMT system.

In this dissertation, Chapter 1 is the introduction to the distinguish properties of GaN and HEMT as a dramatic high-speed device structure. Chapter 2 presents a brief literature review to present the current status of GaN HEMT both on experimental and theoretical sides; topics include highlights of GaN properties, unique characterization related to GaN HEMT simulation and harmonic distortion. Numerical simulation approach and Monte Carlo method are discussed in details in Chapter 3. The various results obtained from the current simulations are discussed in details in Chapter 4. Appropriate comparisons with available experimental data are also included. Under many design related parameters, the

differences between GaAs/AlGaAs and GaN/AlGaN system are provided in this chapter. Finally, Chapter 5 summarizes the main results and contributions. Some discussions of possible future simulation work have also been given at the end.

CHAPTER 2

LITERATURE REVIEW AND BACKGROUND

2.1 Introduction

A quick review of the GaN/AlGaN High Electron Mobility Transistor (HEMT) literature is given in this chapter. Some of the important electronic properties of GaN are first discussed. Compared with GaAs, the wide-band-gap propriety of GaN is emphasized. The dramatic advantages for potential applications in the microwave, RF and high-temperature areas are pointed out. Then two crystal structures of bulk GaN, namely the zinc-blende and wurtzite lattices, are discussed in detail. Next, scattering mechanisms relevant to transport calculations are presented in some detail. This chapter also touches upon some of the effects peculiar to and inherent in the GaN material system. These include interface roughness scattering, the polarization effect and the degeneracy that must all be taken into account for an accurate and physical model representation. This is followed by the theory and principles of HEMT. Details of the related energy band and two-dimensional electron gas characteristics as reported in the literature have also been presented. This chapter ends with the discussion of the quasi-triangular approximation of quantum well and subbands.

2.2 Overview of the GaN Material System

Over the past five years or so, the nitride material system consisting of GaN, InN, AlN, has been the focus of intense research [8-15]. Advantages of these direct, large-bandgap materials include higher breakdown voltages, the ability to sustain large electric fields (which bodes well for device downscaling), lower generation noise, radiation

hardness and high-temperature operation. The nitrides have shown promise as emitters and detectors [16-18], Bragg reflectors [20] and light-emitting diodes (LEDs) [21]. Also, since the diffraction-limited optical storage density increases almost quadratically as the probe wavelength is reduced, the appeal of nitride-based coherent sources is obvious. GaN-based electronics are also expected to be important in applications for high-temperatures and rugged environments such as sensors for jet and automobile engines [24], in military hardware, and space-based sensors operating in the solar blind region of about 260--290 nm. In the area of high-power electronics, GaN-based amplifiers are projected to have some unique advantages over their GaAs-based counterparts. For example, several orders of magnitude improvement in the figures of merit for power switching has been shown over silicon devices [25]. For identical current capability, the GaN devices could be doped more strongly (thereby reducing internal resistance and delay times) and have smaller die sizes because of their ability to withstand higher electric fields. The smaller size would also decrease the transit time in certain drift devices, which would increase the operating speed and frequency response.

Due to the higher inter-valley separation and the larger optical phonon energy, GaN should facilitate higher currents and faster intrinsic speeds. GaN lends itself to hetero-structure fabrication, and the presence of a strong internal polarization can create very high sheet carrier densities, even in the absence of intentional doping. Characterization of the heterojunction high-electron mobility transistors (HEMTs) fabricated has revealed strong enhancement in carrier densities [10], which should lead to higher currents. Experimental demonstrations of large radio-frequency power densities, as measured in Watts per millimeter of the gate periphery, have already been made

[28,29]. However, not much research has been done on devices made from GaN, and this area remains a rich field of study.

2.2.1 Characterization of Bulk GaN

To date, a few theoretical investigations of the electronic transport properties of bulk GaN [30-32] have been made. The steady-state electron drift velocity calculation has been based on the Ensemble Monte Carlo technique. These calculations for bulk GaN have either assumed a one- or two-valley analytical band structure for simplicity, or used full three-valley, nonparabolic conduction band models for higher accuracy.

It is well known now that GaN crystallizes in both the zinc-blende and wurtzite structures with slightly different material properties and substantially different band structures. Brennan et al. [33] reported on the bulk electronic transport properties in both zincblende and wurtzite phases. The calculation of the electronic band structures was based on the empirical pseudopotential method [34,35]. Since the band energies are required over a dense k-space mesh throughout the Brillouin zone, calculational efficiency is important. Consequently, in their analysis, the spin-orbit interaction was neglected and a local pseudopotential used. Approximately, an additional 100 plane wave states were included in Lowdin perturbation theory [36]. The effective mass was taken as the principle fitting parameter. For wurtzite material, the accepted experimental value for the energy gap is 3.4ev and the electron effective mass is $0.19m_0$. For zincblende GaN, the experimental data yields an effective mass of $0.15m_0$ [37].

The pseudopotential band structures along the main symmetry axes of the Brillouin zone are shown in Fig. 2.1 for wurtzite and zincblende GaN, respectively.

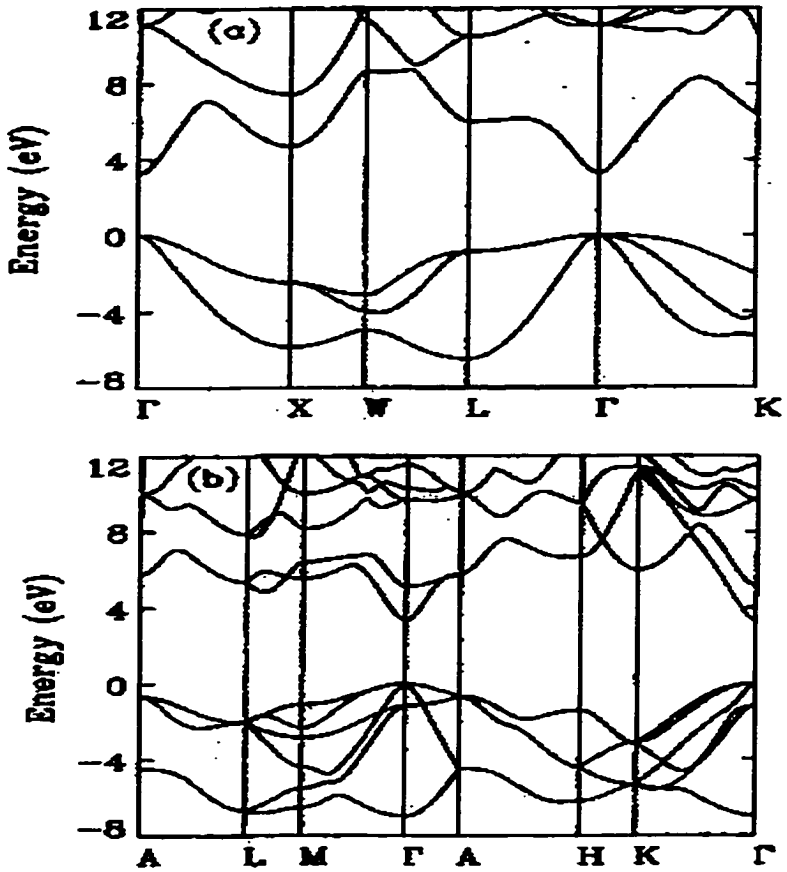

Fig. 2.1 Pseudopotential band structures for GaN on

a) zincblende and b)wurtzite phase [33].

Although the two phases of GaN are very similar (both have direct fundamental gaps at the Γ point that differ by less than 10% in magnitude) their conduction bands appear to be sufficiently different to cause significant differences in their electron transport properties. For example, the nearest satellite valley in zinc-blende structure GaN (X point) is about 1.4ev above the conduction-band minimum, while the nearest satellite valley in wurtzite structure material (between the L and M points) is slightly more than 2 eV above the minimum. Furthermore, they noted the existence of a second conduction band at relatively low energy approximately 2.2eV above the minimum at the

Γ- point in wurtzite material. The second conduction band is considerably higher energy in zinc-blende GaN.

PARAMETER	VALUE
Lattice constants in meter (a , c)	3.189×10^{-10}, 5.185×10^{-10}
Dielectric constants $k(0)$, $k(4)$	9.5, 5.35
Density ($g \cdot cm^{-3}$)	6.095
Acoustic velocity (ms^{-1})	4.33×10^{5}
Effective mass (Γ_1, U, Γ_3 -valley)	0.21, 0.25, 0.4
Valley separation (eV)	0, 1.95, 2.1
Nonparabolicity factors for the three valleys (eV^{-1})	0.19, 0.1, 0
Longitudinal optical phonon energy (eV)	0.092
Intervalley phonon energy (eV)	0.065
Acoustic deformation potential (eV)	8.0
Zero-order equivalent intervalley deformation potential (eV/cm)	0.5×10^{-9}
Zero-order nonequivalent intervalley deformation potential (eV/cm)	1.0×10^{-9}
First-order intervalley potential (eV)	5.0
Interface roughness correlation length (nm)	1.5
RMS fluctuations of interface roughness (nm)	0.65
Spontaneous polarization (C/m^2)	-0.052x–0.029
Elastic constants C_{13} and C_{33} (GPa)	5x+103 and -32x+405
AlGaN alloy scattering parameter (eV)	0.5

Table 2.1 Properties of Gallium Nitride at 300k

For wurtzite-phase GaN, the minimum is located at the Γ point. The satellite valleys are at the U point that is two thirds of the way between the L- and M-symmetry points. The next highest valley is located at the Γ_3 point. Thus, two Γ valleys and the six equivalent U valleys need to be considered for a reasonably accurate analysis. The most important material parameters of GaN at room temperature are listed in Table 2.1.

From experimental data, the curves for conduction valleys of alloys vs the Aluminum mole fraction x can be fitted by the following polynomials [38]:

$$E_g^{\Gamma} = 3.38 + 2.50x + 0.05x^2, \tag{2.1}$$

$$E_g^{X} = 4.57 - 0.08x + 0.61x^2, \tag{2.2}$$

$$E_g^{L} = 5.64 + 2.99x + 0.80x^2. \tag{2.3}$$

2.2.2 Comparison Highlights Between GaN and GaAs Materials

There are increasing demands of military and commercial applications on low-noise, high-frequency amplifications, especially in the high-power regime. HEMTs are appropriate device candidates as they yield high electron mobility and velocity, which helps improve the frequency response. The GaN material is being proposed due to the small intrinsic carrier densities, low noise and high-thermal resistance. Thus, for example, the GaN HEMTs appear to be ideally suited as amplifiers for high-power microwave signals. Some of the important advantages and superiority for the GaN material system are compared to the GaAs material.

(i) High current gain: Characterization of the heterojunction field-effect transistors (HFETs) fabricated to date has revealed a strong enhancement in carrier densities, which should lead to higher currents. This enhancement is thought to arise from

stronger piezo-electric fields in the GaN and AlGaN layers. The AC gain is therefore expected to be large, so GaN HFETs offer bright prospects for use in microwave amplification, particularly at the X-band and higher frequencies [29].

(ii) Wide band-gap: This lattice structure guarantees a band-gap in the 3.3-3.6 eV range depending on the GaN crystal type. This is much larger than the 1.41 eV bandgap typical of GaAs. As a result of the larger bandgap, the nitride-based devices can have higher thermal stability, a larger breakdown voltage, lower noise and radiation hardness. The wide band-gap effectively prevents electrons in the valence band from making transitions to the conduction band. It leads to low noise and smaller dark currents for ultraviolet (UV) detectors.

(iii) Thermal stability: This property is very important for high power applications. The high thermal conductivity parameter helps in transporting heat away from internal hot spots and sources of generation. This makes thermal management and control easier and guarantees that thermal runaway conditions can be avoided. The thermal stability also helps enhance the power handling capability of the GaN based devices.

(iv) High frequency: GaN can be used with its alloys (such as AlGaN) to form heterostucture devices. Such devices have high carrier drift velocities due to suppression in the impurity scattering. The overall result is an increased transconductance with operation at millimeter-wave frequencies with ultra low noise. Besides, the high field carrier drift velocities in GaN are almost a factor of two larger than those in GaAs. This allows for faster speeds and a better high-frequency response for GaN relative to GaAs at high operating voltages.

Parameters	*GaAs*	*GaN*
Density(g/cm^{-3})	5.32	6.095
Lattice constant(A)	5.65	4.50
Dielectric constant ε_0 ε_∞	12.9 9.7	9.5 5.35
Bandgap (eV)	1.43	3.4
Electron Effective mass ($\frac{m^*}{m_0}$)	0.069, 1.43, 1.58 (Γ, X, L)	0.20, 0.24, 0.40 (Γ_1, L, Γ_3)
Nonparabolical constant	0.67, 0.44, 0.36	0.19, 0.17, 0
Electron Mobility (cm^2/Vs)	4500	1500

Table 2.2 Parameters compared between *GaAs* and *GaN*.

Regarding electron transport properties, the Γ–valley effective mass of GaN is 0.20, which is about three times higher than that of GaAs. Hence, the mobility in bulk GaN is expected to be inferior to GaAs, and this has been shown in experimental work. However, the high-field drift velocity of bulk GaN is larger than that of GaAs [26]. This is due to the higher inter-valley separation and the larger energy of optical phonons. The former helps keep a higher fraction of electrons within the lower mass valley, while the latter reduces the net role of phonon scattering by increasing the emission threshold. In GaN, however, the presence of a strong internal polarization arising from the spontaneous and piezoelectric effects works to create stronger band bending and contributes to very high sheet carrier densities, even in the absence of intentional doping.

There are currently many electronic components and products based on the GaAs compounds. However, in comparison to GaAs, the GaN material appears to have some additional advantages. For example, GaN and its alloys provide for semiconductor systems that have a much higher bandgap variation. The bandgaps are tunable between

1.9 and 6.2ev (i.e., a range of over 4.25 eV) upon alloying with In or Al. The GaN based material system also has higher thermal conductivity and stability. Typical characteristics for the GaN material include a high breakdown field of $3\times10^{6}V/cm$, the existence of modulation-doped $Al_xGa_{1-x}N/GaN$ structures with high electron mobility of about $1500cm^2/V\cdot s$ and extremely high peak $3\times10^{7}cm/s$ drift velocities [39]. Figure 2.2 shows the comparison of steady state electron velocity as a function of electric field in GaN, Si and GaAs.

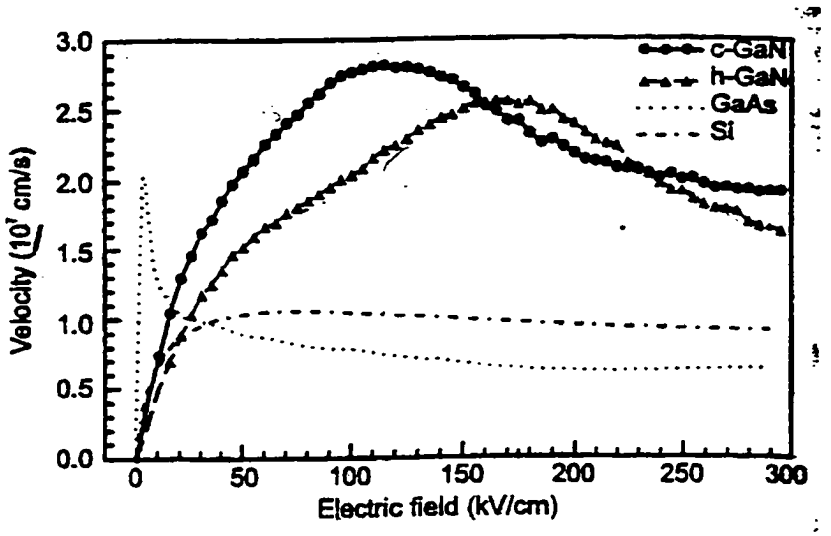

Fig. 2.2 Steady state electron velocity as a function of electric field in GaN, Si and GaAs.

2.2.3 Scattering Mechanisms

The transport properties of the system under study are largely determined by the scattering mechanisms, which influence electron transport. The most important scattering

mechanisms include scattering from acoustic phonons, polar optic phonons, inter- and intra-valley scattering, ionized impurity interactions and disorder-related effects arising from alloy heterogeneity and interface roughness [26,39]. A summary of the scattering mechanisms relevant to the AlGaN/GaN system is given below. The details are discussed later in chapter 3.

(i) Phonon scattering: Phonon scattering plays an important role in limiting the electron mobility in III-V semiconductors. The three most important phonon-scattering processes are deformation potential due to the acoustic modes, piezoelectric interactions associated with the acoustic modes and polar optical scattering. All three of these processes have been studied extensively in bulk semiconductors.

(ii) Acoustic deformation scattering: The perturbation Hamiltonian is assumed to be linear in the local deformation produced by the phonons in the crystal. The acoustic phonon energy is also assumed to be negligible compared with $K_B T$, so that the mechanism is elastic with the change in electron energy during the scattering event taken to be negligible.

(iii) Intervalley phonon scattering: In a many valley model, electrons can undergo transitions between states in two different equivalent or non-equivalent valleys, after scattering with large momentum phonons. Considering two valleys (in the conduction band, for example) involved in the transition, the phonon wavevector is approximately constant and given by the distance in the Brillouin zone between the minim of the initial and final valleys. The energy involved in the transition is also approximately constant, and intervalley scattering can be formally treated in the same way as intravalley optical phonon scattering, with the deformation potential interaction.

The change in energy of the carrier is equal to the typical phonon participating in the event.

(iv) Ionized impurity scattering: The ionized impurity scattering is elastic in nature. This is due to the large size of the impurity atoms relative to the electrons or holes.

Within the high energy region, deformation potential scattering is assumed to be the dominant scattering mechanism. The scattering rate in this region is obtained by integrating over the pseudopotential calculated final density of states including the collision broadening of the final state. The scattering rate is determined from the self-energy of the electron base on the optical theorem [26]. The deformation potential is assumed to be constant and is chosen to match the low-energy scattering rate at a selected energy. Fig. 2.3 is a demonstration of different scattering rate in wurtzite GaN.

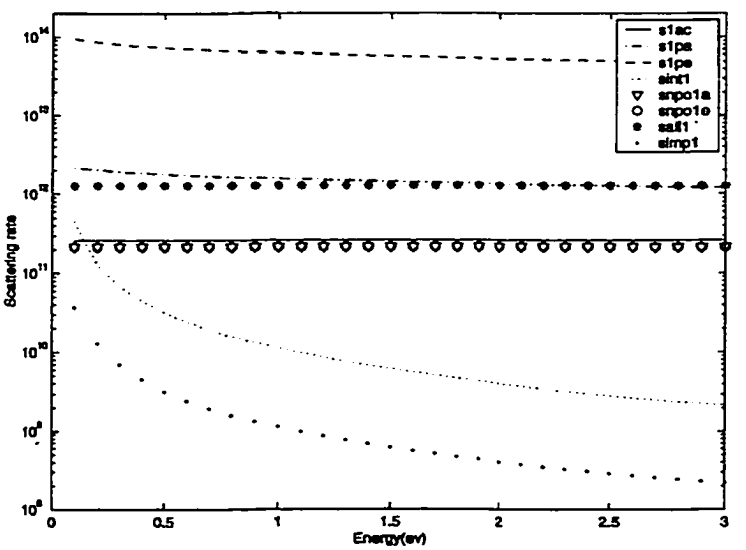

Fig. 2.3 Electron scattering rates for the wurtzite in GaN-AlGaN at 300K.

2.2.4 Interface Roughness Scattering

Surface asperities at the interface between GaN and AlGaN are expected to constitute a major cause of scattering, especially at high electron concentrations. The space-charge present at the interface makes this a Coulombic-type interaction. Charges near the interface, in conjunction with their image charges, set up a distribution of dipoles. Due to undulations in the interface, the distance between the charge and its image is variable, and this creates a spatially varying potential perturbation. Scattering of mobile carriers is then considered to be caused by this interface perturbing potential. Here, the treatment of the interface roughness scattering has been based on a simple Gaussian model for the autocovariance function [40], rather than the exponential dependence used by Goodnick et al. for silicon [41].

This model assumes an infinite barrier at the interface, whose position $z = \Delta(r)$ may have a small and slowly varying displacement. Classically when quantization of the electron motion in the z direction is not important, scattering due to the surface has customarily been treated by a boundary condition on the electron distribution function, following the initial work of Schrieffer [42]. With his assumption, diffuse scattering at the surface and so-called Fuchs [43] parameter is used to describes specular reflection.

When energy separations between different subbands are sufficiently large and the change in the form of the wave function can be neglected, the effect of surface roughness is calculated to lowest order from the matrix element. The mobility decreases in proportion to N_s^{-2} at high electron concentrations. Usually, a Gaussian form of the correlation of the surface roughness is given:

$$< \Delta(r)\Delta(r') >= \Delta^2 \exp[\frac{(r-r')^2}{\Lambda^2}], \qquad (2.4)$$

where Δ is the average displacement of the interface and Λ is of the order of the range of its spatial variation in the direction parallel to the surface. Then we have [40]

$$<|\Delta_q(r)|^2>=\pi\Delta^2\Lambda^2\exp[-\frac{q^2\Lambda^2}{4}] \quad . \tag{2.5}$$

The interface roughness scattering is most simply treated in the Born approximation by assumption that the roughness can be regarded as a weak perturbation. This is then characterized in terms of two parameters, namely, the correlation length L and root-mean-square (rms) height Δ of the roughness fluctuations. This model has previously been shown to be adequate, yielding L and Δ values of about 2.2 and 0.2 nm for silicon [44], 2.3 and 0.8 nm for SiC [45], respectively. The corresponding parameters for the GaN/AlGaN system, however, are not known. They were obtained here through a best-fit procedure. The results, as discussed in Chapter 4, are 1.5 nm and 0.65 nm [46] for correlation length L and root-mean-square (rms) height Δ of the roughness fluctuations, respectively.

More complicated treatments of discrete AlGaN islands at the interface have been suggested to include localization effects [47] but were not used here for computational simplicity.

2.2.5 Degeneracy

The influence of the Pauli exclusion principle on the average transport properties of semiconductors can be of great importance, especially at high carrier densities. For example, when modeling of microwave devices, one often deals with highly doped regions that are expected to be degenerate. Additionally, when balance equations are used, it is always assumed that electrons in the low field region (typically characterized

by high doping levels) have the same average kinetic energy as the lattice, in terms of their characteristic temperature. The calculations show that a proper account of the Fermi statistics causes significant changes, especially to the electron "temperature." It cause the average energy of the carriers is related to the Fermi energy E_f, and not to $K_B T$.

Pauli exclusion was included based on a rejection technique implementation first proposed by Lugli and Ferry [48]. Although the EMC is a semiclassical technique that simulates electrons moving as classical particles, in reality the electrons behave like Fermions. They, therefore, must obey the Pauli exclusion principle: each quantum number is available for at most two electrons, which differ in their spin quantum number. Following the simple theory of the Fermi gas [49], the number of available k-space states for a system enclosed in a volume V is given by $V/(2\pi)^3$. At zero temperature, the electrons fill up a region of k-space called the Fermi sphere. The radius of this sphere, the Fermi wave-vector k_F, is related to the electron concentration n (at absolute zero) by

$$| k_f | = (3\pi^2 n)^{1/3}, \tag{2.6}$$

where n is the net electron concentration. At nonzero temperatures, electrons pill out of the Fermi sphere, moving into states previously vacant and thereby allowing for current flow to occur. In metals, only the electrons in a region of the order of $K_B T_0$ from the Fermi level can take part in collision and conduction processes. Similar effects happen in semiconductors under degenerate conditions when the Fermi level lies near or within the conduction band. The Pauli exclusion principle can be thought of as a many-body effect that influences the transport properties of degenerate semiconductors by limiting the phase space available for electronic transitions.

Degeneracy is expected to play a role in the GaN 2DEG system, because of the large carrier densities that have been observed experimentally. This effect, which essentially reduces the scattering rate due to a finite occupancy probability of the final state, was taken into consideration.

2.2.6 Polarization Effects

Due to a lack of inversion symmetry, nitrides exhibit strong piezoelectric effects. Such non-centrosymmetric compounds exhibit two different sequences of their atomic layering. For GaN heterostructures with the growth direction normal to the {0001} basal plane, the atoms are arranged in bilayers. These bilayers consist of two closely spaced hexagonal layers, one formed by cations and the other by anions, leading to polar faces. Thus, a basal surface could be either Ga (or N) faced, corresponding to either Ga (or N) atoms on the top position of the {0001} bilayer. The two (0001) and (000$\underline{1}$) surfaces are not equivalent, and lead to different net polarizations and internal charge densities. For clarity, a HFET with its equilibrium energy-band diagram is shown in Fig. 2.4 and Fig. 2.5 for the Ga and N polarity. The GaN is relaxed, while the AlGaN has been assumed to be under tensile strain. The spontaneous polarization for AlGaN is larger in magnitude than that for GaN. The spontaneous and piezoelectric polarizations support each other, and a large interface charge is created.

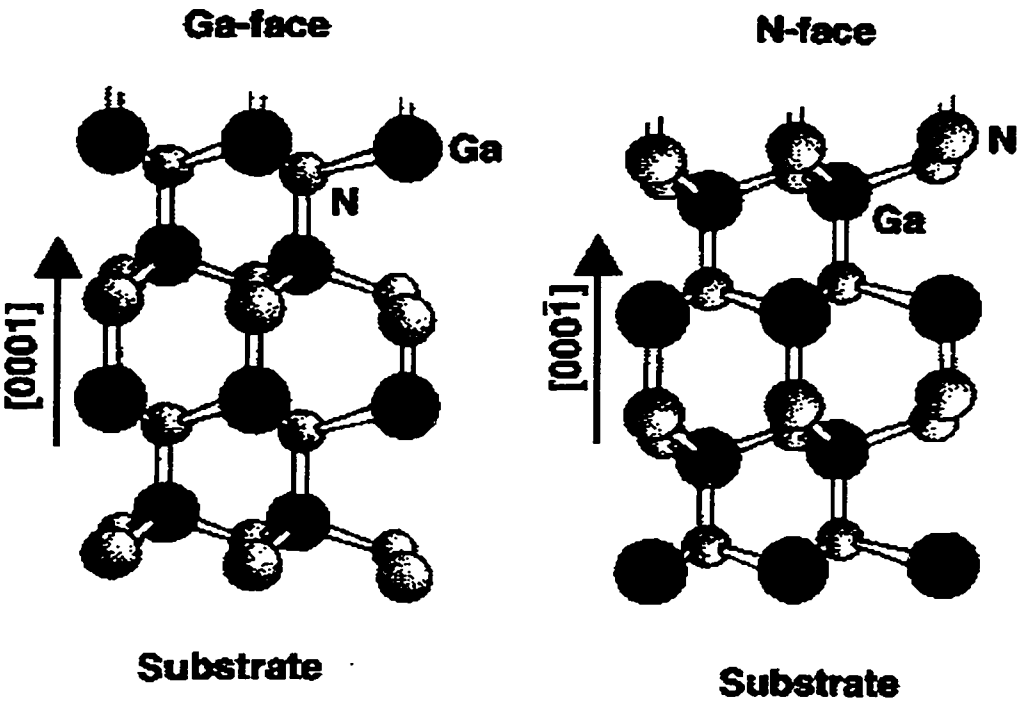

Fig. 2.4 Schematic drawing of the crystal structure of wurtzite Ga-face and N-face GaN.

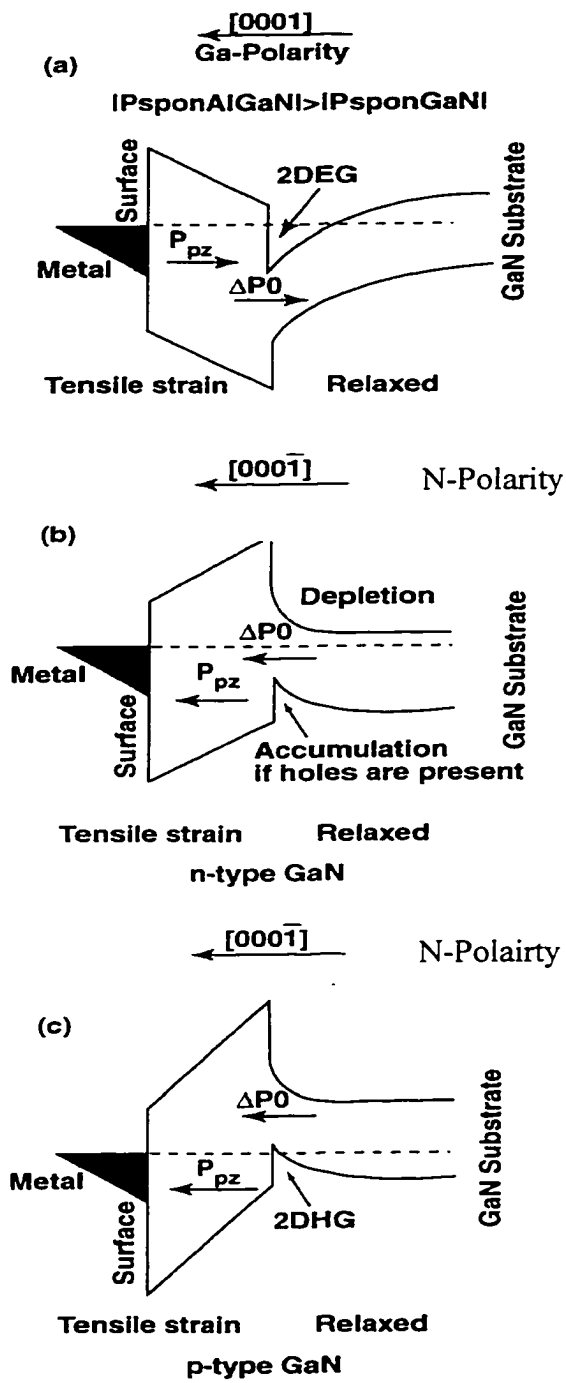

Fig. 2.5 Equilibrium band diagrams of a GaN-AlGaN HFET [46]. a) Undoped GaN with Ga polarity; b) N-type GaN with N polarity; c) P-type GaN with N polarity

In Fig 2.5a, the resulting potential slopes towards the interface from both sides and helps drive mobile electrons towards the channel. There is thus no specific need to dope the AlGaN or have a spacer layer. The metallic reservoir and carrier generation processes can furnish the requisite electrons to the GaN. The situation for an N polarity, on the other hand, is different as shown in Fig. 2.5b and 2.5c. Both n- and p-type doping have been considered, but the net result is the same. The energy diagram predicts an accumulation of holes at the interface rather than electrons. In any case, it becomes clear that details of the surface polarity need to be taken into account, and the most effective scenario for a GaN HFET appears to be the Ga polarity that would create a large electron pool without having to incorporate any dopant impurities [51].

Both the spontaneous [52] and piezoelectric [51] polarization effects were taken into account. The piezoelectric polarization P_{PE} can be calculated from the piezoelectric constants e_{33} and e_{33} as:

$$P_{PE} = e_{33}\varepsilon_z + e_{31}(\varepsilon_x + \varepsilon_y), \tag{2.7}$$

where ε_z is the strain along the c-axis and the in-plane strains ε_x and ε_y are equal and assumed to be isotropic. The strains can be expressed in terms of changes in the lattice constant parallel (a_o) and perpendicular (c_o) to the c-axis as:

$$\varepsilon_x = \varepsilon_y = [a(x) - a_0]/a_0, \tag{2.8}$$

$$\varepsilon_z = [c(x) - c_0]/c_0 = -2[C_{13}(x)/C_{33}(x)]\{[a(x) - a_0]/a_0\}. \tag{2.9}$$

In the above, $C_{13}(x)$ and $C_{33}(x)$ are the elastic constants, x is the aluminum mole fraction in the $Al_xGa_{1-x}N$ material, and $a(x)$ is the in-plane lattice constant. Values of the piezoelectric coefficients $e_{33}(x)$ and $e_{31}(x)$, as well as the elastic constants $C_{13}(x)$ and $C_{33}(x)$ for the GaN-$Al_xGa_{1-x}N$ system, can be expressed in terms of the mole fraction x as,

$$e_{33}(x) = (0.73x + 0.73)\ Cm^{-2}, \tag{2.10}$$

and

$$e_{31}(x) = (-0.11x - 0.49)\ Cm^{-2}, \tag{2.11}$$

$$C_{33}(x) = (-32x + 405)\ GPa, \tag{2.12}$$

and

$$C_{13}(x) = (5x + 103)\ GPa\ . \tag{2.13}$$

Finally, the spontaneous polarization $P_{SP}(x)$ for this material system is expressed as,

$$P_{SP}(x) = (-0.052x - 0.029)\ Cm^{-2}. \tag{2.14}$$

Hence, the magnitude of the polarization-induced interface sheet charge density $\Phi(x)$ in Cm^{-2}. For the pseudomorphic, AlGaN-GaN heterostructure turns out to be,

$$\Phi(x) = 0.0483x\{[5x + 103)/(-32x + 405)](0.73x + 0.73) + (0.11x + 0.49)\} + 0.052x \tag{2.15}$$

This interface charge works to alter the interface electric field, and hence, affects the channel density, the interface roughness scattering, the free carrier screening and the channel degeneracy. The channel electron charge density $qn_s(x)$, is then [53],

$$qn_s(x) = \Phi(x) - (\frac{\varepsilon_0 \varepsilon(x)}{dq^2})[qN_b(x) + E_F(x) - \Delta E_c(x)], \tag{2.16}$$

with ε_0 being the permittivity of free space, $\varepsilon(x)$ the dielectric constant, d the AlGaN barrier thickness, $N_b(x)$ the Schottky-barrier height, $E_F(x)$ the Fermi level with respect to the GaN conduction band-edge, and $\Delta E_c(x)$ the conduction band offset. Using values reported in the literature [54,55], leads to,

$$\varepsilon(x) = -0.5x + 9.5, \tag{2.17}$$

$$q\Phi_b(x) = (1.3x + 0.84)\ ev, \tag{2.18}$$

$$\Delta E_c = 0.7[E_g(x) - E_g(0)], \tag{3.44}$$

$$E_F = \{\frac{9\pi\hbar q^2}{8\varepsilon_0\sqrt{8m^*(x)}}\frac{n_s(x)}{\varepsilon(x)}\}^{2/3} + \frac{\pi\hbar^2}{m^*(x)}n_s(x). \tag{2.19}$$

The effective mass $m^*(x) \approx 0.22m_0 = 0.22 \times 9.1 \times 10^{-31}\ Kg$ [49,56] and the energy gap $E_g(x)$ is measured in eV to be [57],

$$E_g(x) = 6.13x + 3.42(1-x) - x(1-x)\ ev\ . \tag{2.20}$$

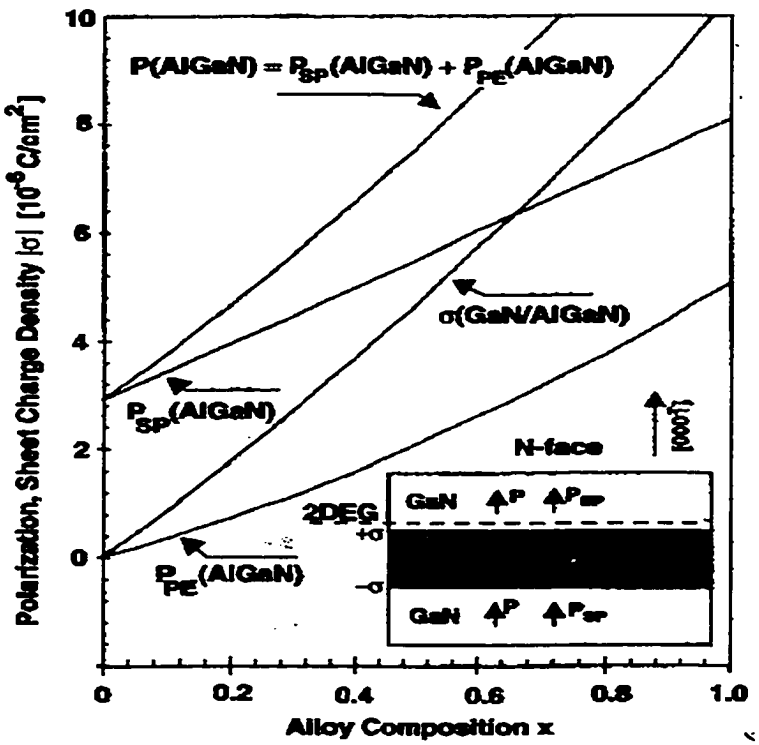

Fig. 2.6 Spontaneous, piezoelectric, total polarization of AlGaN and sheet charge density at the upper interface of a N-face GaN/AlGaN/GaN hetero-structure vs alloy composition of the barrier [51].

2.3 High Electron Mobility Transistors

In today's technical and business world, there is a strong need for high-speed computers to solve problems involving for high-volume data, real-time signal processing, graphics and remote imaging. Then there are the increasing demands of military and commercial applications on low-noise, high-frequency amplifiers. This section describes the basic principle of the filed-effect transistor in terms of selectively doped heterojunctions yielding high electron mobility and velocity, which at the device terminals give rise to a high transconductance FET that can be operated at a millimeter-wave frequency range with ultra-low noise. This device has the superior transport properties of electrons moving along the two-dimensional electron gas (2DEG) formed at the heterojunctions interface between two compound semiconductor materials. Various acronyms have been coined for these devices (MODFET, HEMT, TEGFET, SDHT, GAGFET, etc [57]). HEMT shows much promise in MMICs, demonstrably outperforming the GaAs MESFET in gain, low noise and frequency response. Enhancement-mode and depletion-mode HEMTs can also be fabricated on the same wafer for digital integrated circuits applications.

2.3.1 Introduction to HEMTs

Esaki and Tsu in 1969 [22] first proposed the concept of separating the charge carriers from the parent donors by growing a modulation doped heterostructure (MDH). Their aim was to reduce the impurity scattering of the mobile electrons with the charged impurity center. It was in the late seventies that techniques such as molecular-beam-epitaxy (MBE) were sufficiently developed to enable the growth of such structures. This

discovery laid the foundation for the development of high-speed heterostructure-based semiconductor devices, especially for GaAs material which naturally has a host of ternary alloys.

For the conventional MESFET, the high density of electrons is obtained by increasing the donor impurities. However, the charged impurity's center shares the same space with the free electrons and interacts with them. The interaction is the dominant mechanism responsible for the scattering of free electrons at low temperatures in doped, high-quality semiconductors. This tends to reduce the electron peak velocity. Spatial separation between the electrons and the donor ions may be achieved using a heterojunction between two semiconductors with different bandgap (e.g. $Al_xGa_{1-x}N$ and GaN). This is normally referred to as "modulation doped structure" or a "double hetrostructure."

Carrier confinement is typically engineered through the use of single or double modulation-doped heterostructures, which leads to the physical separation of the mobile electrons from their parent donors. This kind of structure is commonly called named a High-Electron-Mobility-Transistor (or HEMT) due to its fast characteristic response. It is a field effect transistor based on the modulation-doped structure. Also, it is called Modulation-Doped Field-Effect transistor (MODFET).

2.3.2 Structure of HEMTs

A typical HEMT structure is shown as Fig. 2.7.

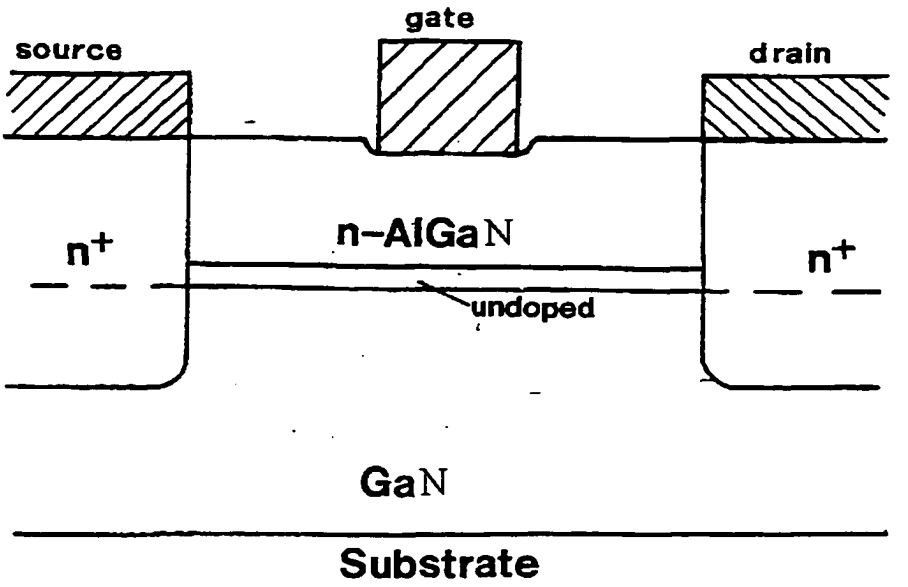

Fig. 2.7 Cross section of a typical HEMT device.

The typical structure of the HEMT starts with a semi-insulating substrate upon which a layer of undoped GaN is grown to a thickness of about 1um. $Al_xGa_{1-x}N$ is then grown, a 1~10 nm undoped layer first, and then a 60~100 nm n^+-layer. This is made possible with the selective doping ability of MBE.

The source and drain terminal are formed with heavily doped n^+. The $Al_xGa_{1-x}N$, which has the larger bandgap, is heavily doped. The GaN is lightly doped or normally undoped. An Schottky barrier gate as in the MESFET is used, but the carriers are confined in a channel physically separated from the gate as in a MOSFET structure. This feature and the presence of quantum effects, generate a completely new set of problems to be faced in the simulation of the device.

The undoped $Al_xGa_{1-x}N$ layer is used to further isolate ionized impurities from the electrons in the channel and minimize Columbic interactions. Source and drain contacts are typically obtained by metallization of AuGe/Ni/Au.

The metal gate and the channel are separated by only a few tens of nanometers and this coupled to the large dielectric constant of $Al_xGa_{1-x}N$ as compared to SiO_2, gives very large transconductance [58].

In normally-on devices, the depletion by the Schottky gate should be just enough to have the surface depletion extended to the interface depletion. Devices designed for about 10^{-12} cm^{-2} density in the channel typically use an AlGaN thickness of about 60 nm and are turned off at a gate bias of -1 Volt. This structure is used mainly for high-speed analog applications, like low-noise microwave amplifiers, since the power consumption is too high for large-scale integration.

In normally-off devices, the thickness of the doped AlGaN under the gate is smaller and the gate built-in voltage depletes this region completely, overcomes the built-in potential at the hetero-interface, and depletes the electron gas. No current flows through the device unless a positive voltage is applied to the gate. This type of device is suitable for use in a high-speed digital integrated circuit because of the low power dissipation. The load may be a normally on transistor with the gate shorted to the source or an ungated "saturated resistor," which has a saturating current characteristic due to the velocity saturation of the carriers.

2.3.3 Energy Band Structure of 2DEG

The electrons diffuse from the $Al_xGa_{1-x}N$ to the GaN, where they are confined in a triangular quantum channel generated at the heterojunction interface. Because of quantization effects, motion of the electrons confined in this channel is forbidden in the direction perpendicular to the interface, and the carriers are distributed inside subbands, which correspond to the quantified energy levels inside the triangular quantum well.

The electrons constitute a quasi-two-dimensional electron gas, which exhibits high mobility due to the reduce interaction of the carriers with the impurities and to the extremely good quality of the interface, usually achieved using MBE.

The conduction-band structure of AlGaN/GaN heterostructure near the interface is shown in Fig. 2.8. In the ideal case , the GaN (at $z \geq 0$) is nominally undoped while the AlGaN/GaN ($z \leq 0$) is selectively doped and consists of a nominally undoped region ($0 \geq z \geq -d$) known as the "spacer" and an intentionally doped region ($z \leq -d$). As GaN has a higher affinity for electrons than AlGaN, electrons from the donors in the AlGaN are transferred to the GaN [59].

The electric field set up by the charge sheet confined at the interface causes a severe band bending due to an internal electric field in the GaN layer. The discontinuity of the conduction band at the heterojunction generates therefore a quasi-triangular potential barrier where the allowed states for motion normal to the interface are discrete in energy. The potential discontinuity depends on the mole fraction x of Al incorporated in the alloy since this fraction controls the energy gap of the wider bandgap $Al_xGa_{1-x}N$ material. The energy band structure of a $Al_xGa_{1-x}N/GaN$ heterojunction is shown in Fig. 2.8.

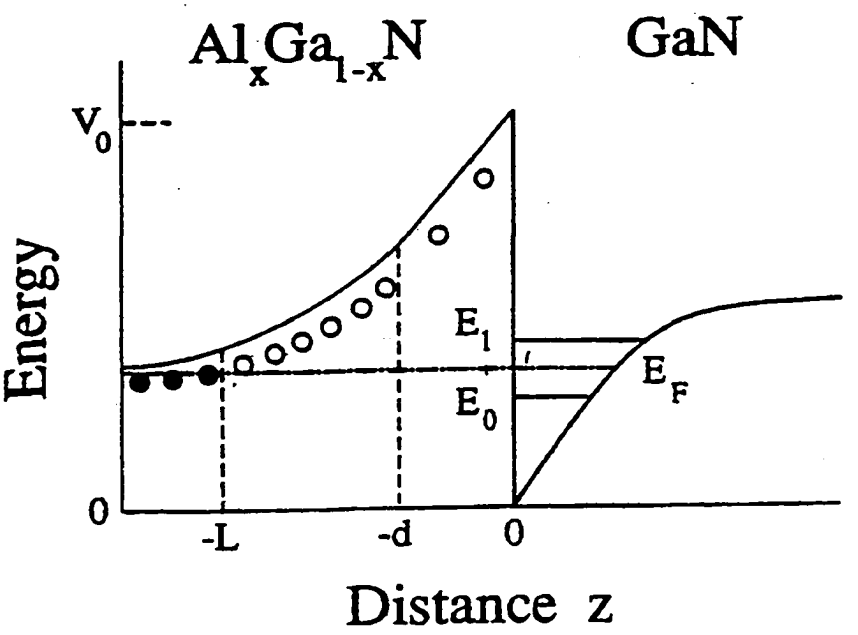

Fig. 2.8 Schematic diagram of the energy subbands in a singlest two energy bands of $Al_xGa_{1-x}N/GaN$ heterojunction [59].

At equilibrium, all of the carriers transferred to the GaN are distributed in the subbands of the conduction channel. When a bias is applied between source and drain, current flows along the quantum channel, under the control of the gate voltage.

The positively charge donors in the $Al_xGa_{1-x}N$ produce an electric field that creates a potential well in the GaN, confining the electrons to a narrow strip at the interface and leading to a quantization of the energy-band structure into subbands. At equilibrium, the transfer of electrons from the $Al_xGa_{1-x}N$ to the GaN is determined by the equations [59,60]:

$$V_0 - \frac{4\pi e^2}{\varepsilon_s}(N_s + N_{dep})d - \frac{4\pi e^2}{2\varepsilon_s}\frac{(N_s + N_{dep})^2}{N_l} = E_F, \qquad (2.21)$$

where V_0, E_F and spacer width d are shown in Fig. 2.9. N_s is the electron concentration in the GaN, N_{dep} is the concentration of residual charged impurities in the GaN, N_I is the bulk concentration of so-called "remote donors" in the $Al_xGa_{1-x}N$ and ε_s is the static dielectric constant of GaN. Assuming that only one subband is occupied, the Fermi energy E_f is given by,

$$E_F = E_0 + \frac{\pi\hbar^2}{m^*} N_s, \tag{2.22}$$

where $\frac{\pi\hbar^2}{m^*}$ is the two-dimensional density of states in GaN.

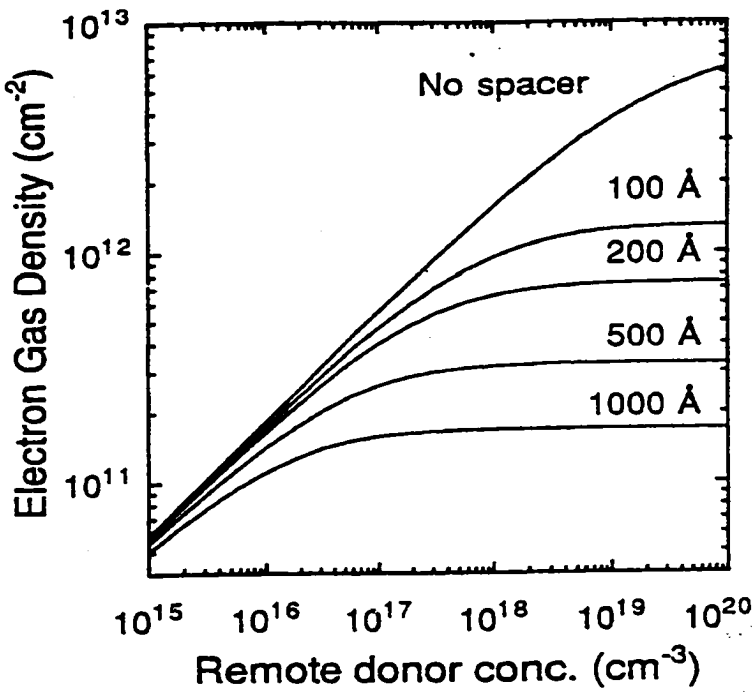

Fig. 2.9 2DEG density in GaN as a function of $Al_{0.15}Ga_{0.85}N$ doping concentration (N1) for different spacer width [59].

In Fig. 2.9, the two-dimensional electron-gas density is shown as a function of the $Al_xGa_{1-x}N$ doping level for an $Al_xGa_{1-x}N/GaN$ Structure with a variety of spacer widths. All of the above features have to be carefully considered for carrier transport analysis in such HEMTs.

In most cases, N_{depl}, the product of the bulk residual charged impurity concentration and the effective width of the electron gas can be made at least two orders of magnitude smaller than N_S, and thus can be neglected.

2. 4 Introduction to Signal Distortion

Distortion is classified as a change in the temporal shape of a signal. This can occur either due to the properties of the medium in which the signal propagates or be the result of physical influences caused by the electronic devices and circuits used for signal processing. In general, distortion can be categorized as either linear or nonlinear in nature. Linear distortion includes processes that may change the level or phase of a signal or its individual frequency components, but not add any new components. Ordinarily these processes would be described in terms of their effects such as the "frequency response" or "phase shift," rather than the generic "linear distortion" classification.

A nonlinear system (or portion of a system) is one whose output is not simply proportional to its input. Instead the output is related to the input in terms of some nonlinear equation that may contain squared or higher order factors involving the input variable. All systems exhibit nonlinear behavior at their limits (or there would be no "limits" in physical systems). For example, an amplifier has a maximum output voltage

determined by its power supply, and a loudspeaker has a maximum displacement determined by its construction.

2.4.1 Harmonic and InterModulation Distortion

In a linear network, a sinusoid passes through unchanged apart from its magnitude and phase. No new frequency components are generated. In a non-linear circuit, not only can the amplitude and phase of the input frequency components be changed but new frequency components are generated. These new components are called distortion products.

When multiple tones are applied to a non-linear network, not only are harmonics of each tone generated, but also distortion components that consist of a sum or difference of integer multiples of the input tones. These intermodulation products restrict the usefulness of the idea of superposition, since they are only present when the input tones are applied to the system together. This is also known as intermodulation distortion (IMD), since the result is similar to multiplying two sinusoids together.

Here, the harmonic and intermodulation products arising from two input tones are illustrated in Fig. 2.10, where the input frequencies are at 2.9MHz and 3.5MHz. The harmonics are denoted by frequencies such as $2f_1$, $3f_1$ etc. The intermodulation products are denoted by frequencies such as $2f_1-f_2$, $2f_1+f_2$. The order of a distortion component is its order given by m+n. From Fig. 2.10, it can be seen that certain third order difference intermodulation products are particularly serious, since they are close to the wanted tones from which they were generated. In a multi-channel communication environment, these

intermodulation products give rise to interference signals that can compromise receiver sensitivity.

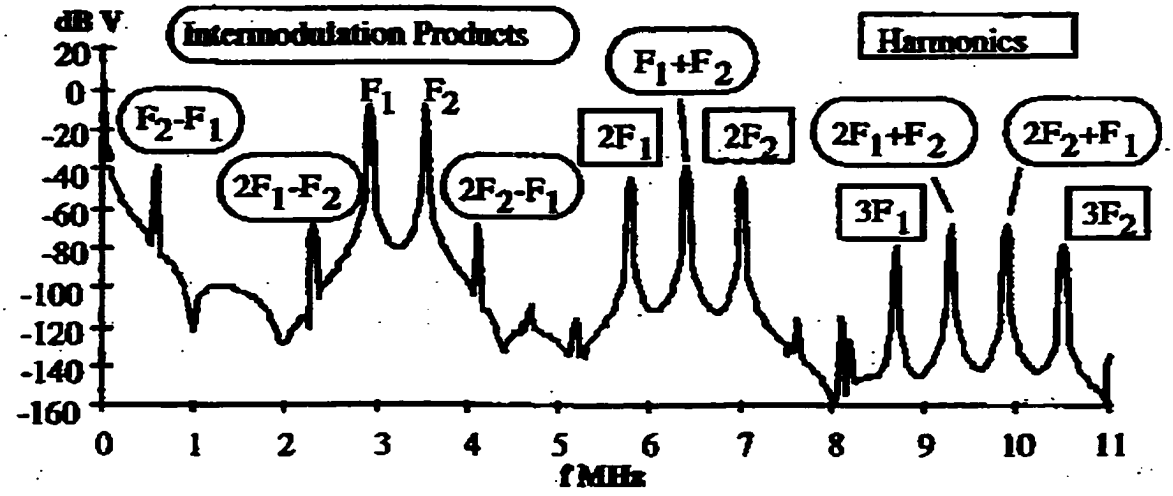

Fig. 2.10 A typical spectrum showing harmonic and intermodulation distortion.

2.4.2 1dB Compression and Intercept Points

Fig. 2.11 schematically shows IMD, IP3, 1db and dynamic range. And this type of graph leads to a number of key definitions.

1dB Compression The point at which the fundamental curve deviates from its linear extrapolation by 1dB. It may be quoted at the input or output signal level. It provides knowledge of the boundary between approximately linear behavior and rapidly increasing non-linearity.

Dynamic Range The amplitude range over which a mixer can operate without degradation of performance. It is dictated by the conversion compression point and the noise figure of the mixer. Since the thermal noise of each mixer is about the same, the conversion compression point normally determines the mixer's dynamic range.

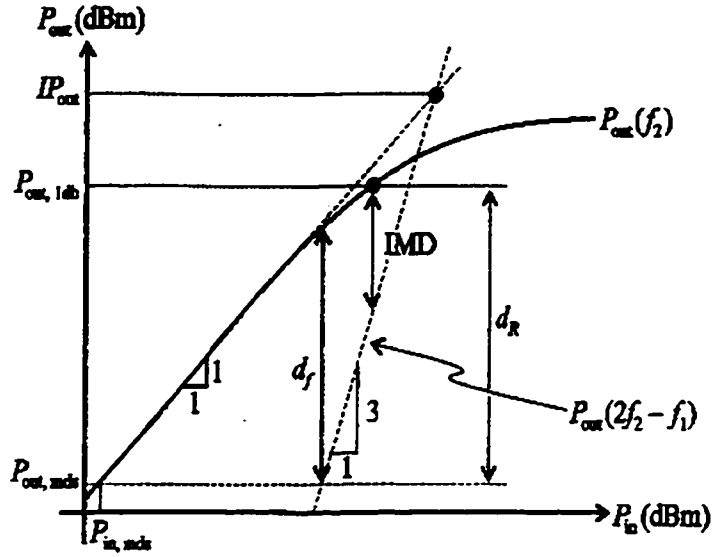

Fig. 2.11 Schematic of IMD, IP3, 1dB and dynamic range.

Intercept Point The point at which the fundamental response and the third-order spurious response curves intercept. It is often used to predict the two-tone, third-order suppression of a mixer. The higher the intercept point, the better the third-order suppression. Relative to the input, the intercept point is typically 9 to 11 dB higher than the conversion compression point.

Third-order Intercept Point (IP3) The point is defined as the theoretical level at which the intermodulation products are equal to the fundamental tone, these intermodulation products increase by 3dB when the fundamental goes up by 1dB. The third-order characteristic is quite important since this component is the strongest for systems subject to two inputs. A "close third-order" distortion occurs at twice the frequency of one stimulus minus one times the frequency of the other stimulus: at $(2f_1-f_2)$ or $(2f_2-f_1)$. Therefore, if the two stimulus frequencies are "x" Hz away from each other,

the close third order products will appear at "x" Hz to the outsides of the pair of stimulus frequencies.

Decibel Scale (dB) A logarithmic scale represents the logarithmic ratio between any two power levels. Taking the load P_L and source P_S power as examples, the decibel scale is defined:

$$dB = 10\log_{10}(\frac{P_L}{P_S}) \ , \tag{2.23}$$

where P_L and source P_S are measured in Watts.

Decibels are simple the ratio of two numbers and give no information about the absolute level of a signal; for example, 10W compared to 1W has the same decibel ratio as 100mW compared to 10mW. For absolute levels, a different scale (dBm) is used where the reference level is fixed at 1mW. The mathematic expression is like:

$$dBm = 10\log_{10}(\frac{P_L}{10^{-3}}) = 10\log_{10}(P_L) + 30 \ . \tag{2.24}$$

Fig. 2.12 show how the typical amplitude of the fundamental and second and third order sitortion components in the output of a non-linear circuit can vary with input signal level. The distortion components could be either harmonic or intermodulation. In the small input signal level region, the distortion components are proportional to the input signal amplitude (on a log or dB, scale) with a gradient equal to the order. As the signal level is increased, higher order distortion components tend to contribute significantly to lower order components and this causes erratic behavior of the distortion products and the saturation of the fundamental curve.

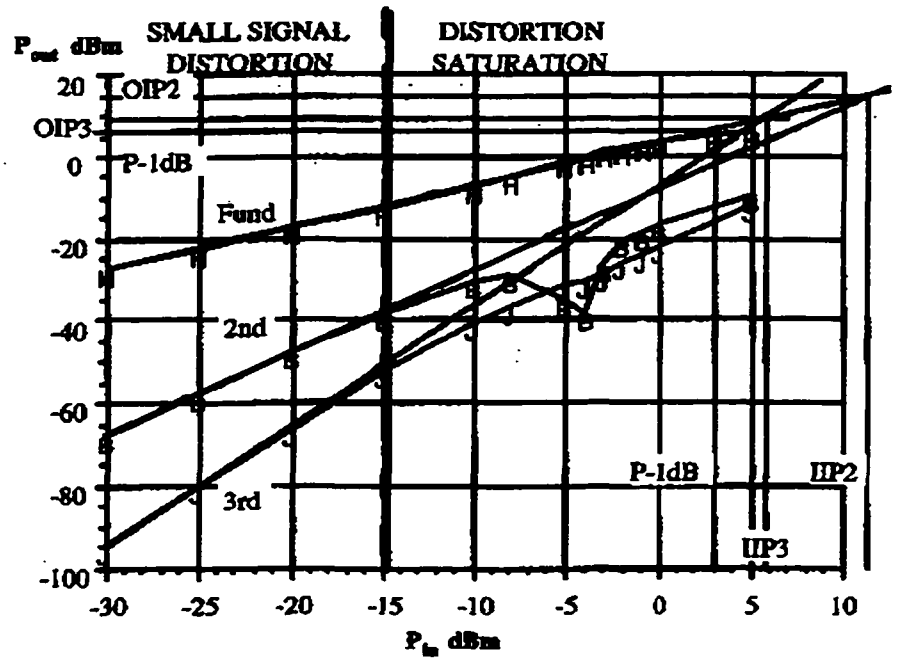

Fig. 2.12 Variation of distortion components with signal level showing input and output referred intercept points (IP2, IP3) and 1dB compression point (P_{1dB}).

CHAPTER 3

SIMULATION APPROCHES

3.1 Introduction to Simulation Approaches

The principal goal of semiconductor device simulations is to determine the behavior of terminal current and device voltage in response to an applied stimulus. The stimulus could either be an external bias, an optical excitation or a thermal perturbation as a function of time. The mathematical models to be used for device analysis should, in general, include the dynamics of free carriers within the bulk semiconductor, appropriate boundary conditions between semiconductor sections, the time dependent behavior at the contacts and surfaces and any applicable thermal exchanges within the semiconductor system.

A simple methodology used for describing the transport behavior in semiconductors is the Kinetic Approach. This approach uses the kinetics of an "average particle" with a simple treatment of collisions to describe its equation of motion [61]. According to this method, the semiconductor band structure is considered parabolic, which leads to a constant effective mass. And the particle is considered to be non-interacting, which implies low concentrations leading to a non-degenerate Maxwell-Boltzmann carrier distribution. However, the off-equilibrium effects are largely excluded, though this approach describes semiconductors microscopic properties reasonably.

The Boltzmann Transport Approach is an equation described by motion equation for the distribution function $f(r, p; t)$ of particle ensemble [62]. This distribution function f is the probability of finding a particle with the momentum p at a position r at time t.

By incorporating all of the internal scattering effects taking place over time, the Boltzmann Transport Equation (BTE) is able to describe non-equilibrium, transient effects correctly provided the scattering relationship can be characterized. Due to the inclusion of scattering, this approach represents a generalization of the Vlassov equations used for simulations of low-density plasmas. Usually, time-dependent perturbation theory based on the Fermi Golden rule is used to ascertain the scattering relationships. However, the Boltzmann equation is an integro-differential equation. For the majority of real systems, exact analytical solutions are not available. Usually, this approach is restricted to inherent assumptions, such as a simplified band structure and distribution function. Thus, this approach is no longer valid in the cases where simplified distribution do not exist, such as in very short dimensional structures or during ultrashort transient time intervals.

In order to correctly simulate semiconductor structures with very small dimensions, a statistical method known as the Monte Carlo approach was proposed to solve complicated mathematic problems [63] such as for cases when the assumptions of the BTE become unacceptable, or to describe phenomena involving ultrashort time scales. In the stochastic Monte Carlo approach, individual particles are randomly selected and their motion followed in space and time. The average ensemble behavior is subsequently determined by collecting enough information about the particles. The biggest advantage of this method is that, no fitting parameter (such as carrier mobility or diffusion coefficient) is required. Once the solution of the equation is being built up, any physical information required can be easily extracted. However, the approach is very

intensive computationally since a large number of particles are required to yield reliable statistics.

While the quantum nature of electron, such as quantum states and kinetics, becomes dominant, the Quantum Transport Approach is applied [64]. Such a treatment becomes necessary in problems where the spatial and temporal extents are similar to the de Broglie wavelength and the duration of scattering respectively. All variations of the quantum transport approaches are very complex and are presently needed in only a few of the devices of interest.

3.2 Theory of Microscopic Transport

The study of charge transport in semiconductors is of fundamental importance either for basic physics or for its device applications. In the semiclassical approximation, the transport of carriers in a semiconductor is described by the Boltzmann Transport Equation (BTE). The BTE describes the dynamic evolution of the distribution function, $f(\vec{r},\vec{k},t)$, under non-equilibrium conditions. The total rate of change of distribution function f can be expressed as:

$$\frac{\partial f}{\partial t} = -\vec{V}\cdot\nabla_r f - \frac{e\vec{F}}{\hbar}\cdot\nabla_k f + \left[\frac{\partial f}{\partial t}\right]_{collisions}, \tag{3.1}$$

where $\vec{F}$ is the applied external field, $\vec{V}$ is the drift velocity, and the last term is the change in occupancy "f" due to collisions and scattering. The approximations on which Boltzmann equation is based are: (i) the effective mass approximation, and (ii) weak coupling. The electron-phonon interaction is treated as a small perturbation on the

unperturbed Hamiltionian for the free electrons and lattice. The external perturbation does not affect the phonon subsystem.

In this equation, the first and second terms describe the effects of the density gradient and of the external electric field, respectively. The collision term involves an integral, which yields a complicated integro-differential form for the BTE. In this reason it is difficult to obtain a simple (or even complicated) analytical solutions except for very few cases, which are not applicable to real systems. Furthermore, since transport quantities are derived from the averages over many physical processes whose relative importance is not known a priori, the formulation of reliable microscopic models for the physical system under investigation is difficult [65].

Approximate analytical solutions involve either approximations on the form of the scattering rates, or assumptions on the distribution function. The two most used techniques are the Legendre polynomial expansion [66] and the displaced Maxwellian approximation [67]. Such approximations are very drastic in most of the cases of interest, and it is not clear whether the simulation results are due to the microscopic model or to mathematical approximations.

To determine the exact expression of distribution function in the Boltzmann transport equation, numerical algorithms, rather than analytical method, have been developed to meet the challenge. With the aid of modem large and fast computers, exact numerical solutions of the BTE can be obtained for microscopic physical models of considerable complexity in a relatively short computer execution time. The two most important numerical techniques are the iterative method [68] and the Monte Carlo technique [69].

The Monte Carlo technique is by far the more popular and accurate. Besides easier implementation, the technique offers the following advantages:

1. The microscopic interpretation of the physical details is quite transparent.
2. Stochastic calculation is achieved at a minimum level of difficulty while incorporating memory effects.
3. Time and space dependent phenomena can be easily simulated.
4. No arbitrary assumption regarding the distribution function needs to be made.
5. Complex geometries and boundary surfaces can easily be treated.

Monte Carlo is a statistical numerical method used for solving mathematical problems. It was born well before its application to the transport problems, and has been applied to a number of scientific fields. This method was first applied to transport in semiconductors by Kurosawa [69] to study steady-state hole transport in Ge. Fawcett et al. [70] extended this method for GaAs material where different scattering processes and a complex band structure needs to be incorporated. The physical interpretation of a numerical solution is the most important step in any simulation, and the Monte Carlo method is particularly useful to achieve this goal, since it permits the observation of simulated physical situations unattainable in experiments, or even the investigation of a nonexistent material in order to emphasize special features of phenomena under study.

3.3 Monte Carlo Method

The Monte Carlo method, as applied to charge transport in semiconductors, consists of simulation of the motion of one or more electrons inside the crystal, subject to the action of external forces due to applied electric, magnetic fields and given scattering

mechanisms. In the frame of semiclassical approximation, the motion consists alternately of free flights due to the drift electric field, and of instantaneous scattering events. Because the particles are treated as classical point-like objects, but the scattering rates are determined by quantum mechanical theory, the approach is categorized as being "semiclassical." The classical motion laws are also applied for the electron drift in the electric field during the free flight. The free flight time, the type of scattering event and the final electron state after the scattering are random quantities that are selected stochastically in accordance with some given probability distributions. This technique was proposed in 1966 and has been used extensively [65]. These distributions can be expressed in terms of the transition rates due to the various processes and the strength of the electric field. In practice, the physical distributions may be quite complex, though the generation by computer of random number sequences with equal probability over some finite range is relatively simple. The manipulation can be simplified by mapping the complex distributions on to a simple pseudo-random distribution [71]; the most convenient pseudo-random distribution is the uniform distribution, which is readily available on most computer systems.

In general, if p(q) and p(r) are the respective probability densities, associated with q in the physical distribution and r in the pseudo-random distribution, then:

$$\int_0^q p(q')\,dq' = \int_0^r p(r')\,dr' \quad . \tag{3.2}$$

In a uniform distribution p(r) = 1, so we get:

$$r = \int_0^q p(q')\,dq' \quad . \tag{3.3}$$

Hence, provided that this integral can be evaluated in a simple closed analytic form, inversion will yield a random value for the physical variable q in terms of the uniformly distributed random number r. As a consequence, any Monte Carlo method relies on the generation of a sequence of uniformly distributed random numbers corresponding to various random processes involved.

The single electron technique mainly allows one to compute the average drift velocity and the mean energy as a function of the electric field, making an average over a simulation time sufficiently long to be representative of the behavior of all the carriers contributing to the transport. This means that the process is assumed to be ergodic; therefore, the results are valid only for steady-state conditions, homogeneous phenomenon. For transient and non-stationary/non-homogeneous process, it is necessary to simulate the motion of an ensemble of charge carriers and evaluate over the time the ensemble average of the physical quantities of interest. The method is known as Ensemble Monte Carlo (EMC) method, and the program flow is summarized below.

3.3.1 Initial Conditions

As a start point, parameters related with the simulation system are initialized. They include simulation device dimensions, material characterization parameters, values of physical quantities and simulation conditions such as lattice temperature, electric field and terminal bias. The parameters that control the simulation program are also defined, such as the number of electrons simulated, duration of each subhistory, total simulation time, the desired precision of results and so on. The scattering rates as a function of electron energy are calculated, normalized and stored in a tabulated form.

The initial conditions of motion are also set in this step. Invoking uniformly distributed random numbers generates the initial position, momentum and energy of the simulated particles. Initially, all the electrons reside in the lowest valley and are assumed to be in a state of initial thermal equilibrium. For simulations involving photoexcitation, the initial state lies in the lowest direct valley with an energy equal to the excess energy of the external excitation. The momentum at this initial energy is usually distributed randomly. For situations involving electrical carrier injection from a contact, the distributions would be suitably modified.

3.3.2 Flight Duration

This step is to determine the free flight time for each electron. The flight time depends on the scattering probability. Suppose that the transition rates between two wavevector states k and k' is given by S_i, where i indicates the type of scattering process. The probability per unit time that the electron will drift for a time t in an electric field E, and then be scattered, is given by,

$$p(t) = \lambda[\vec{k}(t)]\exp\{-\int_0^t \lambda[\vec{k}(t')]dt'\}, \tag{3.4}$$

where: $\vec{k}(t) = \vec{k_0} + e\vec{F}t/h, \lambda(\vec{k}) = \sum_i \lambda_i(k)$. Here, $\lambda_i(\vec{k})$ is the total transition rate from the state $\vec{k}$, due to the i-th process, and $\vec{k_0}$ is the wavevector at the beginning of flight (t=0), i.e., is the final state after the previous scattering event. If the total scattering $\lambda(\vec{k})$ is a constant equal to Γ, equation 3.4 becomes:

$$p(t) = \Gamma\exp\{-\Gamma t\}. \tag{3.5}$$

For a uniform distribution of random numbers r, p(r) = 1, one can easily show [65]:

$$r = \int_0^q p(q')\,dq' , \tag{3.6}$$

which yields,

$$r = \int_0^t \Gamma \exp(-\Gamma t')dt' = 1 - \exp(-\Gamma t) . \tag{3.7}$$

In general, since $\lambda(\vec{k})$ is not nearly constant, a fictitious scattering rate, called self-scattering, is introduced in such a way that the $\vec{k}$ dependence of the self-scattering makes Γ constant [72].

The self-scattering $\lambda_v(\vec{k})$ is only a virtual event that does not alter the state of the electron and allows one to use the easy flight time selection rule give by equation (3.7). Thus, the total scattering rate for the electron, which includes the virtual process, is simplied as:

$$\lambda_T(\vec{k}) = \lambda\,(\vec{k}) + \lambda_v(\vec{k}) = \Gamma_{max} . \tag{3.8}$$

Eq.(3.7) now reduces to the elementary form

$$r = 1 - e^{-\Gamma_{max} t} . \tag{3.9}$$

Eventually, the expression for t is:

$$t = -\frac{1}{\Gamma_{max}} \ln(1-r) = -\frac{1}{\Gamma_{max}} \ln(r) . \tag{3.10}$$

Since r is uniformly distributed, $\ln(1-r)$ and $\ln(r)$ are equivalent. Thus, flight time t can be determined from the uniformly distributed random number r. Γ_{max} is chosen

to be the maximum value of $\lambda(\vec{k})$ in the region of k space of interest. This is done to avoid negative values for $\lambda_\nu(\vec{k})$.

The electrons can drift freely by the influence of the electric field. During the free flight, the electron wave vector k changes continuously according to Newton's law of motion for the frictionless regime. In the absence of magnetic fields or any thermal gradients, the relationship between wave vector and the energy is given:

$$\frac{\partial k}{\partial t} = \frac{eE}{\hbar}. \tag{3.11}$$

The scattering rates for collision mechanisms between three-dimensional states are introduced. The non-parabolicity of the bands is included by relating the energy E to the wavevector k through the following relationship [70]:

$$\frac{\hbar^2 k^2}{2m^*} = E(1+\alpha E). \tag{3.12}$$

Parameters of interest, such as electronic position, momenta and energy, are recorded for the next events. After the free flight, a random number is used to select a scattering event for each electron.

3.3.3 Choice of Scattering Mechanism

The scattering rates of the various mechanisms are tabulated as function of energy and normalized to Γ_{max}. Thus for a given E, the normalized probability $P_j(E)$ for the scattering mechanism j is $\lambda_j(E)/\Gamma_{max}$. The selection is made by generating a random number between 0 and 1, but greater than 0 to avoid singularities. If the inequality: $\sum_{i=1}^{j-1} P_i(E) < r < \sum_{i=1}^{j} P_i(E)$ holds, then the jth scattering mechanism is selected. If

$r > \sum_{i=1}^{N} P_i(E)$, where N is the total number of scattering mechanisms, then a self-scattering occurs.

The scattering event is chosen following the procedure illustrated in the flow-chart of Fig. 3.1. The physical expressions and the details for all the scattering mechanism of AlGaN/GaN system are discussed in section 3.4.

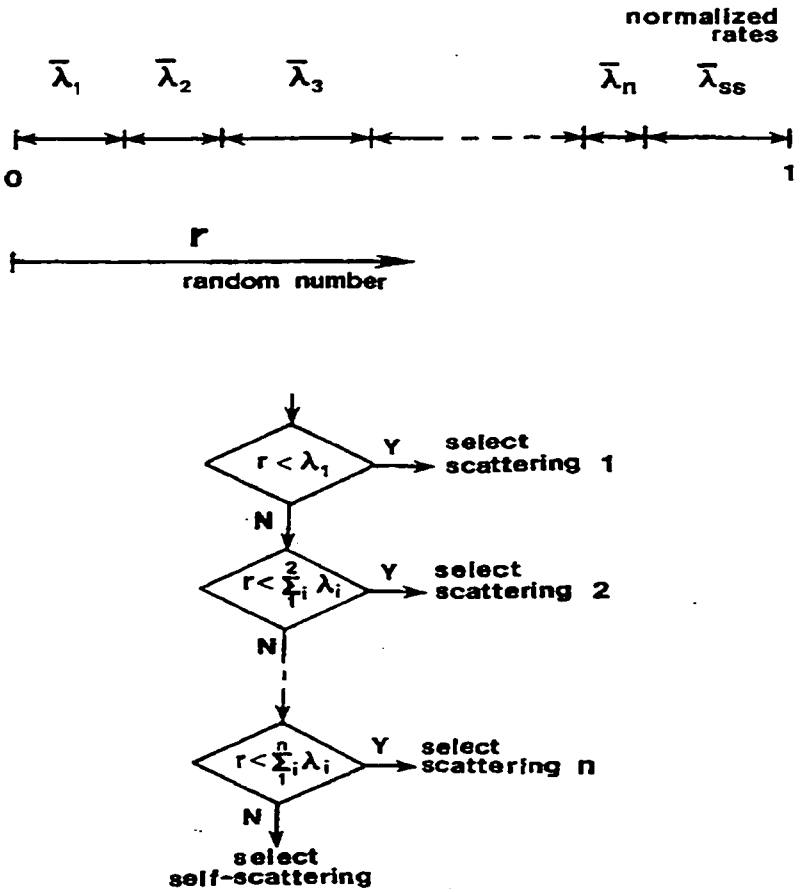

Fig. 3.1 Flow-chart of scattering selection in EMC [73].

3.3.4 Choice of State after Scattering

Once the scattering mechanism that caused the end of the flight has been determined, the new state after the scattering of the electron, k', needs to be chosen. If a self-scattering has occurred, the electron momentum and motion path remain unperturbed. In this case, k' is taken equal to k, the flight is not terminated and a new flight time Δt is chosen and added to t. This goes on until a real scattering event is selected. When a real scattering event occurs, k' is chosen stochastically according to the differential cross-section of that particular mechanism. Energy of the electron is altered if an inelastic process such as polar optical or intervalley scattering has occurred. On the other hand, for ionized impurity scattering or acoustic scattering, the final energy equals the initial energy because of the elastic nature of the collision. A change in momentum will always occur; however, the scattering mechanism could be either a momentum randomizing (acoustic, intervalley scattering) or non-momentum randomizing (polar optical, ionized impurity scattering) process. Optical phonons add or extract a constant quanta of energy $h\omega$ through emission or absorption. Such a fixed energy quanta is a direct consequence of the $\omega - k$ dispersion curves for optical phonons in semiconductor materials. The determination of the new wave vector k after the phonon scattering requires further generation of random numbers. These random numbers are used to determine the azimuthal angle θ and angle ϕ according to the angular dependence of the selected scattering mechanism. The angle ϕ after the scattering can take any value between 0 to 2π with equal probability. So ϕ is chosen using a random number r as:

$$\phi = 2\pi r . \tag{3.13}$$

On the other hand, the angle theta depends on the nature of the scattering process. For momentum randomizing processes, θ is given by:

$$r = \frac{1}{2}(1 - \cos\theta). \tag{3.14}$$

For other scattering mechanisms, that have directional dependence $P(\theta)$, one can select θ by generating a random number and mapping the distribution $P(\theta)$ to a uniform distribution [74].

After the scattering event, the momentum and energy of the electron are updated. The electron position remains unchanged as the collisions are considered to be instantaneous. The electron begins its next flight and scatter mechanism repeats until the end of the simulation.

3.4 Scattering Mechanisms in GaN/AlGaN

In a perfect crystal, the motion of electrons is free. The application of an external field uniformly accelerates the electron, linearly increasing its drift velocity with time in the direction of the field. Such a linear increase in drift velocity with time is not observed in any real crystal. The average electron drift velocity reaches a limiting value, which at low fields is proportional to the magnitude of the field [75]. The limit is set by the interaction of the electron with imperfections in the crystal though the so-called scattering process. Scattering theory is fundamental for electron transport in solids. The interaction of carriers in a solid with imperfections of the crystal lattice such as impurities, lattice defect, lattice vibrations, strain [76] and alloy [77] contributed to scattering [78]. In this section, the scattering theory will be presented along with results for GaN/AlGaN two-dimensional electron gas at the interface.

3.4.1 General Scattering Theory

The most important scattering sources that determine electronic transitions are phonons, ionized impurities and interactions with other electrons and interface roughness scattering. The transitions of interest for electron transport in semiconductors can be classified as intervalley, if both initial and final states of the electron lie in the same valley, or intervalley, if the final state lies in a valley different from that of the initial valley.

In the Born approximation, the scattering process only consists of a transition between two definite momentum states for the electron involved. A central idea in scattering theory is the scattering probability per unit time $S(k,k')$, which is calculated using Fermi's Golden rule [79].

$$S(k,k') = \frac{2\pi}{\hbar} |< k \mid H' \mid k' >|^2 \, \delta(E'-E), \tag{3.15}$$

where $|< k \mid H' \mid k' >|^2$ is the matrix element of H' between the initial and final states and the δ-function expresses the conservation of energy, E and E' being the initial and final energy of the entire gas of electrons and phonons, respectively. For a transition due to a phonon with wavevector q and frequency w_q, we have:

$$E'-E = \pm\hbar w_q, \tag{3.16}$$

$$k - k' \pm q = G, \tag{3.17}$$

where G is a reciprocal lattice vector. When $G \neq 0$, we have an Umklapp process. By integrating over all possible final states k', the total scattering rate out of state k is obtained as:

$$\Gamma(k) = \frac{2V}{8\pi^3} \int dk' \int d\phi \int d\theta S(k,k'') k'^2 \sin\theta, \tag{3.18}$$

where V is the volume of the crystal, θ is the angle between k and k', and ϕ is the azimuthal angle. The factor of "2" comes from the spin-degeneracy of the electronic states. The angular dependence of the scattering is obtained directly from the angular dependence of $S(k,k')$. For non-Umklapp process, the matrix element in equation 3.15 can be written as [65]

$$|<k|H'|k'>|^2 = V(q)G(k,k'). \tag{3.19}$$

So that the transition rate is

$$S(k,k') = \frac{2\pi}{\hbar} V(q)G(k,k')\delta(E'-E), \tag{3.20}$$

where V(q) contains the dependence upon $q = k'-k$ of the square Fourier transform of the interaction potential. The manner in which V(q) depends on the momentum transfer depends on the nature of scattering.

Now we consider the different scattering mechanisms individually. The electron-phonon interaction is due to the deformation associated with phonon vibrations of the otherwise perfect crystal. The covalent semiconductors it is described in the framework of the deformation-potential method [80] for both acoustic and optical phonons. Impurities can be ionized or neutral. In the former case the interaction is of long-range Coulomb type, while in the latter, the interaction is of much shorter range. The overall effect of neutral impurities is, in general, much weaker. Hence the neutral impurities are not included in the present Monte Carlo calculations. The electron-electron collisions are also not considered for the simulation process since both carrier energy and momentum are collectively preserved.

Screening of the polar optical and interface ion interactions was evaluated within the random phase, zero-frequency approximation [81] that requires the evaluation of a

wavevector-dependent form factor. Finally, both intra- and interband transitions were accounted for in the numerical transport simulations. Treatment of the interface roughness scattering was based on a simple Gaussian model for the autocovariance function [40], rather than the exponential dependence used by Goodnick et al. for silicon [41]. More complicated treatments of discrete AlGaN islands at the interface have been suggested to include localization effects [47], but were not used here for computational simplicity.

Phonon scattering plays an important role in limiting the electron mobility in III-V semiconductors. The three most important phonon-scattering processes are deformation potential acoustic, piezoelectric acoustic and polar optical. All three of these processes have been studied extensively in bulk semiconductors.

3.4.2 Acoustic Phonon Scattering

The energy change in acoustic phonon scattering is negligible and it is treated as an elastic process. However, for nonlinear transport problems in low fields or temperature, the small energy dissipation is needed to establish a smooth distribution function. The squared matrix element V(q) (equation 3.19) is given by [65],

$$V(q) = \frac{E_a^2 \hbar q}{\rho s}(N_q + \frac{1}{2} \pm \frac{1}{2}), \tag{3.22}$$

with the plus (minus) sign referring to phonon emission (absorption) process. E_a is the acoustic deformation potential, ρ the crystal density, s the speed of sound and N_q the Bose-Einstein distribution given by:

$$N_q = (\exp[\frac{\hbar w}{kT}] - 1)^{-1}, \tag{3.23}$$

where $\hbar w$ is the phonon energy. The acoustic phonon scattering rate can be determined by substituting V(q) in equation 3.23 and using equation 3.12 for integrating over all k'.

3.4.3 Polar Optical Phonon Scattering

In optical phonon mode of vibration the two oppositely charged unit cells oscillate out of phase. The displacement during the oscillation sets up a polarization field that scatters the electron. The square of the matrix element for this process is given by [65]:

$$V(q) = \frac{\pi e^2}{\hbar \varepsilon_0 q^2} \frac{\hbar w}{2} (N_q + \frac{1}{2} \pm \frac{1}{2}), \tag{3.24}$$

where $\varepsilon(\infty)$ and $\varepsilon(0)$ at the high frequency and static dielectric constants respectively. N_q is given by the Bose-Einstein distribution.

3.4.4 Non-polar Optical Phonon Scattering

The non-polar optical phonons generate a short range potential that causes a shift in the electronic band states. In the long wavelength optical mode of vibration, one set of atoms moves as a body against the second set of atoms, which creates a strain in the lattice. The scattering of electrons by this strain is known as deformation potential scattering. The square of matrix element is given by:

$$V(q) = \frac{D_a^2 \hbar^2}{2\rho \hbar w} (N_q + \frac{1}{2} \pm \frac{1}{2}), \tag{3.25}$$

where D_0 is the deformation optical potential.

3.4.5 Intervalley Phonon Scattering

Intervalley phonon scattering is an important scattering mechanism for multiple valley materials. In a multi-valley model, electrons can undergo transitions between states in two different equivalent or non-equivalent valleys after scattering with large momentum phonons. Considering two conduction band valleys involved in the transition, the phonon wavevector is approximately constant and given by the distance in the Brillouin zone between the minim of the initial and final valleys. The energy involved in the transition is also approximately constant, and intervalley scattering can be formally treated in the same way as intravalley optical phonon scattering with the deformation potential interaction.

The transitions between different valleys involve a large amount of momentum transfer so that the polar interactions play a negligible role. The wave-vector q of the phonons causing the transitions is nearly the same as the distance between the minima of the initial and final valley in the Brillouin zone. This fixes q for a given pair of valleys so that the energy change in these transitions is constant for a given phonon mode. Consequently, the intervalley transitions can also be treated using the deformation potential concept. The squared matrix element is given by,

$$V(q) = \frac{D_{ij}^2 \hbar^2}{2\rho\hbar w}(N_q + \frac{1}{2} \pm \frac{1}{2}), \tag{3.26}$$

where D_{ij} is the deformation potential for scattering from the i^{th} valley to the j^{th} valley induced by a phonon of energy $\hbar w$.

If scattering between the central and satellite valley occurs, the electrons must acquire at least an energy Δ before the transition becomes possible. However, in the satellite valley the electron energy is measured from its minimum, so it is necessary to

add Δ to the electron energy if scattering from the satellite to the central valley occurs. Such nonequivalent intervalley transitions are shown in Fig. 3.2.

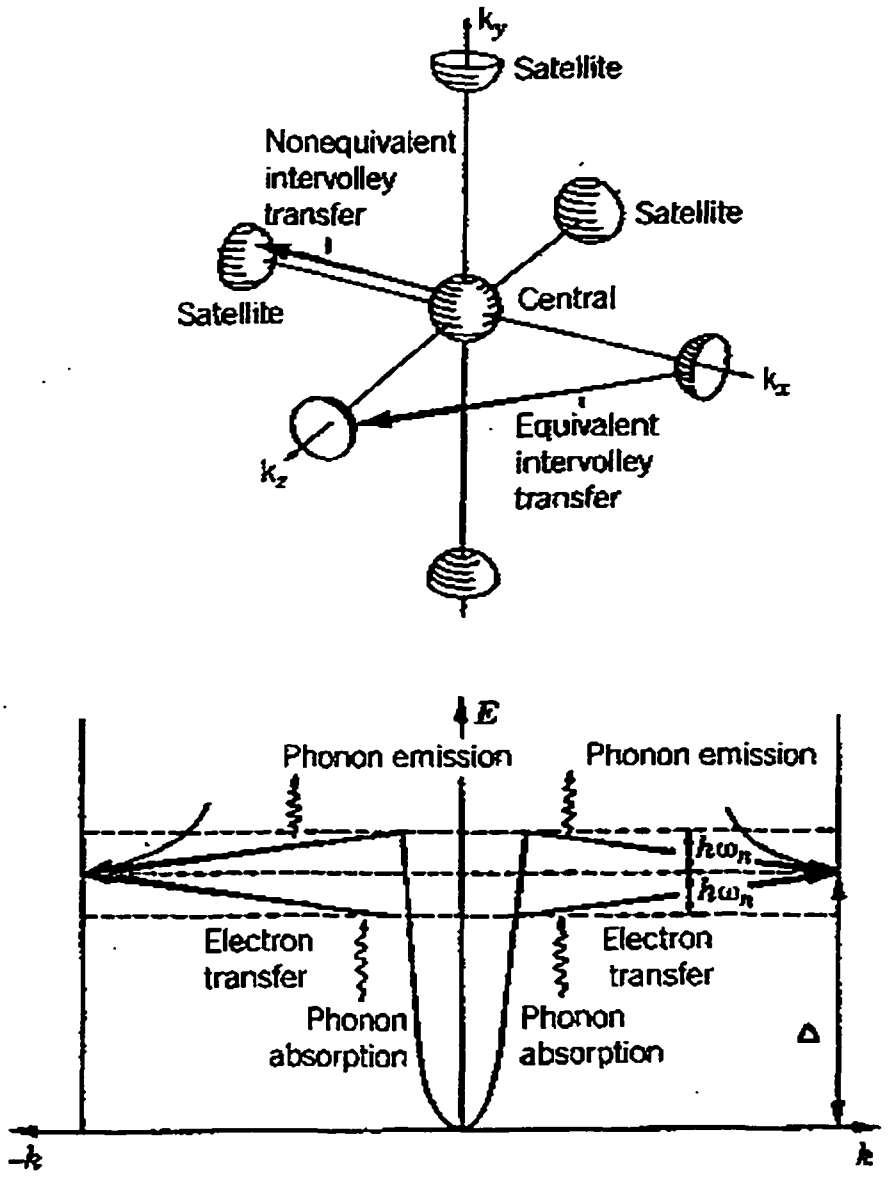

Fig. 3.2 Intervalley transitions on GaN [82].

For the sake of simplicity, one-way transitions are shown. The reverse transitions also occur with phonon emission or absorption changing to absorption or emission.

3.4.6 Ionized Impurity Scattering

The ionized impurity scattering is elastic in nature and cannot control the transport by itself in the presence of an external field. It must be accompanied by some dissipative scattering mechanism to obtain the proper energy distribution. The scattering source for an ionized impurity is a screened Coulombic potential. The square matrix element in the Brooks-Herring case is given by [83,84],

$$V(q) = \frac{NZ^2e^4}{(4\pi\varepsilon)^2(q^2+\beta^2)^2}, \tag{3.27}$$

where Z is the number of unit charge in the impurity, and β is a constant screening parameter.

3.5 Scattering with Electron Quantization

The above discussion assumed that the electrons were capable of unimpeded motion in all three directions within the semiconductor bulk. However, for analyzing electron motion and their mobilities in MOSFET structures or HEMTs, one needs to include the effect of constrained motion in one of the three directions. This occurs because the electrons in a HEMT (or MOSFET) move laterally from the source to drain within a very narrow inversion channel that is formed at the semiconductor-oxide interface. This channel is typically on the order of 10-20 nm, which is on the order of the typical deBroglie length of a free electron. The thickness of the channel is dependent on the transverse field set up by the applied gate voltage and can reduce the channel width at

higher gate voltages. In such a situation, the electron can no longer be described as a free particle, and its plane-wave description has to be modified. This is usually done by treating its lateral motion parallel to the interface as a usual classical particle, but incorporating quantization effects aiong the third direction. Such electron quantization has been discussed in detail [85]. Briefly it leads to the following effects:

(a) Modification of the wavefunction from a three dimensional electron plane wave to a two-dimensional electron plane wave modulated by an envelope function along the constraining direction. Thus, the wavefunction changes from

$$\Psi(x,y,z) = \frac{1}{\sqrt{(V)}} \exp[-k_x x] \exp[-k_y y] \exp[-k_z z] \ , \tag{3.28}$$

to

$$\Psi(x,y,z) = \frac{1}{\sqrt{(A L_z)}} \exp[-k_x x] \exp[-k_y y] \ F_j(z) \ , \tag{3.29}$$

where Fj(z) is a suitable envelope function for electrons in the jth subband. As a result, the modified wavefunction needs to be used in the calculation of all the scattering rates. The matrix elements also change since the initial and final states are now described by two-dimensional wavefunctions. The two-dimensional wavefunction given by (3.29) have to satisfy the Schrodinger wave equation. Now for the HEMT device, the interface can be represented by a potential barrier at z = 0 due to the discontinuity between the conduction band of GaN and AlGaN. In addition, the applied gate voltage produces a perpendicular field along the longitudinal z-direction. This gives rise to a potential that varies linearly with distance away from the interface and into the GaN material. A good analytical approximation for the envelope function F(z) based on the above potential has been worked out [40,86]and yields,

$$F_1(z) = \sqrt{\frac{b_o^3}{2}}\, z \exp[-\frac{b_o z}{2}] \ ,$$

$$where\ b_o = \frac{33\, m^* e^2}{8\_\hbar^2}\ [n_s + \frac{32}{11} N_b\ ]^{1/3} \ , \tag{3.30}$$

and

$$F_2(z) = \sqrt{\frac{3 b_1^5}{2[b_o^2 - b_o b_1 + b_1^2]}}\ [z - \frac{(b_o + b_1) z^2}{6}] \exp[-\frac{b_1 z}{2}] \ , \tag{3.31}$$

with b_1=0.754 b_o, N_b the background HEMT doping, and ns is the inversion channel density.

(b) Quantization of the electron energies and the formation of a set of discrete subbands. The subbands result from the quantization, just as full three-dimensional quantization in an atom leads to discrete electron energies. The difference though, is that instead of complete energy discretization, a continuum of energies results in the two directions in which motion is allowed, while a discrete subband level forms due to the quantized along the z-direction. Thus, the total energy E(k) as a function of the electron wavevector k becomes,

$$E(k_x, k_y, k_z) = \frac{\hbar^2 (k_x^2 + k_y^2)}{2m} + E_{oj} \ , \tag{3.32}$$

where E_{oj} is the discrete energy of the j^{th} subband. According to the model given above [40,86], the subband energies are given in terms of the longitudinal electric field Fg due to the gate voltage as,

$$E_{oj} = [\frac{\hbar^2}{2m}]^{1/3}\ [\frac{3}{2} e \pi F_g (\ j + \frac{3}{4}\ )]^{2/3} \ . \tag{3.33}$$

(c) Finally, due to quantization and the formation of subbands, the scattering becomes somewhat more complicated. In addition to scattering processes within each subband, due to either phonon emission, absorption events, or ionized impurities, one also needs to consider intersubband scattering. For intrasubband processes, the initial and final energy states of an electron lie within the same jth subband. However, for an intervalley scattering event, the electron transitions from the jth initial state to a new state in the ith subband. This, in principle, is not more difficult but simply requires a more complicated tracking based on a larger scattering table. Also, an additional interface roughness scattering process needs to be included. This scattering mechanism arises because the inversion electrons in an HEMT move in close proximity to the interface. Undulations at the atomic level, due to variations in the positioning of GaN and AlGaN atoms at the boundary, produce a scattering potential. Such interface roughness scattering can be especially important at high gate voltages since the inversion electrons are then tightly clustered close to the interface.

The details of the various scattering rates for treating such two-dimensional electron quantization have been worked out in the literature [87-90]. The formulae and equations given in the various references have been applied to GaAs HEMTs, and Si MOSFET structures, but not commonly to GaN HEMT devices. Here, the available results [87-90] were used, and suitable parameter changes were made for simulations of GaN HEMTs.

3.6 Implementation of the EMC

The flow-chart in Fig. 3.3 shows a general self-consistent Ensemble Monte Carlo algorithm. An initial distribution of position and momentum of the electrons inside the device is assumed at the beginning. After a first solution of Poisson's equation, the dynamics of all the electrons is evaluated in parallel, for a simulation time T_s. During this

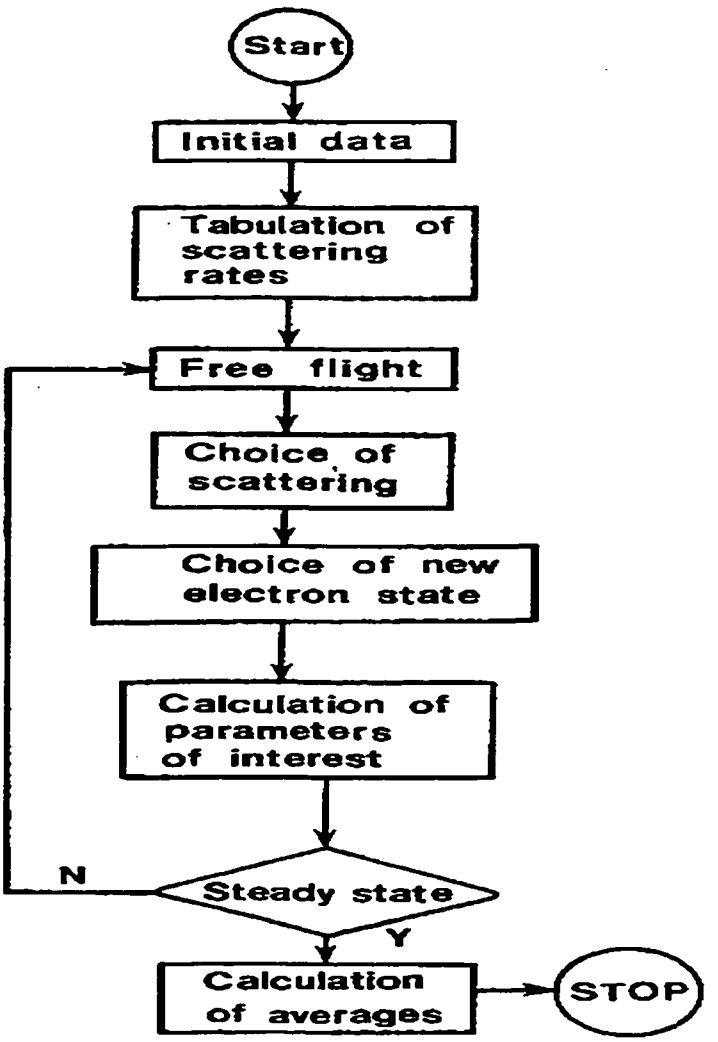

Fig. 3.3 The schematic flow-charts of a device Ensemble Monte Carlo method [73].

time interval scattering events occur randomly, using the same procedure discussed earlier, and the possible interactions while the boundaries are monitored. Then, Poisson's equation is solved again and the self-consistent iterations are stopped when a steady-state is achieved.

Fig. 3.4 shows the basic EMC technique. Fig. 3.4a shows the actual electron path in two dimensions, under the influence of a large external field. It is composed of eight segments of a parabola corresponding to the eight free flights. Fig. 3.4b shows the same eight events as heavy line segments in momentum space. These heavy lines are interfaced by light lines representing the changes of momentum in each scattering event. Fig. 3.4c gives the velocity of the carrier averaged at the n^{th} point over all previous (n-1) paths [91]. This average velocity approaches the drift velocity (dash-dotted line) when enough paths are taken. The drift velocity is a direct measure of mobility.

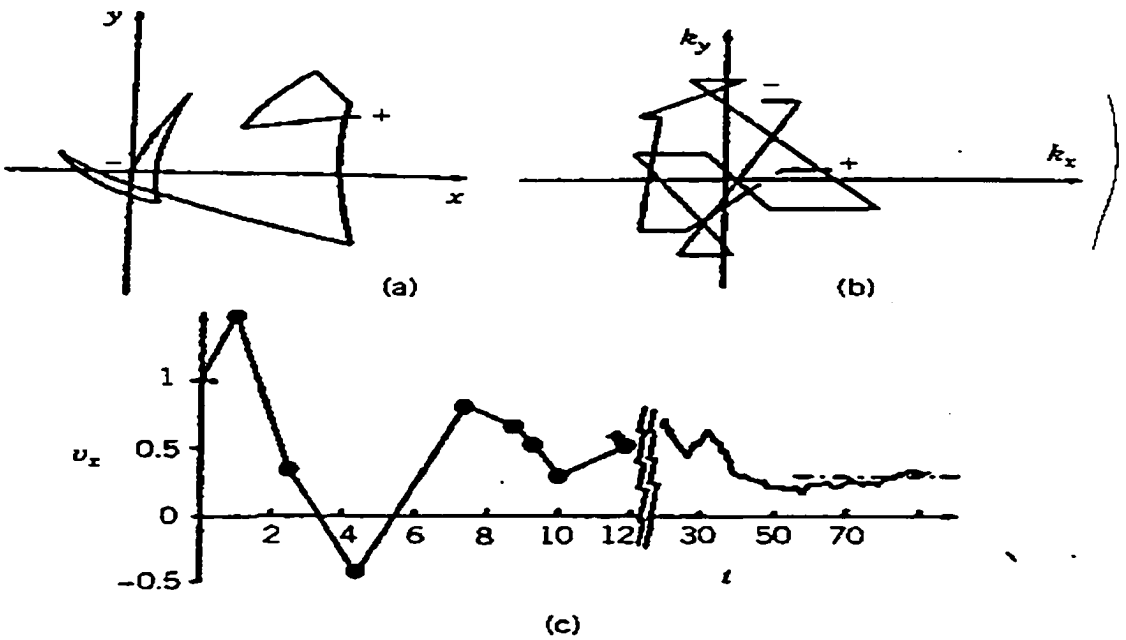

Fig.3.4 Schematic for Monte Carlo method [92].

3.7 Boundary Conditions

The simulation of a steady-state phenomenon in a physical system where electron transport depends upon the position in space is of particular interest for the analysis and modeling of devices. For this case, an ensemble of independent particles must be used, and averages must be taken over particles at given positions. In the case of a device, the electrons are constrained inside a box, which represents an open system through which the particles flow, and appropriate boundary conditions on the sides must be adopted. In many cases, devices present a direction of symmetry, so that one can restrict the study to a representative slice of the device, as shown in Fig. 3.5. Two sides of the box will therefore be in common with the adjacent parts of the device. When a particle crosses one of these boundaries, to conserve charge we can re-inject another particle with the same momentum components through the other side (periodic boundary). The remaining sides of the box are considered to act like a mirror, which inverts the normal component of the momentum when an electron impinges on it. Where contacts are defined, the electrons are instead absorbed and another electron is re-injected from the same or another appropriate contact. The momentum components for re-injected electrons may be conveniently selected at random from a cold Hemi-Maxwellian distribution, that is, one with only positive velocity components along the direction perpendicular to the contact.

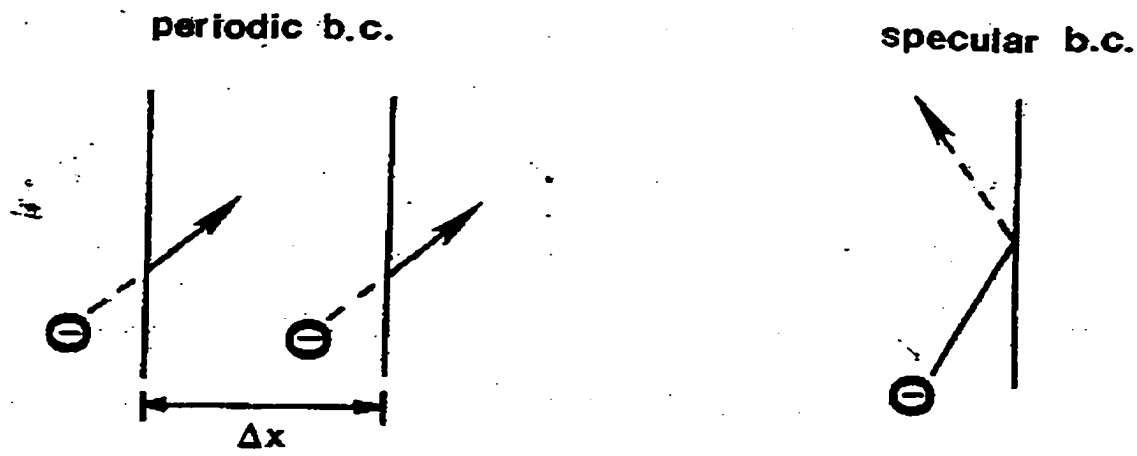

Fig. 3.5 Section of a device and appropriate boundary condition for the electrons in a device EMC simulation. [73]

The spatial distribution of the charge and of the ionized doping atoms is not homogeneous inside the simulated device, therefore the electric field is a function of position and must be obtained from the solution of Poissons's equation. Provided the number of simulated particles is sufficiently large, the average value obtained on the sample ensemble as a function of time will be representative of the average for the entire gas. The ensemble average of a quantity A(t) must be estimated according to the basic definition

$$< A(t) >= \frac{1}{N}\sum_{i=1}^{N} A_i(t). \qquad (3.28)$$

The transient dynamic response obtained by means of the simulation will depend upon the initial condition of the carriers assumed.

CHAPTER 4

SIMULATION RESULTS AND DISCUSSION

4.1 Introduction

A number of issues somewhat unique to the GaN based heterostructure system arise and can be expected to have important bearing on the transport behavior. The first issue is related to the large polarization. For instance, polarization related modifications to the internal fields could affect ionization rates in quantum well devices [93] or alter electronic injection at the gate contacts of HFETs [94]. Furthermore, carrier mobility should also be affected by the polarization-induced field enhancements since carrier wave functions and the scattering rates are directly modified in the process. In addition, interface roughness scattering is expected to increase due to the closer proximity of the 2DEG with the barrier layer at the higher electric fields. The interface roughness scattering is typically quantified on the basis of weak-perturbation theory in terms of two parameters: the root-mean-square value of fluctuations at the interface Δ, and the correlation length L between fluctuations. These parameter values are not well known for AlGaN/GaN HFETs and need to be determined. It is also unclear whether weak perturbation theory would be adequate for accurately predicting the transport behavior. Screening effects arising from the higher electron density also need to be considered in evaluating the transport properties. These could exhibit spatial inhomogeneity across the interface. Next, the degeneracy effects associated with the higher electron density need to be carefully evaluated because of the high 2DEG density. There have been no studies into the role and extent of Pauli exclusion on the mobility in GaN HFETs to the best of our

knowledge. A third point relates to the impact of material parameters and geometry on the electrical response. For example, changes in the mole fraction of the AlGaN barrier layer, the spacer thickness, or the barrier width all alter the polarization field, the carrier density, and thus the electrical response characteristics. It is important to obtain quantitative predictions in order to optimize the device operating characteristics. Finally, numerical evaluations of the drift velocity as a function of the applied agate voltage and longitudinal field need to be carried out to ascertain the nonlinearity in response and the high temperature behavior. Changes in the interface field with gate bias, for example, are expected to produce nonlinear variations in drift velocity. Such nonlinearity can lead to possible harmonic generation, intermodulation and mixing of time-dependent signals applied to the gate of HFET structures.

In this dissertation work, Monte Carlo based calculations of the large-signal nonlinear response characteristics of GaN-AlGaN HEMTs, with particular emphasis on intermodulation distortion (IMD), have been performed. The nonlinear electrical transport is treated on first principles, all scattering mechanisms included, and both memory and distributed effects built into the model. The results demonstrate an optimal operating point for low intermodulation distortion (IMD) at reasonably large output power due to a minimum in the IMD curve. Dependence of the nonlinear characteristics on the barrier mole fraction "x" is also demonstrated and analyzed. Finally, high-temperature predictions of the IMD have been made by carrying out the simulations at 600 K. An increase in dynamic range with temperature is predicted, due to a relative suppression of interface roughness scattering.

In this chapter, we examine all of these effects though numerical Monte Carlo based simulations of electron transport. Electronic mobility and drift velocity have been carried out for bulk GaN and AlGaN-GaN heterojunctions. The bulk calculations were intended to serve as a validity check of the simulation model. For the heterojunction electron mobility calculations, polarization effects, degeneracy and interface roughness scattering were all taken into account. This chapter presents all of the results obtained from the numerical simulations.

4.2 Bulk Monte Carlo Calculations

The simulation scheme for bulk wurtzite GaN is discussed first. A three-valley, nonparabolic conduction band model was used for the transport calculations in bulk GaN. For wurtzite-phase GaN, the minimum is located at the Γ point. The satellite valleys are at the *U*-point, that is, two-thirds of the way between the *L*- and *M*- symmetry points. The next highest valley is located at the Γ_3-point. Thus, two Γ–valleys and the six equivalent *U*-valleys were considered. The scattering mechanisms considered were ionized impurity based on the Brooks-Herring approach, acoustic deformation potential scattering, polar-optical interactions and intervalley deformation potential processes. The piezoelectric scattering was excluded, since it has been shown to be negligible at temperatures of 300 K and beyond. Nonequivalent intervalley scattering events were taken into account amongst all three valley types, governed by a single deformation potential and phonon energy. A 65-meV phonon was assumed to adequately represent both nonequivalent and equivalent intervalley scattering. A 92-meV phonon value was used for the intravalley longitudinal polar optical phonon scattering. Screening was

incorporated with the random phase approximation in the long wavelength limit. The value of the inverse screening length β was obtained as,

$$\beta = [ne^2 / \varepsilon k_B T_e(t)]^{0.5}, \tag{4.1}$$

where n is the electron density, e the electronic charge, k_B the Boltzmann constant, and T_e the effective electron temperature. This effective temperature was evaluated at each step of the Monte Carlo simulation with the following equation [26],

$$T_e(t) = \frac{2}{3k_B} \sum_I f_I (0.5 m_I < v^2 >_I - 0.5 m_I v_{dI}^2). \tag{4.2}$$

In the above equation, f_I, m_I, $<v^2>_I$ and v^2_{dI} refer to the electron fraction, effective mass, mean-square velocity, and drift velocity, respectively, for the I^{th} band and the index I runs over the three bands. The T_e represents an ad-hoc parameter as used by Bhapkar and Shur [26], and is not a real electron temperature. Pauli exclusion was applied based on a rejection technique implementation first proposed by Lugli and Ferry [94]. The material parameters required for the bulk GaN simulations were generally taken from the published literature [27,48], with minor adjustments.

Results of the Monte Carlo simulation for bulk wurtzite GaN at 300 K are given and discussed first. Some of the transport parameters for GaN material have not explicitly been measured. Hence, as a first step, the 10,000-electron Monte Carlo code was used without any quantization effects to simulate the transport in bulk material. The primary objective was to start with as many of the known parameters for wurtzite GaN as possible and fine tune other values to achieve a reasonable fit with available reports in the literature. The best-fit parameters thus obtained are given in Table 2.1 and were

subsequently used for the inversion layer problem. These parameters are used in the Monte Carlo calculations for wurtzite GaN.

Fig. 4.1 shows the transient drift velocity of the electronic ensemble in bulk GaN for different values of the electric field parameter. An upperbound of 400 kV/cm was chosen to prevent the electronic energies from becoming excessively large. This precaution was necessary, since the present simulation does not include a full bandstructure calculation, but instead relies on a simple nonparabolic approach to the

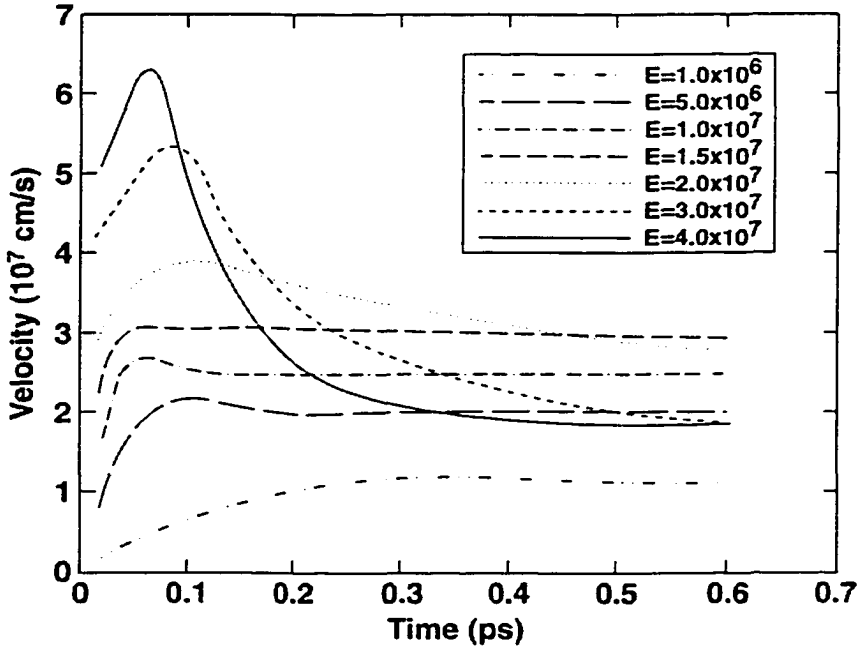

Fig. 4.1 Monte Carlo results of the transient electron drift velocity at 300 K in wurtzite GaN for different fields

energy bands. A velocity overshoot arising from intervalley transfer is immediately seen from the curves, similar to the occurrence for GaAs. The threshold field for this

transferred electron effect is predicted to be around 170 kV/cm. For electric fields higher than this threshold, there is a monotonic decrease in the steady-state drift velocity, although a much higher transient overshoot results. At 400 kV/cm, for example, a peak velocity of about 6.5 x 10^7 cm/s is predicted. The central conclusion is that GaN material can be well utilized for nonequilibrium transport and would yield a fast response for scaled-down structures.

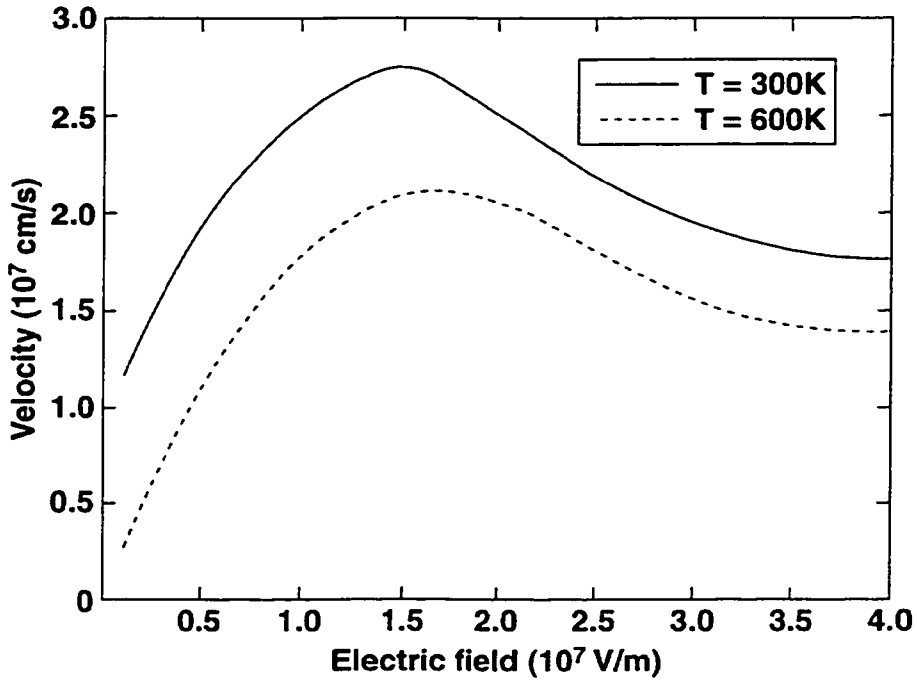

Fig. 4.2 Monte Carlo results of the electron velocity-field characteristics at 300 and 600K for bulk GaN.

Steady-state values at the high fields are also larger than those obtainable for GaAs. The field-dependent velocity-field curves for the material at two different temperatures are shown in Fig. 4.2. A fairly large drift velocity of 1.4 x 10^7 cm/s at 400

kV/cm is predicted for temperatures as high as 600 K, while the room temperature peak is nearly 2.6 x 10^7 cm/s, which translates into a 30-percent increase over that for GaAs.

These results also indicate that high-field drift velocities for the wurzite phase are larger than those reported for zinc blende GaN. Although experimental reports of the low-field mobility demonstrate higher values for zinc blende due to a smaller Γ–valley effective mass, the wurtzite phase would have an advantage for high field applications. This is because the satellite valley for the wurtzite phase is higher, at around 1.95 eV versus the 1.45 eV inter-valley energy separation for zinc blende. These conclusions are similar to those reached previously by Kolník et al [95].

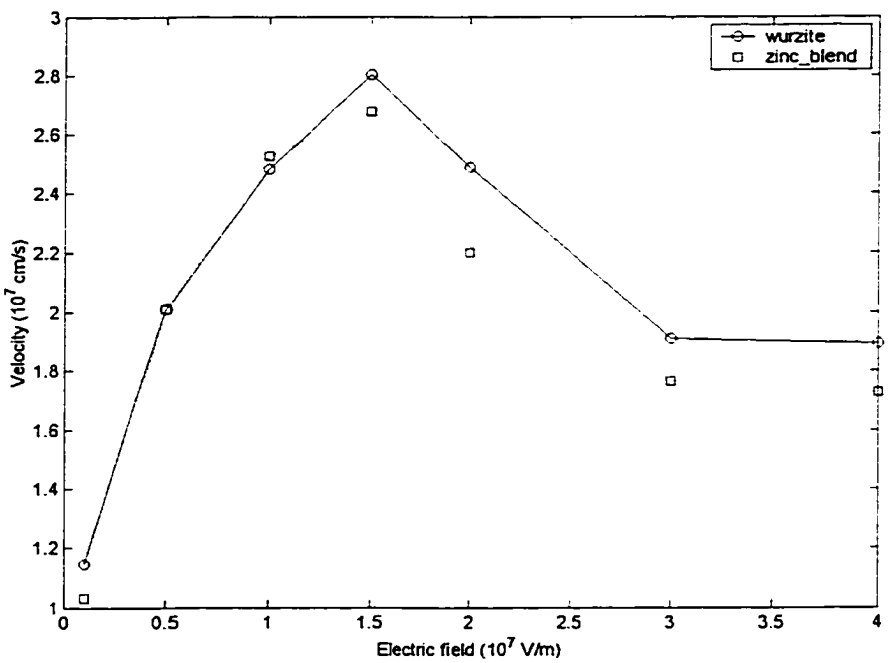

Fig. 4.3 Comparison of zinc-blende and wurtzite at 300k for bulk GaN.

Finally, the Monte Carlo results for the lowest Γ-valley occupancy as a function of time are shown in Fig. 4.4 for various electric fields. Fractional occupancies of 90 percent and higher are predicted for applied electric fields below 150 kV/cm. There is a relatively sharp transition into the satellite valleys for fields around 180 kV/cm. Steady-state occupancies as low as 35 percent are predicted at our highest field, 400 kV/cm. These results are also fairly close to those obtained by Kolnik et al. [95], on the basis of a more sophisticated Monte Carlo scheme that included a full bandstructure. This agreement establishes the validity of the transport parameters used in the present model and underscores its utility as a simple, computational efficient tool for analyzing transport for field below 400 kV/cm.

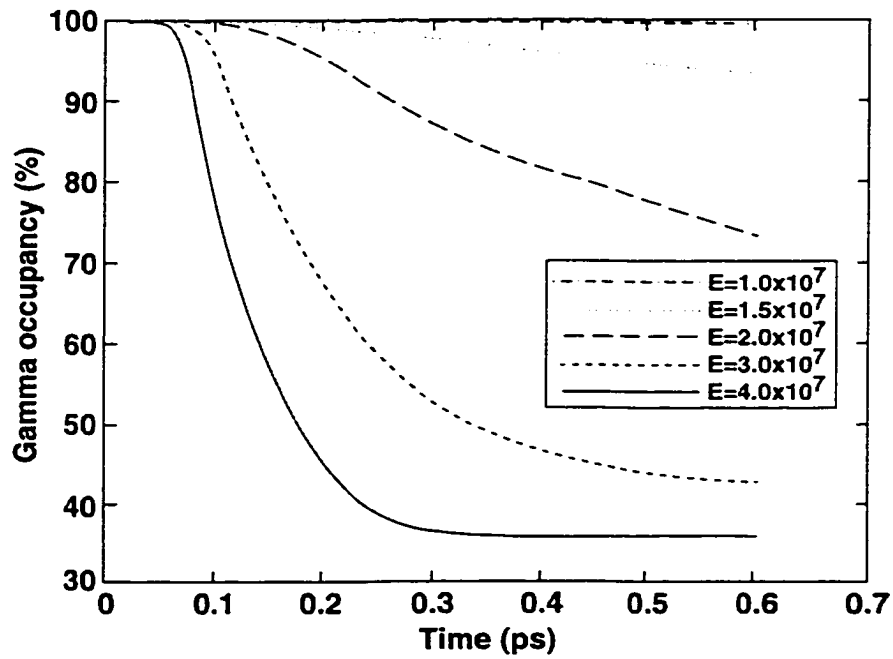

Fig. 4.4 Monte Carlo predictions of the time-dependent Γ-valley occupancies at different fields.

4.3 Monte Carlo Calculations for the GaN/AlGaN System

Simulations of parallel transport for the 2DEG in GaN-AlGaN HFET structures were also carried out based on the kinetic Monte Carlo approach. As is well known, mobile carriers are confined within a shallow inversion layer at the interface. Confinement then leads to the following consequences:

(a) Electron quantization with subband formation, leading to a two-dimensional flow;

(b) Changes in the transverse wavefunctions that slightly lower the electron-phonon scattering rates, but increase the number of inter- and intra-subband processes;

(c) A relative decrease in the influence of remote ion, oxide charge and depletion dopant ion scattering due to the increased physical separation;

(d) The inclusion of an additional interface roughness scattering, which imparts a strong transverse electric field dependence on the channel mobility, as first shown by Sabnis and Clemens [96] for silicon.

Physically, higher transverse fields enhance the electronic confinement by drawing them closer to the interface, which leads to greater interface roughness scattering and lower mobility. The details, however, are complicated, since the relative subband occupancy and spatial electron distribution within each subband change with the transverse field by different amounts. Furthermore, as channel densities are enhanced with transverse field, free-carrier screening increases and should work to lower the effects of polar and Coulombic interactions, thereby moderating the mobility reductions.

For simplicity, it has been assumed here that the electron density within the conduction channel is uniform. Extensions to account for possible nonuniformities can be incorporated by using the procedure outlined by Ravaioli and Ferry [97]. Details of

our inversion-layer Monte Carlo implementation and the procedure can be found in reference [45]. Electron confinement was treated on the basis of a simple triangular well approximation [40,98]. In keeping with the recent experimental work on GaN heterostructures, the *c*-axis was taken to be perpendicular to the GaN-AlGaN interface (and hence, parallel to the growth direction), resulting in a single transverse effective mass and one set of subbands. Fang and Howard [99] variational wavefunctions were used for computations of the scattering rates. Although more sophisticated wavefunctions derived from a solution of the Poisson and Schrodinger equations could have been used, the present approach was chosen, given the existing uncertainty in the material parameters and the need to implement a relatively fast computational scheme. Besides, the variational method is known to yield reasonably accurate results and to exhibit the correct trends.

A two-subband Monte Carlo model was used which included electron interactions with acoustic modes via the deformation potential, polar optical phonon interactions, zero- and first-order intervalley deformation potential scattering [100], interface roughness [101] and interface ion interactions [40]. Higher subbands were ignored in the present context of low fields, as were considerations of interface phonon modes. Similarly, real-space transfer and electron flow in the AlGaN barrier layer was also neglected. However, the role of AlGaN on the transport was indirectly taken into account by including an alloy disorder scattering mechanism. The rationale is similar to that used by Hsu and Walukiewicz [59]. Screening of the polar optical and interface ion interactions was evaluated within the random phase, zero-frequency approximation [81] that requires the evaluation of a wavevector-dependent form factor. Finally, both intra-

and interband transitions were accounted for in the numerical transport simulations. Treatment of the interface roughness scattering was based on a simple Gaussian model for the autocovariance function [40], rather than the exponential dependence used by Goodnick et al. for silicon [41]. More complicated treatments of discrete AlGaN islands at the interface have been suggested to include localization effects [102] but were not used here for computational simplicity. The interface roughness scattering is most simply treated in the Born approximation by assumption that the roughness can be regarded as a weak perturbation. This is then characterized in terms of two parameters, namely, the correlation length L and root-mean-square (rms) height Δ of the roughness fluctuations. This model has previously been shown to be adequate, yielding L and Δ values of about 2.2 nm and 0.2 nm for silicon [44] and 2.3 nm and 0.8 nm for SiC [45]. The corresponding parameters for the GaN-AlGaN system, however, are not known, and have been obtained here through a best-fit procedure. Finally, degeneracy is expected to play a role in the GaN 2D system, because of the large carrier densities that have been observed experimentally. This effect, which essentially reduces the scattering rate due to a finite occupancy probability of the final state, was taken into consideration. As our results show that the mobility values can increase substantially at high gate voltage levels due to this effect.

Simulations were next carried out at 300 K for the GaN-AlGaN HFET structure. The polarization effect is known to be dominant in this material system and should influence both the carrier sheet density and interface electric field. Since the carrier density controls the device current and mitigates scattering through enhanced screening, it is critical to correctly predict the mobile charge density as a function of the geometry

and operating conditions. The interface field is also an important transport parameter, since it shapes the electronic wavefunctions, thereby influencing the interface scattering process. Consequently, the sheet density and interface fields were calculated as a function of the gate bias. The AlGaN mole fraction and thickness were the variable parameters. The results are shown in Figs. 4.5 and 4.6 for an undoped system.

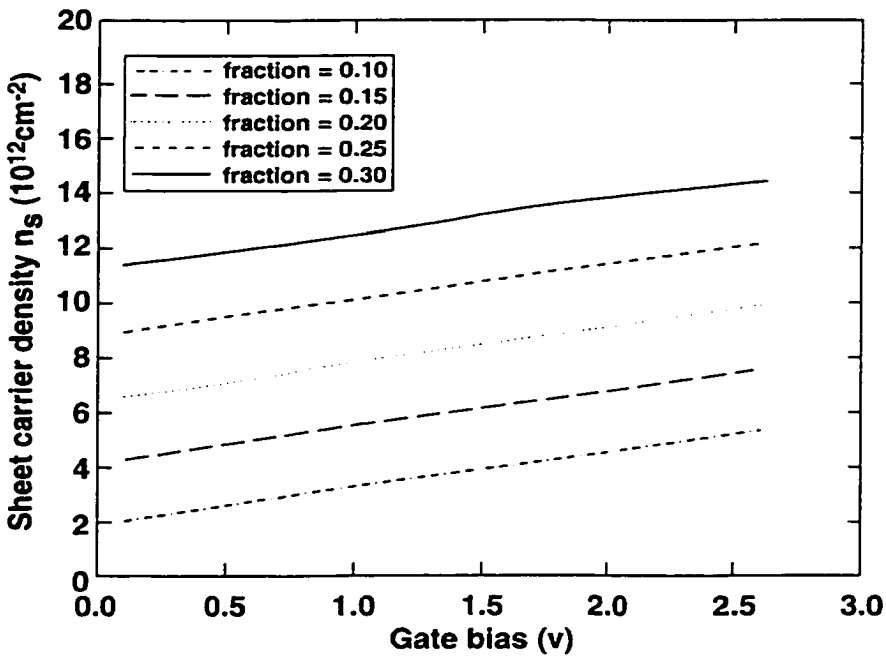

Fig. 4.5 Gate voltage dependence of the electron density for various AlGaN mole fractions. The thickness was 30 nm.

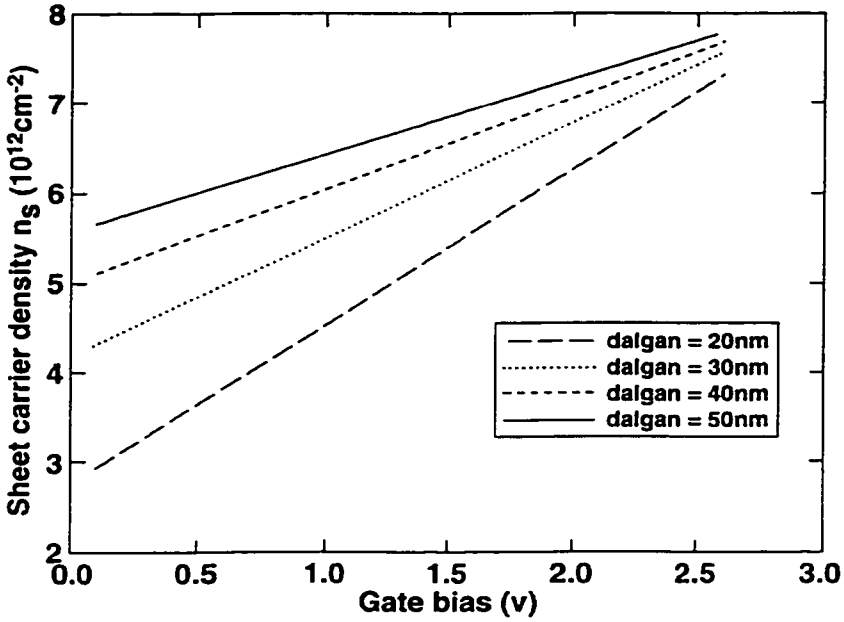

Fig. 4.6 Gate voltage dependence of electron density for various $Al_{0.15}Ga_{0.85}N$ layer thicknesses.

From both figures, it is evident that the 2D electron density n_s is large and almost an order of magnitude higher in comparison to values reported in the literature for the GaAs heterosystems. Our values match the recent experimental reports for the AlGaN-GaN HFET [51]. Fig. 4.5, for 30-nm barriers, shows that as the AlGaN mole fraction is increased, the sheet density (and hence also the interface field) is enhanced. This is due to the increased values in both spontaneous and piezoelectric polarization terms. Increases in the band offset with mole fraction also contribute to a higher n_s value, as inferred from Fig. 4.5. Also as expected, the density increases with bias.

The four curves of Fig. 4.6 show the effect of variations in the AlGaN barrier thickness on the bias-dependent sheet density. The Al mole fraction was kept fixed at 0.15. The largest barrier thickness provides the most mobile carriers in the channel.

Obviously there would be a practical limit on barrier thickness increase for purposes of enhancing the channel density. With a very thick AlGaN layer, the device would no longer be pseudomorphic and would have internal dislocations and defects.

Next, the electron channel mobility was calculated based on the Monte Carlo model. Currently there are no measured data available on the interface roughness characteristics, to the best of our knowledge. In the absence of such data, the interface roughness correlation length L and the rms height of interface roughness fluctuations Δ were taken as adjustable parameters. It was implicitly assumed that the interface roughness process could be adequately modeled in the Born approximation with the use of weak-perturbation theory and that localization effects were negligible. Furthermore, the presence of any spatially distributed interface polarization charge arising from the creation of AlGaN and GaN islands at the heteroboundary were presumed to be adequately included by the L and Δ parameters. Since the mobility has to be computed at zero (or very low) electric fields, this parameter was evaluated based on the diffusion coefficient D. Use of a drift velocity calculation at low fields for determining the mobility can lead to large statistical variations, due to the low driving field. The diffusion constant was computed from the time derivative of the second central moment as,

$$D = 0.5 \frac{d[< (x_i(t) - < (x_i(t) >)^2 >]}{dt}. \qquad (4.3)$$

The above applies to nondegenerate situations strictly. For a more precise calculation of D with degeneracy, a modified Monte Carlo technique as suggested by Thobel et al. needs to be used [103]. However, this aspect was ignored here, and instead equation 4.3 was used for calculations of D. An approach similar to the present one was taken by

Yamada et al. in the recent past [104]. The low-field mobility is related to D via the Einstein relation [75] as,

$$D = \frac{nu}{q}[\frac{dn}{dE_F}]^{-1}, \tag{4.4}$$

where q is the electronic charge, n the carrier density and E_F the Fermi energy. For a two-subband electron system considered here, the density n is related to the Fermi level as,

$$n = [\frac{m^* k_B T}{\pi\hbar^2}]\ln\{(1+\exp[\frac{(E_F - E_1)}{k_B T}])\} \times \{1+\exp[\frac{(E_F - E_2)}{k_B T}]\}, \tag{4.5}$$

where m^* is the effective electron mass, while E_1 and E_2 are the subband energies. With the use of Eq. 4.4 in the Einstein equation, the mobility can be determined from knowledge of the diffusion constant D. Figure 4.7 shows the time-dependent variation of the $P(t)$ term for various values of L and Δ with applied gate bias values of 0.0 and 3.0 V. A 30-nm $Al_{0.15}Ga_{0.85}N$ layer was used. Values 1.5 nm and 2 nm for L, with Δ = 1 and 0.75 nm, have been shown. These parameters were adjusted until a good match of the electron mobility with available experimental data was obtained. The best mobility fit was obtained for L = 1.5 nm and Δ = 0.65 nm, and the complete set of resulting transport parameters used for the simulation are given in Table 2.1.

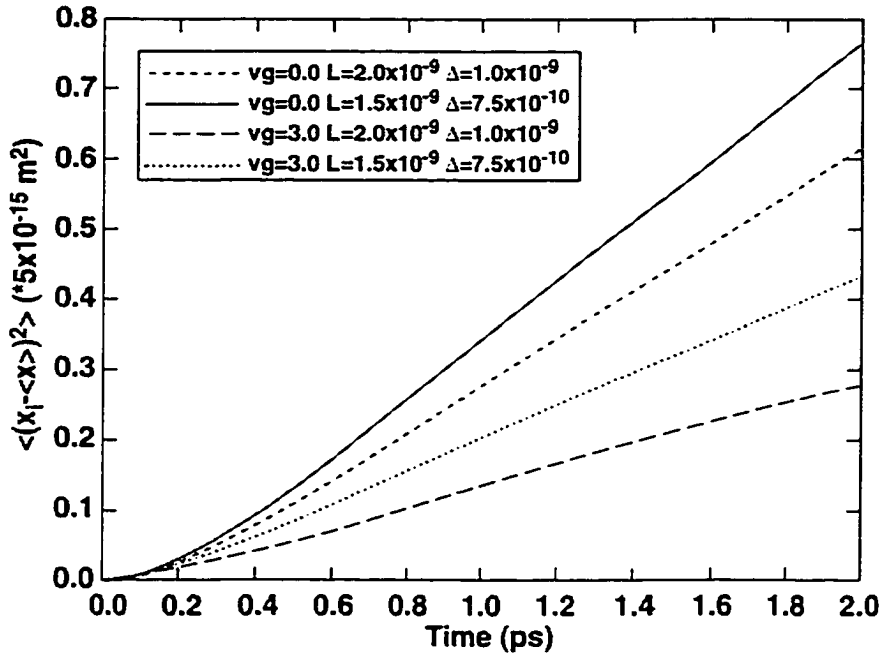

Fig. 4.7 Time dependence of the second central moment obtained from Monte Carlo calculations.

The mobility results at 300 K as a function of gate bias are shown in Fig. 4.8, along with experimental data taken from the literature [105-108]. The measured values do have a significant spread. The role of degeneracy is clearly brought out in Fig. 4.8. Without degeneracy, the mobility is predicted to be much lower, since the possibility of final state occupancy is then discounted. The predicted values agree with the available experimental data, but only when the Pauli exclusion is taken into account. It may be mentioned that the experiments measured Hall mobility, while here the low-field drift mobility has been obtained. The two differ by the Hall factor. The Hall factor can be quite complicated, since it depends on the details of the prevalent scattering mechanisms, their relative strengths and the bandstructure of the mobile carriers. Typically, the Hall

factor has a value higher than unity. In some cases, however, such as holes in strained Si or $Si_{1-x}Ge_x$ alloys, this factor can be below unity [109]. This is due to the strong nonparabolicity and band warping effects. For electron in GaN, however, such a peculiar situation does not arise. Hence, the Hall factor is, in general, larger than 1. Consequently, the drift mobility is expected to be lower than the Hall mobility. This aspect was indirectly taken into account here, and the fitting parameters were chosen to yield drift mobility predictions that were somewhat lower than the experimental values.

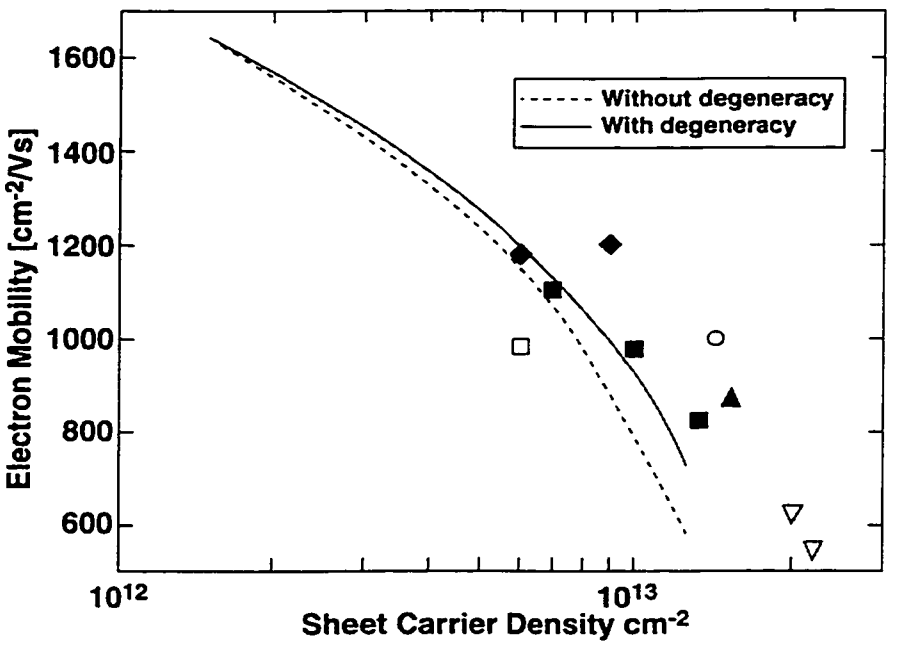

Fig. 4.8 Monte Carlo results of the gate bias dependent GaN HFET electron mobility with and without degeneracy [105-108].

Next, the electron drift velocity was calculated for the interface roughness parameters obtained from the fitting procedure above. The transient velocities at different values of longitudinal electric field along the channel, with the applied gate bias

V_g as a parameter, are shown in Fig. 4.9 for 300 K. As expected, the highest velocity occurs at the lowest (0 V) gate bias, due to reduced interface roughness scattering. At electric fields of 20 and 50 kV/cm, the steady-state velocities for $V_g = 0$ are predicted to be about 1.5 x 10^7 and 2.1 x 10^7 cm/s, respectively. At the 3 V gate bias, the corresponding values for the 20 and 50 kV/cm fields are 1.15 x 10^7 and 1.8 x 10^7 cm/s.

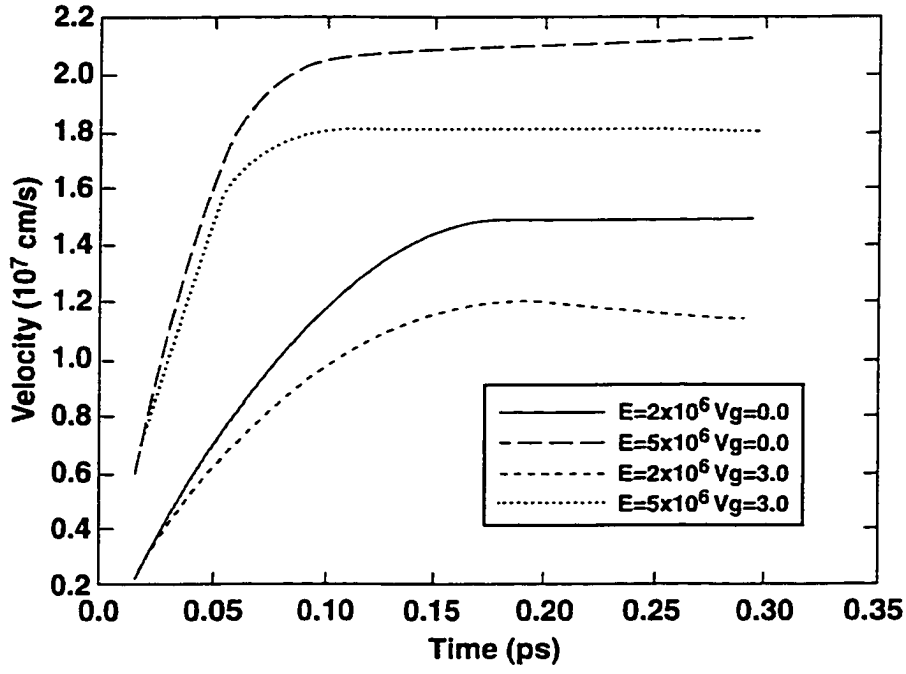

Fig. 4.9 Transient 2D electron drift velocities as a function of the gate bias and longitudinal electric field at 300K.

The steady-state results gleaned from the transient Monte Carlo simulations are shown in Fig. 4.10 for four values of the gate bias. In addition, steady-state velocity-field curves for the 2DEG at 600 K are also shown.

The velocity decreases with the gate bias for every longitudinal field value, but the scaling is not linear. This is expected since changes in V_g primarily affect interface scattering, while the other processes are only mildly changed due to variations in the wavefunction overall and screening. In any case, it becomes clear that the nonlinear dependence on gate voltage is likely to play a role in large signal amplification and cause mixing of multifrequency signals. The values for 600 K are lower than at 300 K, but the nonlinearity with V_g appears to be somewhat mitigated. This is to be expected, since the phonon processes become more dominant at the higher temperatures and reduce the relative role of interface roughness scattering (IRS).

Since the IRS rate is strongly energy dependent and decreases sharply with increasing energy, the gate voltage effects should be most prominent under conditions of low carrier energies, such as with low longitudinal electric fields. This is borne out in Fig. 4.10. At the lowest electric field of 10^6 Vm^{-1}, the drift velocities V_{300K} and V_{600K} corresponding to temperatures of 300 and 600K, respectively, are predicted to be 1.044 x 10^5 and 0.4883 x 10^5 ms^{-1} for $V_g = 0$. However, at $V_g = 4.5$ Volts, the velocities V_{300K} and V_{600K} are computed to be 0.59 x 10^5 and 0.3018 x 10^5 ms^{-1}, respectively. The ratio $(V_{600K}/V_{300K})\,|_{vg=0}$ then turns out to be less than $(V_{600K}/V_{300K})\,|_{vg=4.5}$. This in inequality $(V_{600K}/V_{300K})\,|_{vg=0} < (V_{600K}/V_{300K})\,|_{vg=4.5}$ is the direct consequence of a disproportionately large reduction of the low-field 300 K velocity in going from the $V_g = 0$ operating condition to $V_g = 4.5$ Volts. As a final comment in this regard, quantitative evaluations of the temperature-dependent HFET response to multicomponent, time-dependent signals would be more useful in yielding details of harmonic distortion and remain to be carried out.

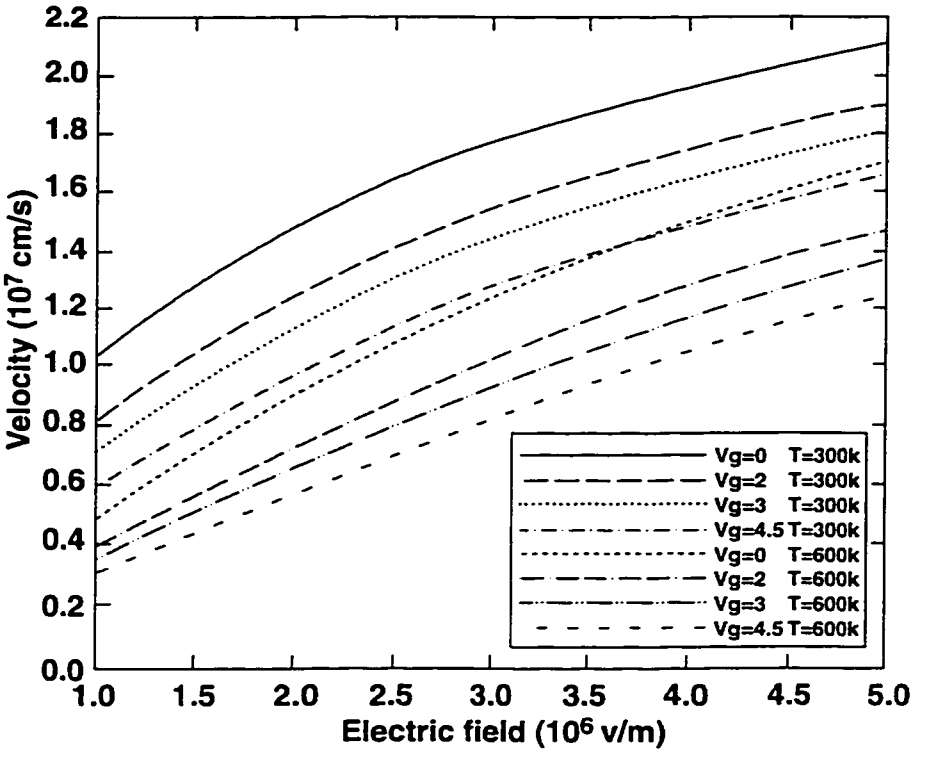

Fig. 4.10 Steady state velocity field characteristics for 2D electrons for various gate-voltage. Temperatures of 300 and 600K are used.

4.4 IMD Characterization of GaN HEMTs

4.4.1 IMD in GaN

Monte Carlo based calculations of the large-signal nonlinear response characteristics of GaN-AlGaN HEMTs with particular emphasis on intermodulation distortion (IMD) were also performed. The nonlinear electrical transport was treated on a first-principles basis, all scattering mechanisms included, and both memory and distributed effects were built into the model. The results demonstrate an optimal

operating point for low intermodulation distortion (IMD) at reasonably large output power due to a minima in the IMD curve. Dependence of the nonlinear characteristics on the barrier mole fraction "x" is also demonstrated and analyzed. Finally, high-temperature predictions of the IMD have been made by carrying out the simulations at 600 K. An increase in dynamic range with temperature is predicted, due to a relative suppression of interface roughness scattering. The thermal conductivity of GaN is higher than GaAs, which should help alleviate the thermal management issue. The use of SiC substrates for GaN HEMT fabrication [110,111] is also helpful in this regard. These collectively enhance the prospects of GaN HEMTs for use in microwave power amplification, particularly at the *X*-band and higher frequencies [29,112].

One of the most important requirements for microwave power amplifiers is the level of nonlinear distortion and inter-modulation (IM) behavior. Nonlinearity in the output current response with applied gate voltage results from the combined nonlinear behaviors of carrier drift velocity and the channel density. The drift velocity is determined by a variety of energy dependent scattering processes with the net magnitude being a weighted average over the entire carrier distribution within the channel. The scattering rates are nonlinear functions of energy and depend on details of the carrier wavefunctions which are shaped by the gate voltage. For example, interface roughness scattering can exhibit a nonlinear increase with transverse electric field created by the gate bias [46] due to closer proximity of the two-dimensional electron gas (2DEG) with the barrier layer. The gate voltage (V_G) also causes variations in the 2DEG density, and thus affects scattering through changes in screening of the polar interactions and degeneracy effects [46]. The carrier density variations are non-linear and depend on the

mole fraction "x," and thickness of the barrier layer [51]. Since GaN exhibits large piezoelectric effects under stress along the *c*-direction, modifications in the 2DEG is somewhat more complicated for this material system. Reports of strained zincblende GaN grown along the (111) orientation [51], or in pseudomorphic wurtzite material grown in the (0001) orientation [113], are typical examples of this situation.

The third-order intermodulation and the fundamental output power have been obtained through Monte Carlo evaluations of the time dependent current response to a two-tone, large-signal, ac gate voltage in the GHz range. Carrier trapping has been ignored due to the relatively short time scales. Hence, features such as trap related drain current compression that have recently been reported [114] will not be probed here. The results demonstrate an optimal operating point at a reasonably large output power due to a minimum in the IMD curve. Furthermore, dependence of the nonlinear characteristics on the barrier mole fraction "x" has been analyzed. Based on the Monte Carlo results, a useful analytical characterization of the nonlinear response has also been obtained. Finally, high-temperature predictions of the nonlinear behavior and IMD have been made, by carrying out the simulations at 600 K. Since the wide bandgap GaN system is a potential candidate for high-temperature operation, it is important to ascertain the IMD implications at elevated temperatures.

4.4.2 IMD Analysis

Mathematical evaluation of the nonlinear characteristics of field effect transistors (FETs) has often been based on the Volterra-Wiener formalism [116,117]. However, this technique is only applicable to small-signal inputs, and it neglects memory-effects. A

more appropriate scheme for an analytical solution would be a polynomial representation of the device output current (or current density J_0) as a function of the input gate voltage V_G [117,118], Thus,

$$J_0(V_G) = K_0 + K_1 V_G^1 + K_2 V_G^2 + K_3 V_G^3 + \cdots + \cdots, \tag{4.6}$$

where the coefficients K_i being some constants. For accurate and realistic results, the coefficient can either be extracted from actual experimental data, or from curve-fitting to Monte Carlo predictions of the current response. For a single sinusoidal input, i.e.,

$$V_G(t) = A\cos(Tt), \tag{4.7}$$

the polynomial representation yields the following current density function to fifth order :

$$\begin{aligned} J_0(A,t) = & \frac{1}{2}K_2A^2 + \frac{3}{8}K_4A^4 + \{K_1A + \frac{3}{4}K_3A^3 + \frac{5}{8}K_5A^5\}\cos(Tt) \\ & + \{\frac{1}{2}K_2A^2 + \frac{1}{2}K_4A^4\}\cos(2Tt) + \{\frac{1}{4}K_3A^3 + \frac{5}{16}K_5A^5)\cos(3Tt) \\ & + \{\frac{1}{8}K_4A^4\}\cos(4Tt) + \{\frac{1}{16}K_5A^5\}\cos(5Tt) \end{aligned} \tag{4.8}$$

For a two-tone input gate signal, i.e.,

$$V_G(t) = A\cos(T_1t) + A\cos(T_2t) \tag{4.9}$$

The current density terms at the fundamental and intermediate frequencies based on a fifth order polynomial are:

$$\begin{aligned} J_0(t) = & \{K_1 + \frac{9}{4}K_3A^3 + \frac{25}{4}K_5A^5\}[\cos(T_1t) + \cos(T_2t)] \\ & + \{\frac{3}{4}K_3A^3 + \frac{25}{8}K_5A^5\}[\cos\{(2T_1 - T_2)t\} + \cos\{(2T_2 - T_1)t\}, \\ & + \cdots + \cdots \end{aligned} \tag{4.10}$$

The choice to fifth order is meant to represent an acceptable tradeoff between increasing accuracy with the inclusion of higher orders at the expense of enhanced computational complexity. Based on the above, expressions for the input power (P_i), the output power (P_o), in dBm units, at the fundamental frequency can be obtained. These are

$$P_i = 10\log_{10}[10^3 \frac{A^2}{2R_i}] \propto 30 + 10\log_{10}[A^2], \tag{4.11}$$

and

$$\begin{aligned} P_0 &= 10\log_{10}[\{K_1 A + \frac{3}{4}K_3 A^3 + \frac{5}{8}K_5 A^5\}^2 \times \frac{10^3}{2R_0}] \\ &\propto 30 + 10\log_{10}[\{K_1 A + \frac{3}{4}K_3 A^3 + \frac{5}{8}K_5 A^5\}^2] \end{aligned}, \tag{4.12}$$

where R_i and R_o are the respective input and output resistances. Similarly, the variation of the third-order intermodulation power P_{IP} , in dBm, with the gate signal amplitude "A" is :

$$P_{IP} \propto 30 + 10\log_{10}[\{\frac{3}{4}K_3 A^3 + \frac{25}{8}K_5 A^5\}^2], \tag{4.13}$$

Based on Eq. 4.8~4.10, the input-output power curves can be obtained, provided the coefficients K_i are given or can be extracted.

The above approach, though reasonable, excludes memory effects within the system. It is implicit that the output changes instantaneously in response to the fluctuations of the input signal. A more realistic representation is provided through Monte Carlo simulations that can yield an output current due to a collective motion of the 2DEG ensemble in response to gate voltage variations. The history of individual particles in automatically included, as are all details of scattering that control the dynamic evolution of the carriers. The non-Markovian behavior is expected to become important

for short devices and/or high operating frequencies. Here, both the analytical results and the Monte Carlo calculations have been used to probe the IMD behavior.

4.4.3 Results without Real Space Transfer (RST)

The polarization effect is known to be dominant in the GaN-AlGaN material system, and influences the carrier sheet density n_s, screening and degeneracy, the interface electric field, and the interface roughness scattering. Hence, to begin with, the carrier density was calculated as a function of the gate bias based on equations 2.4 and 2.5 with the AlGaN mole fraction "x" as the variable parameter. The results, for an undoped system with 30 nm AlGaN barriers are shown in Fig. 4.11. From the figure, the 2D electron density n_s is seen to be large and almost an order of magnitude higher in comparison to values reported in the literature for the GaAs heterosystems. Our values match the recent experimental reports for the AlGaN-GaN HFET [51].

Fig. 4.11 shows a negative gate threshold for each curve, making n_s a strongly nonlinear, monotonically increasing function of V_G. For analytical calculations, polynomial curve fits to the n_s-V_G relationships can easily be obtained for each mole fraction. Obviously if the HEMT were operated in the large-signal mode with amplitudes less than the gate threshold, then the nonlinearity (and hence, IMD) would be less severe. Fig. 4.11 also indicates that increasing the mole-fraction should improve the IMD characteristics, and permit higher signal voltages and input power due to an increased gate threshold.

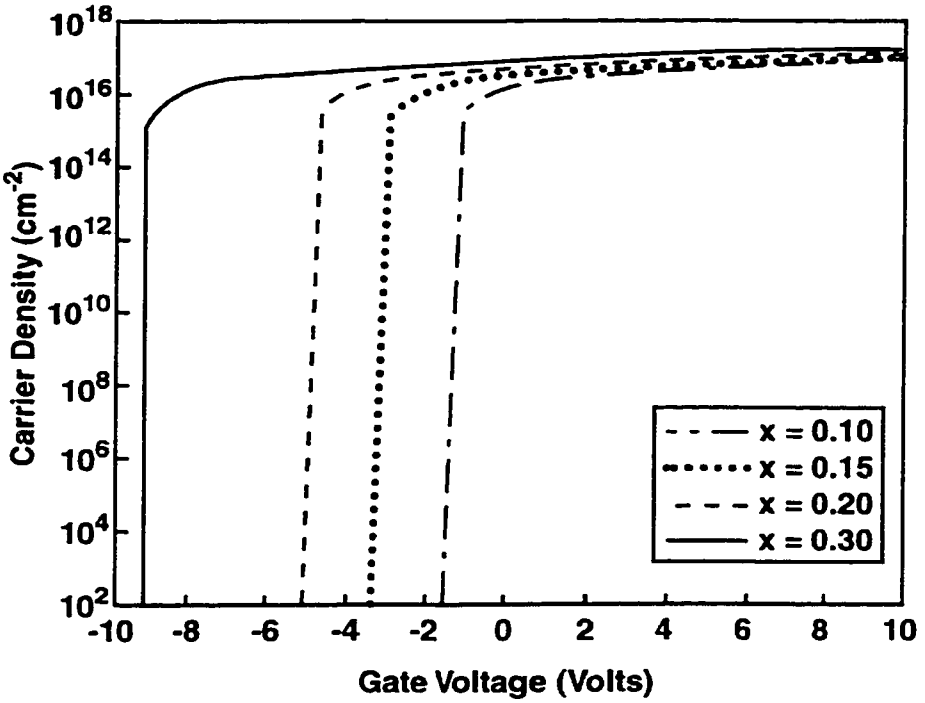

Fig. 4.11. Gate voltage dependence of the electron density for various $Al_xGa_{1-x}N$ mole fractions. The thickness was 30 nm.

The second source of nonlinearity arises from a V_G dependence of the 2DEG drift velocity. This aspect was probed by carrying out Monte Carlo simulations for a fixed drain field for various values of DC gate voltages. Results showing variations in the electron drift velocity V_{dr} with gate voltage are shown in Fig. 4.12 with the mole fraction as a parameter. The temperature was set to 300 K and a longitudinal channel field of 10 kV/cm was used. The relatively low field was chosen to avoid complications arising from real space transfer and trapping within the AlGaN layer. Such secondary effects have been reported recently at high drain currents. A general monotonic decrease of the carrier velocity with gate voltage is apparent, and arises from increases in interface roughness

scattering (IRS). Since the decreasing V_{dr} behavior is opposite to the n_s trend, these two factors mitigate the overall nonlinearity in the current. Based on the above argument, one can expect the nonlinear response trend to change at higher temperatures. This is because at higher temperatures, phonon scattering would increase, reducing the role of IRS.

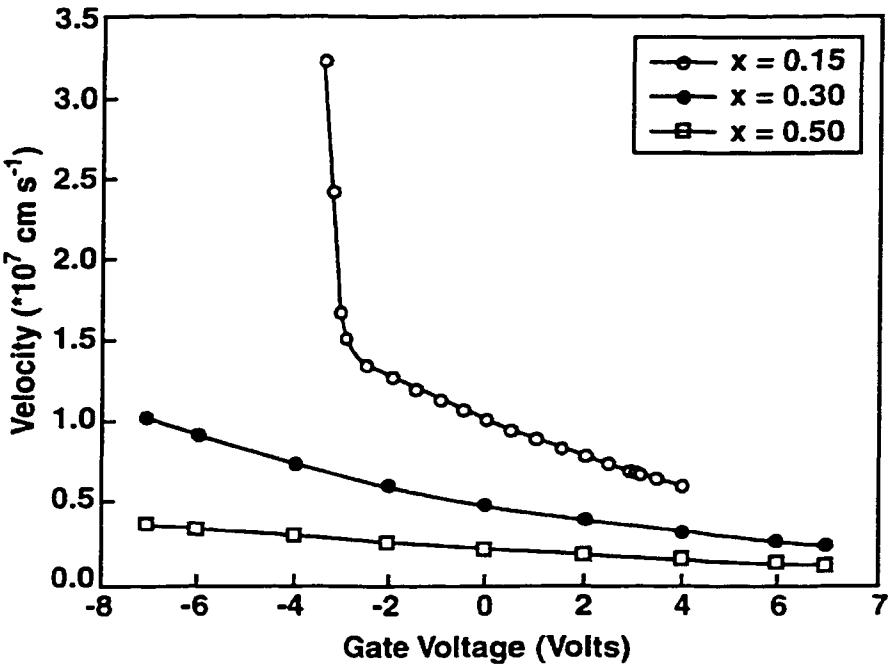

Fig. 4.12. Monte Carlo results of the electron drift velocity at 300 K as a function of the HEMT gate-voltage with the AlGaN mole fraction as a parameter.

Consequently, the decrease in V_{dr} with gate voltage would become less significant, and the n_s-V_G term would dominate. The V_G dependence of the current density was obtained by combining the results of Figs. 4.11 and 4.12 for various values of the mole fraction. The results are shown in Fig. 4.13. The x=0.15 curve is dominated by the electron density

term. It has a strongly non-linear current density with values starting near zero close to the –3.5 Volt threshold. This is followed by a significant increase. The x=0.5 curve allows for a much larger gate voltage swing and is dominated by the velocity term since carrier density does not change much over this range of V_G. Finally, the x=0.3 curve exhibits an initial increase due to the n_s term, followed by a decrease arising from the drift velocity factor.

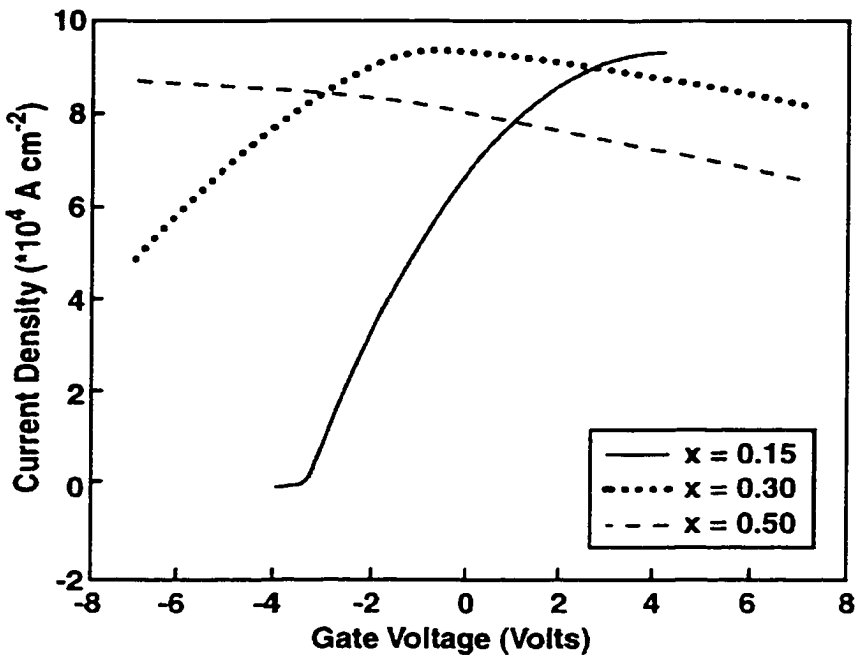

Fig. 4.13. Current density dependence on the gate voltage at 300 K for various AlGaN mole fractions.

In general, the results exhibit the following features.

(a) All curves exhibit non-linearity.

(b) The characteristics change with the mole fraction and the gate voltage swing. For example, the x=0.3 curve reveals that a large-signal gate amplitude limited to ± 2 Volts

would produce a nearly constant current response. For these conditions then, output power at the fundamental frequency can be expected to be relatively low.

(c) The results of Fig. 4.13 suggest the possibility of judiciously selecting conditions for minimal non-linear distortions.

The input-output power characteristics, as obtained from equations (4.9)-(4.11), are shown in Fig. 4.14. Polynomial fits to the voltage dependent current densities of Fig. 4.13 were used to generate the power characteristics for x=0.15, 0.30 and 0.50. Values of P_{in} on the x-axis were calculated as:

$$P_{in} = 10\log_{10}(10^3 \times A^2)\ dBm, \tag{4.14}$$

with A being the gate voltage amplitude. Similarly, values of P_o were obtained as:

$$P_o = 10\log_{10}(10^3 \times J^2)\ dBm, \tag{4.15}$$

from the computed drain current density J.

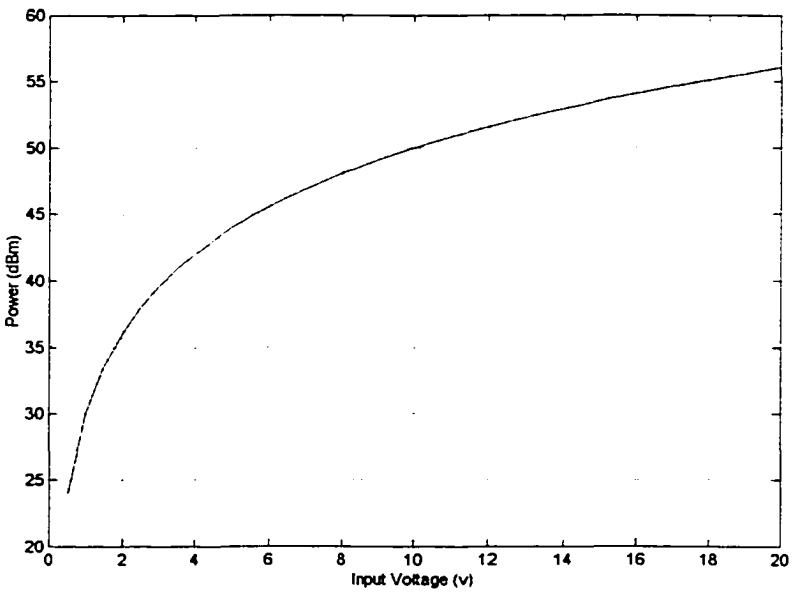

Fig. 4.14. Relationship between input voltage and output power.

Based on equation 4.14, the numerical relationship between input voltage and output power is shown in Fig. 4.14. It will be used for future reference and discussions.

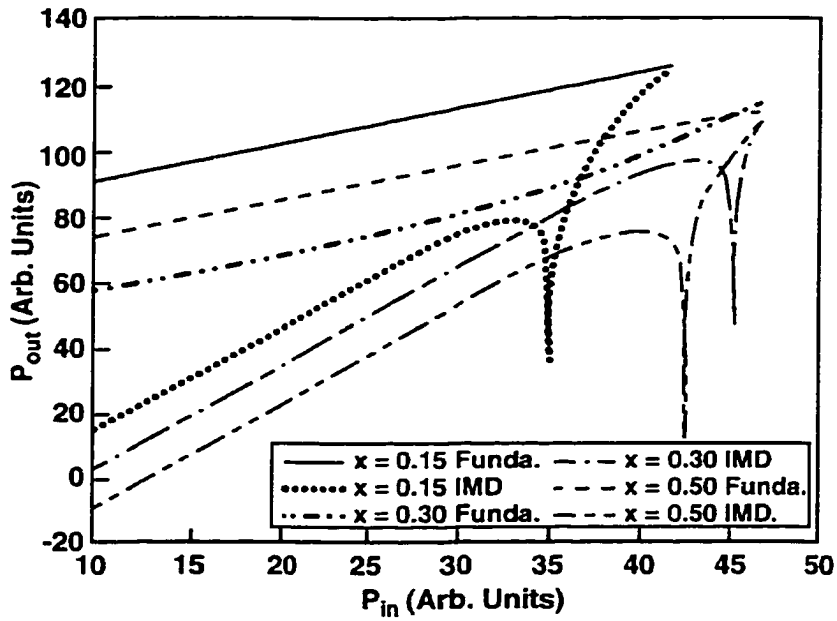

Fig. 4.15. Calculated output-input power characteristics for the fundamental and third-order inter-modulation frequencies. Mole fractions of 0.15, 0.30 and 0.50 were used for the barrier layer.

The following features of interest can be discerned from Fig. 4.15:

(i) The third-order intermodulation curves exhibit a local minima for all three mole fractions. Such behavior has been reported for GaAs transistors [118,119] and so, is consistent with experimental observations. At low input power, the curves all follow the simplified theory that predicts a constant 3 dB increment in distortion for every decibel of input power.

(ii) For optimal results, it would clearly be best to operate the device at an input power level that corresponds to the IMD minima, since the differential between the fundamental and IMD outputs is then the greatest. This, in theory, would allow for superior device operation at relatively input powers larger than predicted by a conventional assessment.

(iii) The lowest power output at the fundamental frequency is for the x=0.3 case. This outcome is expected from Fig. 4.13, which as discussed previously, reveals a nearly constant current response for large signal amplitudes limited to 2 Volts. By the same reasoning, the fundamental output for x=0.15 is the best, since the corresponding curve of Fig. 4.13 has the most linear characteristic of the three.

(iv) Despite low output power at the fundamental for x=0.3, there would seem to be two inherent advantages. First, the characteristics are predicted to have gain expansion at higher voltages. Such gain expansion has been reported in the literature [118]. Second, the operating power corresponding to the IMD minima is the largest for x=0.3.

As expected, the 300 K curve is generally higher due to increased carrier drift velocity resulting from lower phonon scattering, except near the V_G threshold. Carrier densities at the two temperatures are nearly the same, expect for a slightly more negative gate threshold for the 600 K case. Hence, the curves are generally controlled by the carrier drift term, but show a somewhat larger current at 600 K close to the gate threshold value.

Furthermore, since phonon scattering is strongly temperature dependent, while interface roughness scattering is not, the relative role of IRS is reduced at 600 K. Hence, for the 600 K case, the velocity variation (and thus the current density) tends to flatten

out, showing a weak V_G dependence at the larger gate voltages. Overall, the 600 K characteristic is smoother, and is perhaps a closer approximation to a linear curve as compared to the 300 K result. Thus crudely, one might expect lower distortion for higher temperature operation.

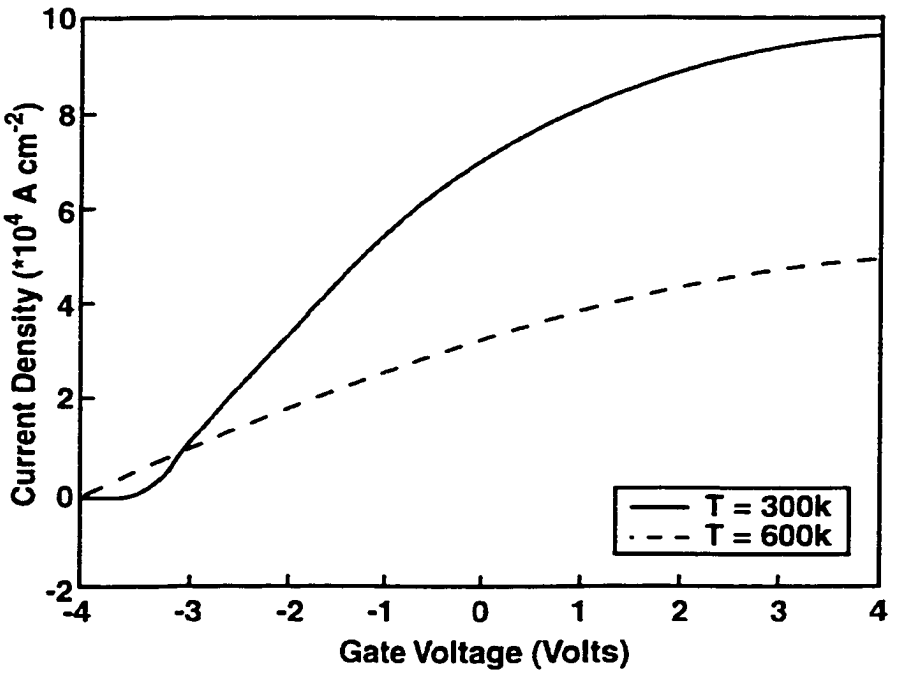

Fig. 4.16. Comparison of the calculated V_G dependent current density at 300 and 600 Kelvin for an Aluminum mole fraction of 0.15.

The large-signal response at an elevated temperature of 600 Kelvin was analyzed next for a relative comparison with room temperature results. Simulation predictions obtained for the current density as a function of V_G are shown in Fig. 4.16 for x=0.15.

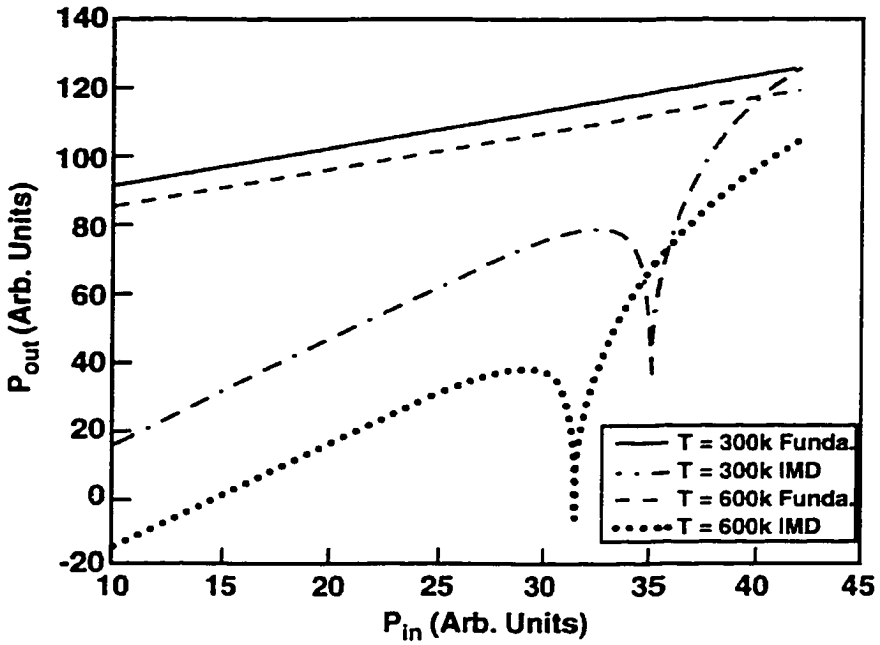

Fig. 4.17. Comparison of the calculated output-input power characteristics for the fundamental and third-order intermodulation frequencies at 300K and 600K. A mole fraction of 0.15 was used.

The input-output power characteristics obtained from equations 4.10-4.13 through polynomial curve fits to the data of Fig. 4.16 are shown in Fig. 4.17. Looking only at the fundamental frequency, the output power at 300K exceeds that at 600K. This in itself seemingly favors room temperature operation. This result is the direct consequence of a greater drift velocity and hence, device current, at 300K due to lower total scattering. However, the IP3 curve for 600 K is substantially smaller than the corresponding 300K characteristic and exhibits a much larger differential. Thus, for better device performance in terms of an IP3 differential alone, the 600 Kelvin operation seems to be the favored alternative. Furthermore, the fundamental and IP3 curves at 300 K are seen to intersect

over the input range considered, while those for 600K do not. These results are thus indicative of potential benefits for device operation at elevated temperatures.

Finally, direct full-Monte Carlo calculations for the HEMT were performed to gauge the response to two-tone, large-signal inputs. Instead of using polynomial fits to the steady-state velocity-field data as generated by a Monte Carlo calculation, a full dynamic MC simulation of the current response to a two-tone, time varying signal was performed. The MC-based approach was undertaken for the following reasons.

(i) It provides a much better dynamical treatment of the carrier transport.

(ii) The results serve as a validity check to the analytical fits that were used on the basis of equations 4.7-4.13.

(iii) All memory effects, which were absent from the polynomial expressions, could be included. Also, in effect, this naturally allowed a voltage dependence to the various coefficients K_i.

(iv) The inclusion of distributed internal effects. In the analytical approach it is assumed that the current changes instantaneously in response to the applied signal uniformly. The MC, however, takes account of the spatial distributions and temporal delays.

The results for the fundamental and IP3 are shown in Fig. 4.18 at 300 K for x=0.15. Running the MC simulator for a discrete set of V_G large-signal amplitudes generated the required data points. The time-dependent current density response was recorded for each input two-tone signal. Due to the computationally intensive nature of the simulations, only a few discrete V_G amplitudes were chosen. The use of relatively few V_G points, coupled with the statistical nature of the MC simulation, yielded curves

that were less smooth compared to those of Fig. 4.14 that resulted from the analytical fits. Similarities between the curves of Fig. 4.17 and the 300K analytical results of Fig. 4.16 are apparent.

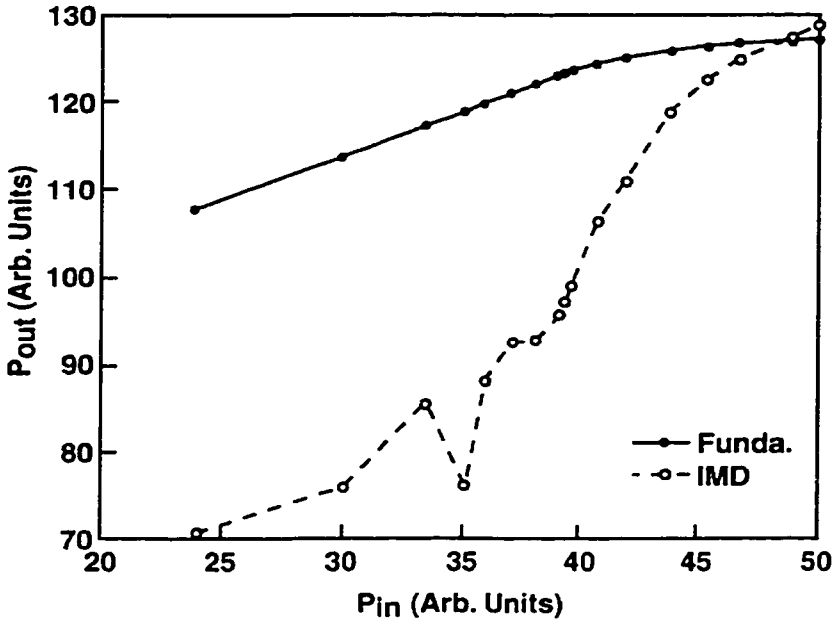

Fig. 4.18 Direct Monte Carlo results of the output-input power characteristics at 300K for a mole fraction of 0.15.

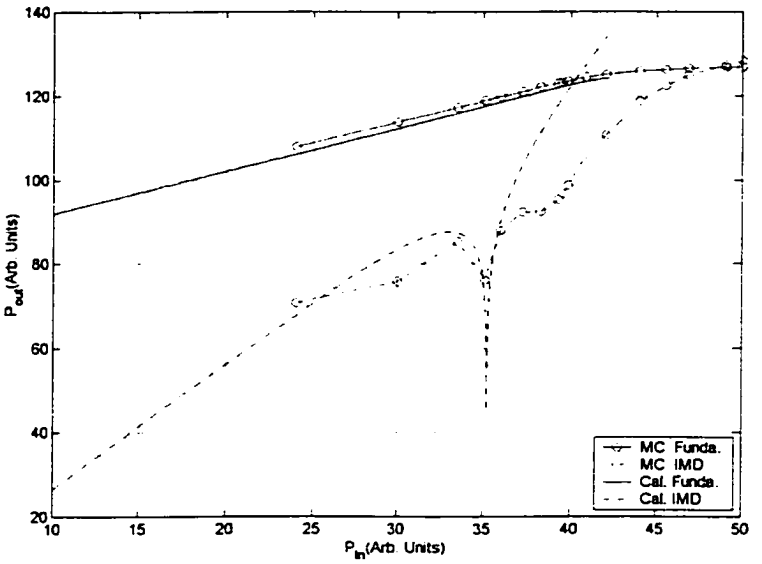

Fig. 4.19. Direct Monte Carlo and calculated results of the output-input power characteristics at 300K for a mole fraction of 0.15.

The direct Monte Carlo and calculated results of the output-input results for the fundamental and IP3 are shown in Fig. 4.19 at 300 Kelvin. In both cases, the IMD minima occurs at a value of about 35, though the analytical curve of Fig. 4.15 is much smoother. Minor differences include a more pronounced saturation (especially at the fundamental) and a higher cross-over point from the Monte Carlo calculations. The disparity is indicative of the internal memory and distributed effects that only the MC calculations can fully account. This demonstrates that for accurate and precise predictions, full MC calculation would be necessary.

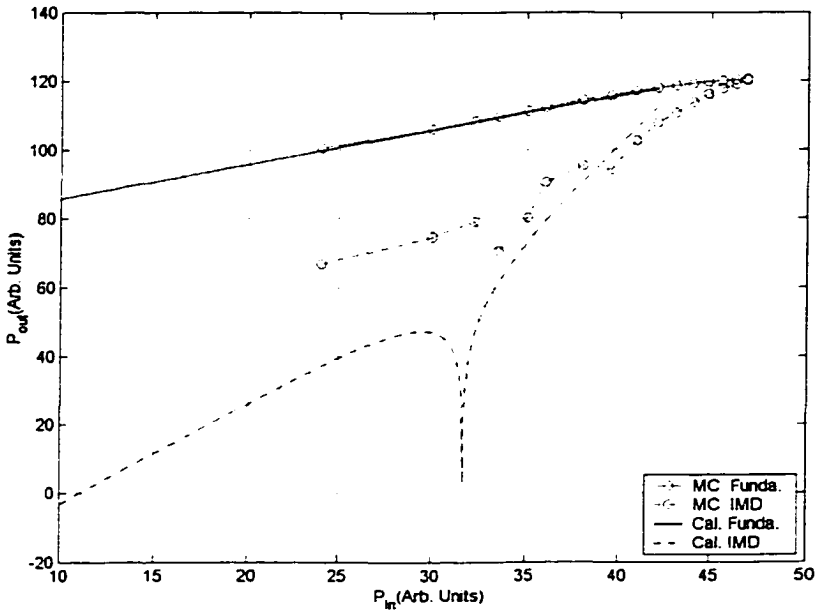

Fig. 4.20. Direct Monte Carlo and calculated results of the output-input power characteristics at 600K for a mole fraction of 0.15.

Fig. 4.20 shows the direct Monte Carlo and calculated results of the output-input results for the fundamental and IP3 at 600 K. We can draw the same conclusion as obtained for 300k, with some minor differences. In both cases, the fundamental curves are almost the same. Furthermore, the IMD has a minimum as before. However, the IMD minimum of as predicted by the direct MC simulations is around 34 units of input power at a 67 units of output power. The IMD minima based on the analytical formulation is around 32 units of input power, but predicts only about 10 units of output power. So while the whole trend is similar, the direct MC result is much higher than the discrete-analytical calculation based results.

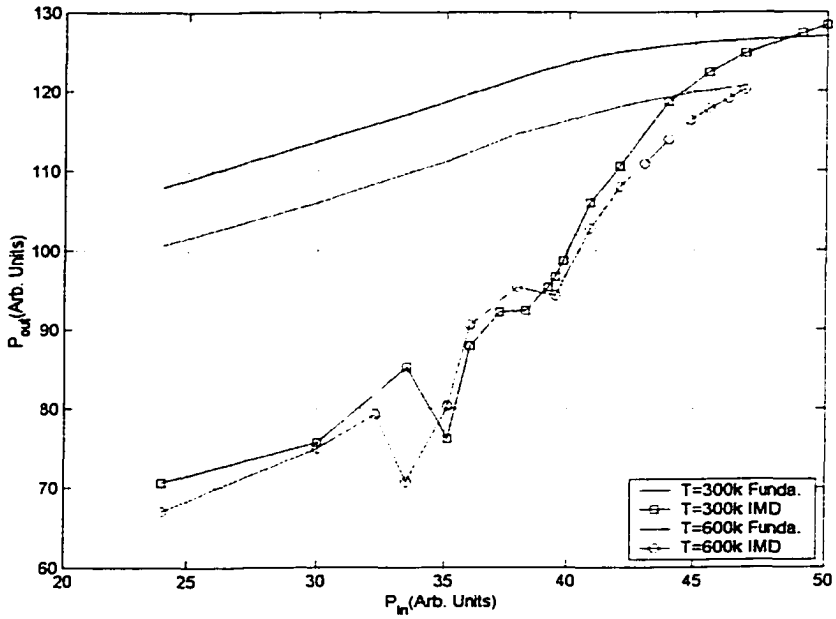

Fig. 4.21. Comparison of the direct Monte Carlo output-input power characteristics for the fundamental and third-order intermodulation frequency at 300K and 600K. A mole fraction of 0.15 was used.

In order to better understand the two-tone power depression at various temperatures, the direct Monte Carlo output-input power characteristics at 300K and 600 K for the fundamental and third-order intermodulation frequencies are put together in Fig. 4.21. With increasing temperature, both the fundamental and IMD signals decrease due to higher electron scattering with phonons since the phonon populations are intensify with temperature. Also, the IMD minima shifts somewhat from the 35 input power value to a magnitude of 33 units. The difference in power between the fundamental and IMD signals 300K is 42 (i.e. 118-76=42), while for 600 K it is about 38 (i.e. 108-70=38). This implies that the amplification behavior for the device used at 300k is somewhat better than the higher 600 K operating point. It can be mentioned that device noise has been

ignored in this work. The noise figure at elevated temperatures always degrades due to contribution from thermal noise. Hence, including the noise issue would further worsen the 600 K operating condition.

Next, for completeness, the same simulation scheme and parameters were implemented for a different gate signal frequency. In this case, a gate voltage frequency of 5GHz was chosen. The intent was to generate more data and better understand the frequency behavior of the GaN HEMT devices. Figure 4.22 shows the direct Monte Carlo results of the output-input power characteristics at frequency 5GHz. The results were obtained by using the same parameters except for the difference in frequency.

HEMT devices are usually designed for wide-band operation and need to function well over a range of high frequencies. This feature should also be borne out in simulations, if the numerical analysis is to accurately predict device behavior. Hence, simulations at different frequencies, as mentioned above, were carried out for accuracy and validity checks. Simulation results for the GaN HEMT are shown in Fig. 4.23 for a mole fraction of 0.15 and temperature of 300 Kelvin. Both direct Monte Carlo and analytically calculated results of the output-input power characteristics at frequencies of 5GHz and 20GHz are shown. As can be seen from the figure, the IMD minima occur at the same point and are nearly identical at the two frequencies. This clearly indicates that the consistency of results from the simulator developed here and underscores that it can be used for accurate predictions for a variety of HEMT applications.

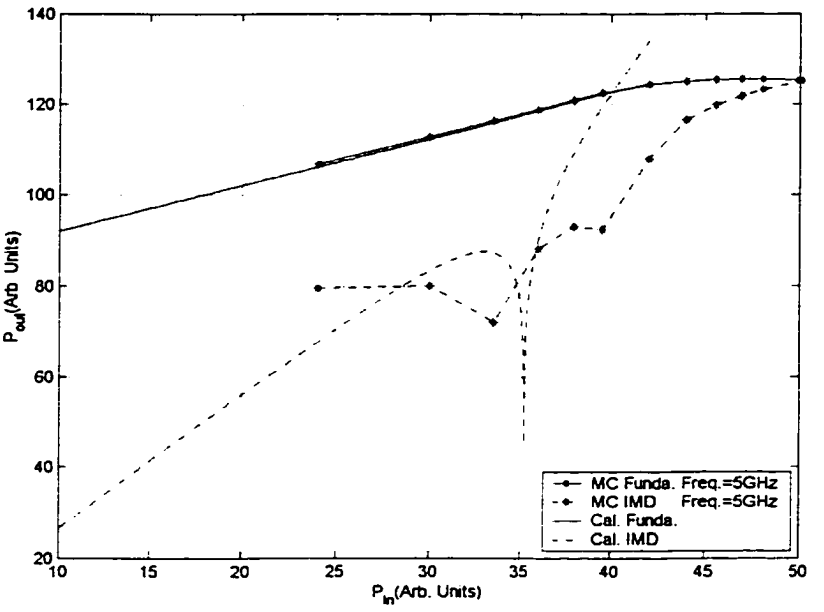

Fig. 4.22 Direct Monte Carlo and calculated results of the output-input power characteristics at frequency 5GHz for a mole fraction of 0.15 at 300K.

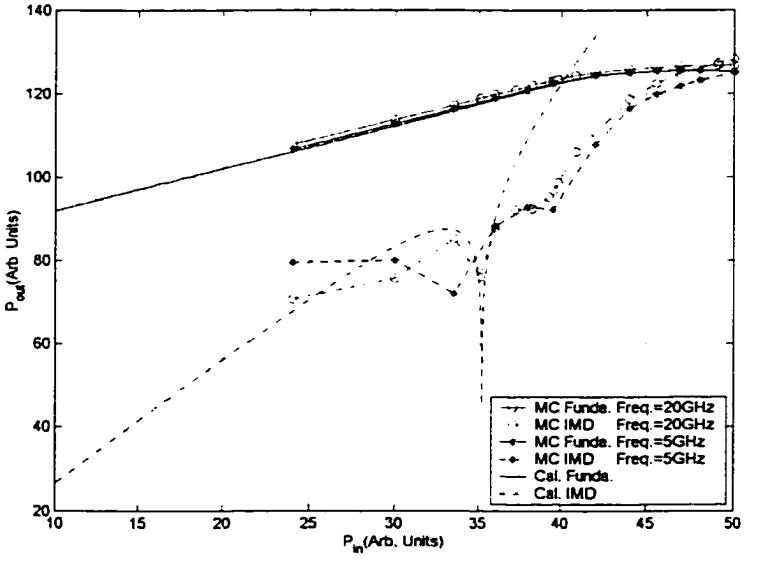

Fig. 4.23. Direct Monte Carlo and calculated results of the output-input power characteristics at frequency 5GHz and 20GHz. The mole fraction of 0.15 at T=300K.

4.5 Research on Real Space Transfer (RST)

4.5.1 Physics of RST and simulation schemes

In the results and discussions thus far, the real space transfer (RST) process whereby electrons can physically move from the GaN channel into the AlGaN barrier region was not taken into account. However, experimental reports in the literature indicate some peculiar phenomena in GaN HEMTs operating at high voltages. These observations include drain current compression and large-signal gains that are lower than those based on simple theoretical predictions. Therefore, it is conceivable that mechanisms such as RST are playing an important role and modifying the transport behavior in AlGaN/GaN system. RST could alter the current response by weighting the electronic conduction towards the high mass, low-mobility AlGaN region. This can be expected to become critical at high drain voltages as the electrons become capable of picking up large energy from the applied field. For example, during periods of higher positive gate voltages, more electrons would undergo RST effectively reducing the drain current I_D associated with the mobility suppression in the AlGaN layer. This clipping in I_D would exacerbate the nonlinearity and lower the dynamic range. Such effects are investigated in the final section of this dissertation research.

In this section, AlGaN/GaN HEMT system with RST effect will be fully explored. With RST, Monte Carlo simulations results show that the velocity, IMD and dynamic range are all affected by the electric fields along the channel, the operating temperature and gate length characteristic. Also, comparisons between the IMD simulation results with and without RST are provided here at different temperatures and electric fields for a clarifying analysis.

Simulation of the RST was carried out by first assigning all electrons to the GaN channel. This assumes that prior at any applied electric field, the electrons would populate the lowest energy states. Thus, at the beginning of the RST simulation all the electrons are assumed to stay in the two-dimensional electron gas system. The two-dimensional system is formed by the spatial confinement of the electrons due to the AlGaN/GaN conduction band-edge discontinuity on one side and the conduction band bending on the other due to the applied gate potential to form a triangular quantum well as shown in Fig. 2.8. For simplicity, only the first two subbands are shown. Once within the triangular well, the electron's motion is subject to the physics of the two-dimensional system; the transverse z direction is quantized. The scattering mechanisms are then described by a two-dimensional formulation, with the energy being simply given by:

$$E = E_i + \frac{\hbar^2}{2m^*}(k_x^2 + k_y^2), \tag{4.16}$$

where E_i is the subband energy. Therefore, the electron k vector component in the z direction remains fixed during its flight while the x and y components change in accordance with the action of the applied electric field.

For electron energies greater than that corresponding to the band barrier, the electrons are assumed to move into the three-dimensional GaN system. This is reasonable, since at high energies within the quantum well, the quantum levels become closely spaced forming a quasi-continuum band of states as in a bulk material. Upon drifting to lower energies (for example, due to phonon emission processes) those electrons lying below the barrier height would effectively transfer into the two-dimensional states. Though this approach is somewhat artificial, the net result is physically correct; when the electrons are at energies below the top of the well, they are

treated as belonging to the two-dimensional system. At energies above the barrier threshold, they can be assigned to the AlGaN layer.

In the above description, RST is field assisted whereby electrons pick up the requisite energy through accelerations produced by the driving electric field. In addition, coupling of the two-dimensional system to the three-dimensional bulk AlGaN, can also occur through phonon scattering events. At electron energies near the top of the quantum well, the electrons can scatter to three-dimensional states within the bulk AlGaN by picking up energy via phonon absorption processes. Similarly, the electron can enter the quantum-well system from the bulk via polar optical phonon emission events. The extent to which the electrons transfer from the quantum system to the bulk, and vice versa, depends upon the relative strength of the polar optical scattering. Thus, the relative rates of the two-and three-dimensional transitions dictate the particle dynamics and final states. Upon reaching energy greater or equal to the well height, the electrons are placed within the AlGaN environment, and produce currents dictated by the transport properties of the AlGaN material.

In the two-dimensional system, the electron motion is subject to various two-dimensional scattering mechanisms, particularly, polar optical phonon, acoustic phonon alloy and remote impurity scattering. In our simulation of the two-dimensional system, the subbands are assumed to from only in the Gamma valley. The L- and X-valleys were treated as three-dimensional since the intervalley separation energies for the L and X minima exceed the potential well height. Therefore, intervalley scattering events were neglected. The two-dimensional scattering rates were calculated including both intra and

inter-band scattering processes using the trial wave functions of Yamaguchi [121]. The full details of these calculations have been reported elsewhere [122].

The final state of the electron after suffering a two-dimensional scattering event is found in a similar way to that for bulk material [123] except that the k vector component in the z direction remains fixed. However, the k vector component in the x and y directions changes in accordance with the physics of the scattering event. Therefore, only one scattering angle is necessary to determine the final state after a two-dimensional scattering event.

4.5.2 Simulation Results and Discussion

In order to demonstrate the RST effect and show its consequences, a simple simulation experiment is implemented for the AlGaN/GaN system. A mole fraction of 0.15 and temperature at 300K were used. Fig. 4.24 shows snapshots of electron populations along in the x-z plane at different time instants. For simplicity, 1000 electrons are used for this demonstration simulation. In the figure, time snapshots of 0 fs, 5 fs, 25 fs; 50fs, 100fs and 500 fs are shown from left to right. Initially, all the electrons are intentionally set within the two-dimensional conduction channel. Thus, in the figure, all the electrons are shown at the origin of the x-z plane. After this initialization, the electron begins to move along conduction channel due the effect of the lateral electric field and change their positions as time moves on. At the 25 fs time slot, Fig. 4.24 reveals that some electrons have been offset along the z-direction. This is the result of some electrons gaining enough energy to overcome the quantum-well barrier. They,

consequently, move from two-dimensional confining well, into the three-dimensional AlGaN bulk material. Once the electrons are in the AlGaN due to RST, they can then undergo drift along the z-direction due to the z-field set up by the applied voltage. As time elapses, more and more electrons enter into the bulk AlGaN side from the GaN channel. Hence, electrons begin to move and conduct a current in both AlGaN and GaN materials. The RST effect thus occurs and is seen easily from the sequence of pictures given in Fig. 4.24.

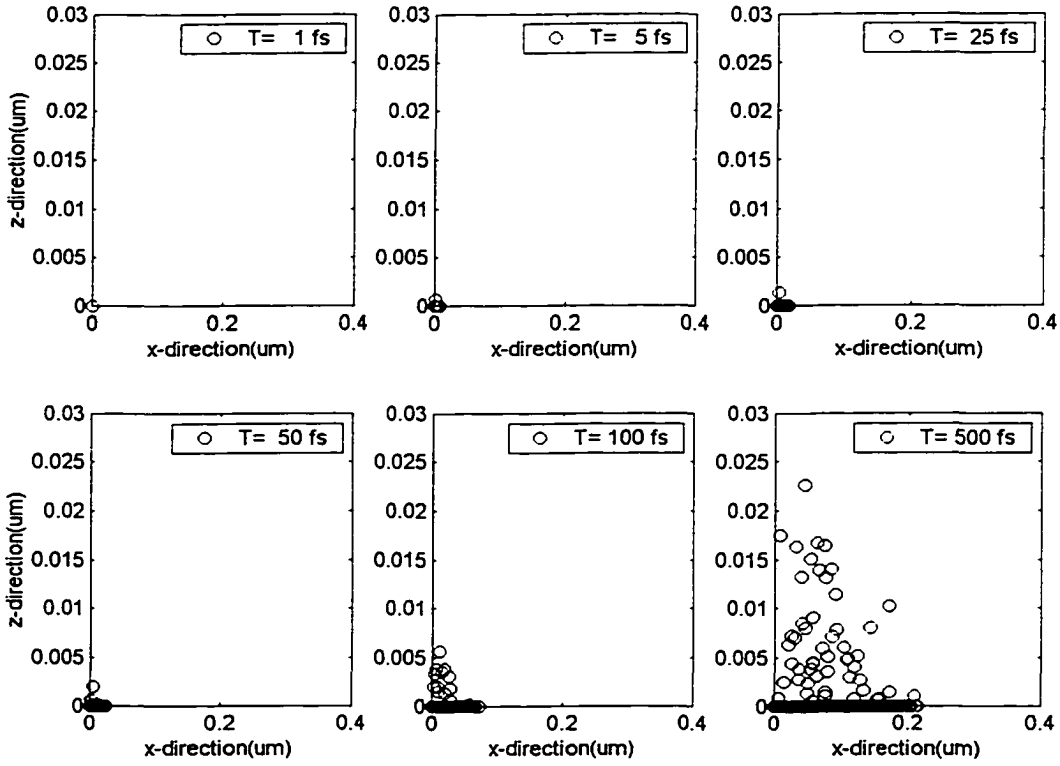

Fig. 4.24. Electrons population along the intersection plane of x- and z- direction at different time slots.

In the RST simulation programs, 10000 electrons were used for the Monte Carlo procedure. A fixed 0.15 Aluminum mole fraction was chosen in the AlGaN layer for concreteness. Different operating temperatures and gate lengths were used to simulate and probe the transport behavior. Initially, all the electrons were assigned random locations at the GaN channel. There the particles could undergo drift based on Newtonian mechanics and constant scattering within the two-dimensional GaN conduction channel. Next, a gate voltage and lateral electric field were applied in this simulation model. By varying bias, temperature or gate lengths, a variety of simulation results could be obtained for gauging the effect of these parameters on the electrical response of the GaN HEMT with the inclusion of RST.

Fig. 4.25 shows the direct Monte Carlo simulation results at different electric fields with the RST effect included. An ac gate voltage having a large-signal amplitude of 1.5 V and a 20 GHz frequency was used. Based on the results shown in Fig. 4.25, the following general observations can be made.

1. Since a voltage with cosine time-varying function is applied to the gate terminal, the AlGaN/GaN device response fluctuates continually in response to the gate voltage changes. When the gate voltage increases, more electrons move from the GaN layer towards the AlGaN; while gate voltage decreases force a relative accumulation of electrons on the GaN side at the expense of the AlGaN population.
2. Electron transient velocity is affected by the gate voltage as well. In response to fluctuations in gate voltage, electrons move back and forth between the bulk AlGaN layer and the two-dimensional quantum channel. However, the particle scattering in

the AlGaN layer is higher than in GaN due to a higher density of states (that arises from the larger effective mass) and to the presence of an additional alloy scattering process. Consequently, the overall device velocity is smaller when more electrons populate the AlGaN layer, and vice versa.

3. As a result, the current density also exhibits fluctuations due to the direct relationship between the current magnitude, the electron density and the average drift velocity.

Next, comparisons are made between longitudinal electric field of 5 x 10^5 V/m and 3 x 10^6 V/m. At higher fields (which correspond to larger applied drain voltages), the electrons in the GaN channel are likely to pick up more energy during their transit from the source side. Consequently, one expects more RST than at higher values of the electric field. The overall current, however, depends not only on the relative population distribution between the two channels (one slower than the other), but also on the magnitude of the drift velocity, which increases with the electric field. Thus, the higher drift velocity and larger RST at increased electric fields, in a sense, work to oppose each other.

From Fig. 4.25, it is clearly that there is not much of an effect on the electron distributions in the AlGaN and GaN layers. The electron numbers remain almost identical at the two different lateral electric field values. However, the velocity does change dramatically with the electric field. Electrons in GaN, for example, can gain more energy and are thus able to move faster at the larger lateral electric field value. A lower average velocity results at the smaller electric fields.

Device current density is the product of the electron number and electron velocity. The results here show that the electron distribution between the two material channels has a much smaller effect. Consequently, the current density trend is mainly affected by the velocity factor.

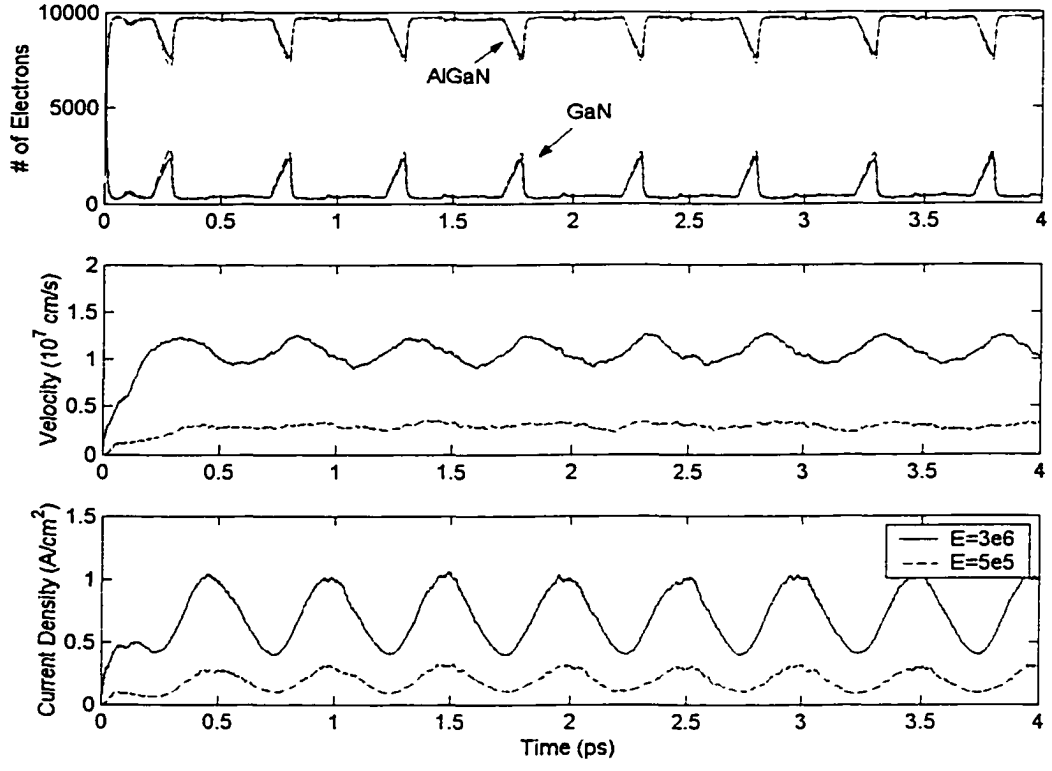

Fig. 4.25. Direct Monte Carlo transient simulation results at different electric fields with RST included. Temperature is 300 Kelvin.

From Fig. 4.25, one can draw the following conclusions. At low electric field strengths, the carriers remain within the two-dimensional quantum well. As the electric field increases, the electrons begin to transfer out of the two-dimensional system into the three-dimensional GaN states. Once in the three-dimensional bulk, the electrons can be

further heated to sufficiently high energy at which real-space transfer into the surrounding AlGaN layer can occur. Under certain bias conditions, a significant portion of the drain current flows through a stray path in the AlGaN layer. Due to the large concentration of impurities present and subsequently high scattering rate, the higher electron effective mass, and the loss of considerable kinetic energy upon crossing the heterojunction interface, the device performance is considerably degraded when sizeable current flows within the AlGaN layer.

The steady-state velocity-field characteristics for 2D electrons with and without RST effect also investigated. The comparison results are shown on Fig. 4.26. A 3 V gate voltage was assumed, with conduction channel length 0.4um at T=300 Kelvin.

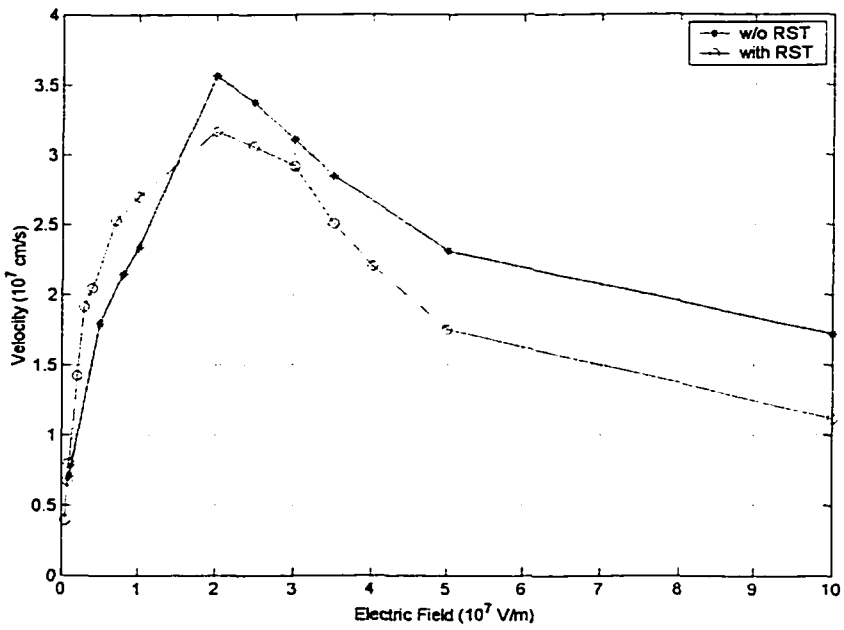

Fig. 4.26. Steady-state velocity-field characteristics for 2D electrons with and without RST effect. Gate voltage of 3 volts at T=300 Kelvin was used.

For this chosen condition, both velocity-field curves show an overshoot. This would be indicative of negative differential resistance (NDR), and can potentially generate unstable or oscillatory device response. At first, the velocity increases with increasing electric field. At an electric field value of around $2\times10^{7}V/m$, the velocity reaches a peak. For fields beyond this value, the drift velocity begins to decrease dramatically. At low electric fields, the velocity with RST is a little higher than that without RST. But at higher electric field, velocity with RST is much lower than that without RST. This is because the higher scattering that occurs on AlGaN side.

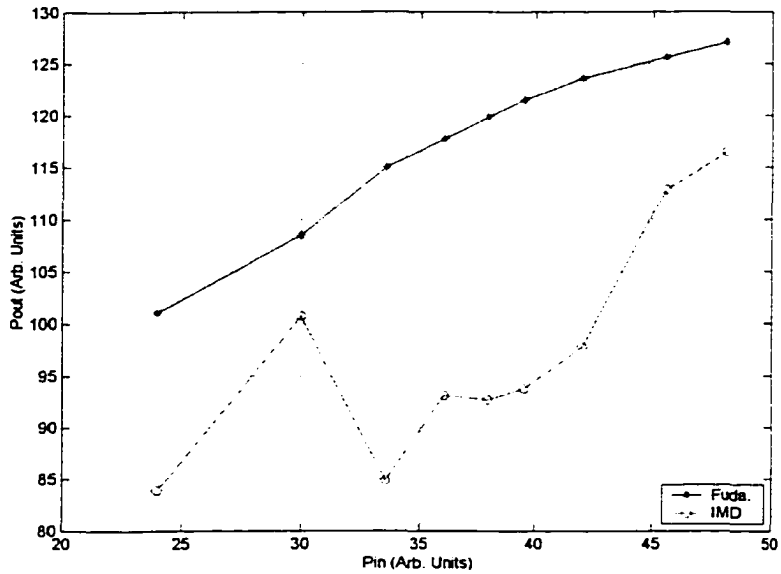

Fig. 4.27. Direct Monte Carlo results of output-input power characteristics with RST at 300K. A mole fraction of 0.15 and electric field of $1\times10^{6}V/m$ were used.

The direct Monte Carlo results with RST for the fundamental and IP3 are shown in Fig. 4.27 at 300 K for x=0.15. Running the MC simulator for a discrete set of V_G

large-signal amplitudes generated the required data points. The time-dependent current density response was recorded for each input two-tone signal. Due to the computationally intensive nature of the simulations, only a few discrete V_G amplitudes were chosen. The use of relatively few V_G points, coupled with the statistical nature of the MC simulation, yielded curves that were less smooth compared to those of Fig. 4.15 that resulted from the analytical fits. The trends in the results are similar to those obtained from simulations carried out without RST. The IMD minima occurs at a value of about 33 units.

The effects and role of RST on the input-output power characteristics of the device is probed more clearly through the curves of Figs. 4.28, 4.29 and 4.30. These figures show comparisons between Monte Carlo simulated and calculated output-input power characteristics with and without RST.

Fig. 4.28 is the comparison of calculated results of the output-input power characteristics with and without RST at 300 Kelvin. The third-order intermodulation curves exhibit a local minima at around 35 units, both with and without RST. The output power characteristic at the fundamental frequency remains almost unchanged. The figure

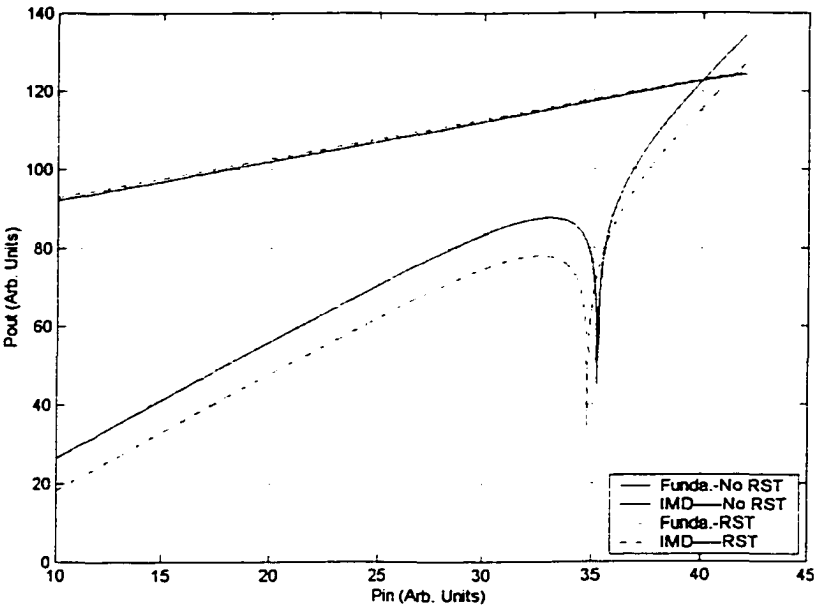

Fig. 4.28. Comparison of calculated results of the output-input power characteristics with and without RST. Temperature is 300 Kelvin.

also shows that at the same input power the IMD power response with RST is a little smaller than that without RST. Hence, from an amplification point of view, RST will be somewhat beneficial and advantageous to the device RF performance, by reducing the harmonic content.

Fig. 4.29 is the comparison of direct Monte Carlo results of the output-input power characteristics with and without RST at T=300 Kelvin. It is obvious that they are not as smooth as the analytical curves of Fig. 4.28. Some differences include a slight shift in the IMD minima with towards the left and a higher input power at the cross-over point.

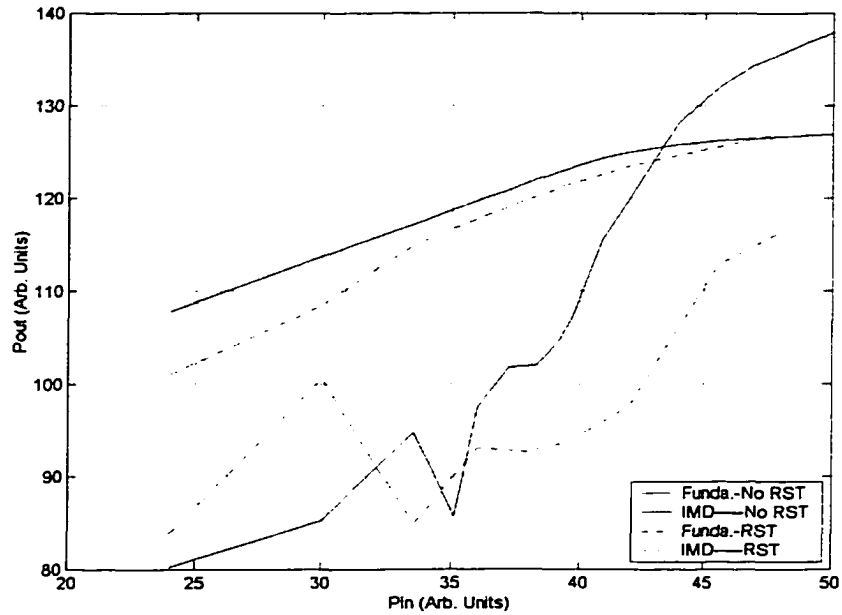

Fig. 4.29. Comparison of direct Monte Carlo results of the output-input power characteristics with and without RST.

Fig. 4.30 shows the comparison of direct Monte Carlo and calculated results of the output-input power characteristics with RST at T=300k. The figure is obviously indicative of several differences. The disparity might arise from factors such as the internal memory and distributed effects that only the MC calculations can fully take into account. This demonstrates that for accurate and precise predictions, full MC calculation would be necessary.

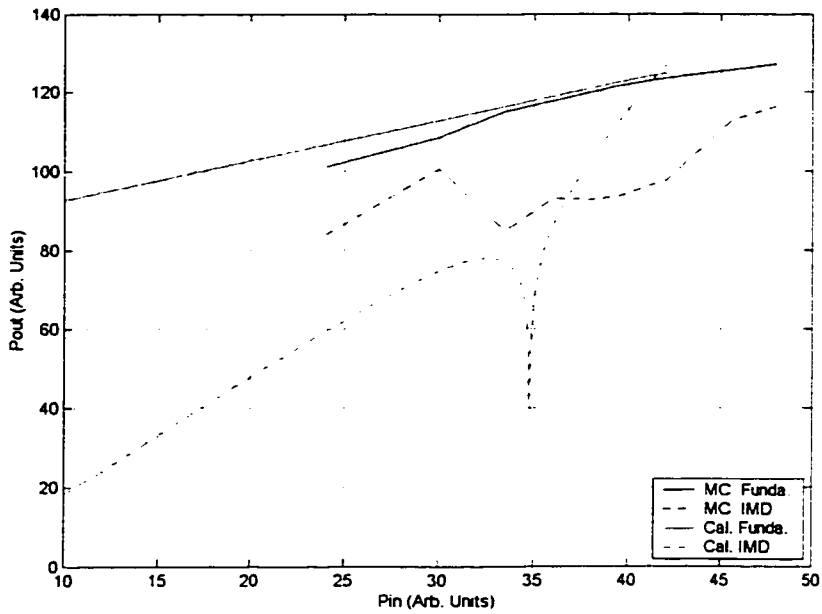

Fig. 4.30. Comparison of direct Monte Carlo and calculated results of the output-input power characteristics with RST.

Finally, the velocity comparisons are provided for different temperature and different gate length with the RST effect taken into account. Fig. 4.31 is the velocity and electron profile at an elevated temperature of 600 Kelvin. This figure should be used for a relative comparison with room temperature results without RST. The same ac large-signal gate voltage of amplitude 1.5V and a 20GHz frequency was used. As evident from the plots of Fig. 4.31, at the higher temperature more electrons tend to stay on the AlGaN side, and the velocity is much lower compared to the regular temperature. Also, many more fluctuations can be seen. This is indicative of higher noise caused by larger phonon scattering at the elevated temperatures.

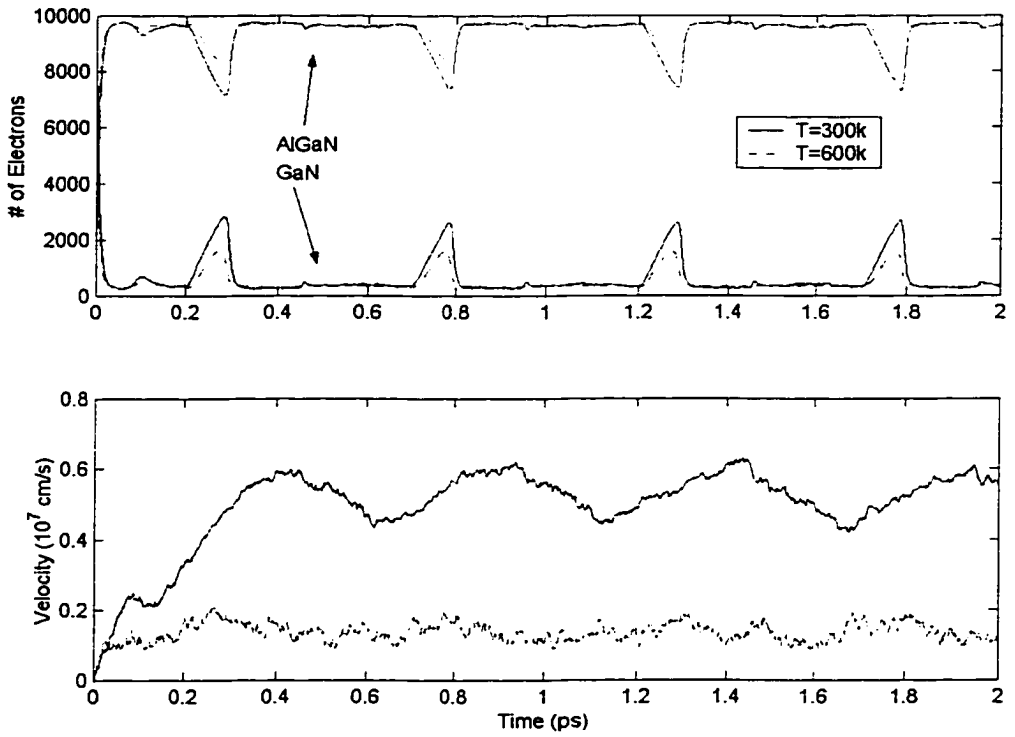

Fig. 4.31. Direct Monte Carlo transient simulation results at different temperature with RST.

Fig. 4.32 is the velocity and electron profile at a narrow gate length. With a smaller gate length, electrons traversing the GaN channel from the source to the drain have a shorter transit time. As a result, the energy gained by the particles (for a fixed lateral electric field) is correspondingly lower. Also, there is a lower probability of the particles to be able to successfully scatter into the AlGaN barrier before they arrive at the drain collection electrode. Once at the drain end, the electrons would get absorbed by the Ohmic contact and not have a chance to transfer to the AlGaN side. One, therefore, expects that the RST will not be as large or significant as a device with a longer gate length. This point is probed more extensively through the simulations presented in Fig.

4.32. In this case, for the narrower channel length (0.1um compare to 0.4um) more electrons are retained at GaN side, and the velocity is a little higher than the 0.4um case.

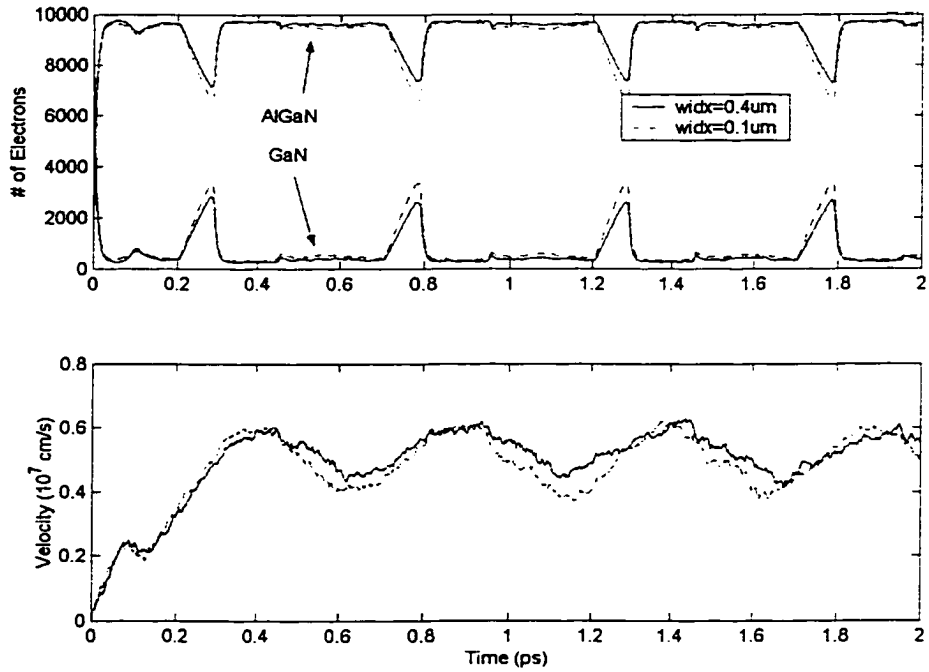

Fig. 4.32. Direct Monte Carlo transient simulation results at different gate length with RST.

CHAPTER 5

CONCLUSIONS AND FUTURE RESEARCH

5.1 Research Summary for the GaN/AlGaN System

In this research, evaluations of the electrical transport characteristics of GaN/AlGaN system were obtained. First principle Monte Carlo simulators were set up to meet the research requirement. Such Monte Carlo simulators are known to be very accurate and do not need any measured electrical data sets as adjustable input parameters. The technique is therefore very useful in studying new material systems for which experimental results are not available *a-priori*. Though the Monte Carlo scheme is well known in the context of semiconductor transport studies and has been applied to many of the commonly used materials, it has not been used much for GaN and related nitride materials. The Monte Carlo simulations for GaN/AlGaN that have been developed here are a contribution in this field.

Results of the Monte Carlo calculations seemed to correlate well with some of the experimental data that is becoming available. Both the bulk and quantized inversion layer simulations matched the experimental observations. The advantages of high voltage operation in terms of superior transport properties over conventional Si and GaAs materials were also assessed and quantitatively demonstrated.

Monte Carlo simulations for electronic transport in wurtzite GaN have been carried out for bulk and HFET structures. The bulk calculations were intended to serve as a validity check of the simulation model and yield a set of best-fit transport parameters through comparisons with previous work. The results matched Monte Carlo predictions

reported in the published literature based on a full-bandstructure calculation, up to electric fields of 400 kV/cm. Wurtzite GaN was shown to have superior steady-state drift velocity characteristics over both GaAs and the zinc blende phase of GaN. Next, electron mobility in HFET structures was analyzed, taking account of polarization effects, degeneracy and interface roughness scattering. Degeneracy was shown to play an important role, especially at large gate bias values. Very good agreement with available experiments was obtained. Our results underscored the dominance of interface roughness scattering (IRS) and demonstrated that a parameterized model based on a weak-perturbation, Born approximation theory can yield sufficiently accurate results. Finally, steady-state characteristics for GaN-AlGaN HFET structures were also obtained at 300 K and the high operating temperature of 600 K. Degeneracy was shown to play an important role, especially at large gate bias. Very good agreement with available experimental mobility could only be obtained upon the inclusion of degeneracy.

The large-signal nonlinear response characteristics of GaN-AlGaN HEMTs, with particular emphasis on intermodulation distortion (IMD) and the third-order intercept point (IP3) were also studied in this dissertation research. These are important transistor performance measures for applications that require high-power, large-signal amplification. For optimal design it becomes necessary to understand the IMD characteristics and subsequently, devise ways to increase the IP3 operating point and dynamic range. Here the GaN material system was chosen for analysis since it is relatively new and holds promise for high-temperature operation. It is therefore appropriate to evaluate the device operation and to make performance comparisons between normal and elevated temperature operation for potential benefits.

Since the device current and details of the non-linearity that gives rise to IMD depend critically on the carrier transport behavior, a Monte Carlo (MC) based numerical simulation scheme was employed to include the microscopic details. In the process, all scattering mechanisms were treated comprehensively, and the nonlinear response included on first principle basis, rather than approximate analytical expressions as usually used in the literature. Besides, the MC approach allows for the inclusion of internal memory and spatially distributed effects. Two approaches were used to obtain the third-order inter-modulation and the fundamental output power for GaN-AlGaN HEMTs. In the simpler version, the velocity-field curves generated on the basis of MC simulations were used to generate analytical curve fits. These were then used to obtain the response to time-varying signals. In addition, full Monte Carlo calculations were carried out to evaluate the time dependent current response to two-tone, large-signal, gate voltages. The analysis demonstrated an optimal operating point at a reasonably large output power due to a minimum in the IMD curve. Such minima has been observed and reported in GaAs-based transistors. Furthermore, it was shown that the nonlinear characteristics depend on the barrier mole fraction. Hence, it is possible to select this parameter for optimizing device performance. Besides room temperature predictions, the behavior at 600 K was also probed. Based on the predicted high-temperature nonlinear behavior and IMD characteristics, it was shown that the IP3 point and dynamic range would not degrade significantly under elevated temperature operation. This probably results from changes in the drift velocity associated with the internal scattering processes, particularly the IRS. The results are encouraging and seem to make a case for GaN based high temperature amplifiers, especially suited under harsh and/or high-temperature environments.

In order to probe the transport physics governing the device operation further, the influence of various source-drain biases (longitude electrical field along the conduction channel) was examined. It was found that the steady-state electron drift velocity increases with the increment of longitudinal electrical field first. This is due to confinement of the electrons within the two-dimensional system near the source and beneath the gate. As the electrical field continually increases, the electron energies increase proportionately leading to significant velocity overshoot. Electron velocities well in excess of the steady-state values were predicted. Immediately thereafter, the electron drift velocity dropped precipitously due to the combined effects of transfer out of the two-dimensional system, intervalley transfer in the bulk AlGaN layers. Depending upon the gate bias, the velocity near the drain is limited by either K-space or real-space transfer. It was found that at low gate bias real-space transfer within the three-dimensional AlGaN system limits the carrier speeds.

Finally, the research works on the AlGaN/GaN system by taking RST effect into account. Real space transfer (RST) is reported as an important transport process in AlGaN/GaN system by experimentalists. It can possibly alter the current response and lead to memory effects. These would become critical at high drain voltages. With RST, Monte Carlo simulations results showed that the velocity, IMD and dynamic range are all affected by the electric field, temperature and gate length characteristics. Also, comparisons between the IMD simulation results with and without RST for the AlGaN-GaN material system were provided at different operating temperatures and electric fields.

5.2 Future Research Work

Ensemble Monte Carlo simulations were developed and applied to the study of the electrical behavior in the new promising III-V compound semiconductor GaN/AlGaN. This constitutes a significant "first-step." The study enabled a number of important conclusions to be made. However, more research work in this field can be carried out to improve predictions for the GaN/AlGaN characterization with regards to the electrical, thermal and frequency aspects. Some of these issues and possible future research work are discussed next.

(a) During the present research simulations, a constant and uniform electric field was assumed. However, in general, the flow of electrons and holes in an actual device will change the internal electric field distribution and carrier densities. This aspect will, therefore, need to be incorporated into future simulations for more accurate characterization. Poisson solvers possibly using the collocation technique would need to be used.

(b) Electron transport was studied through the Monte Carlo simulations. Electrons were chosen since they are usually more important to current conduction, and make the largest contribution. However, microscopic properties of the holes can also be computed. Hence, holes could be included as a next step with appropriate information about their effective masses and band structure. Unfortunately, some of these input parameters have not been obtained experimentally. These would be important to bipolar devices such as Heterojunction Bipolar Transistors (HBTs) and Thyristors.

(c) It should be pointed out that a number of other factors not considered here could become important in the final analysis. For example, the thermal noise level would be

higher for elevated temperature operation and affect the minimum detectable signal. Besides, the recombination-generation and 1/f noise components would also increase. Contributions to the latter could arise from electronic trapping-detrapping (TD) at the barrier layer across a distribution of tunneling depths, as in CMOS devices [122]. Aspects relating to device noise were not investigated here, but could be included in subsequent research.

(d) Optimization for GaN/AlGaN system electrical behavior based on a judicious selection of the different parameters is needed. These parameters include: gate voltage, channel length, source-drain voltage, undoped AlGaN space thickness, mole fraction and operation frequency. Future work could attempt to optimally choose an operating parameter set for a given device specification and application.

(e) For high-power microwave applications, it is expected that internal device heating will occur due to Joule energy dissipation. Consequently, variations in the device temperature are to be expected both spatially and in time. Such variations are likely to influence the transport properties by altering the carrier drift velocity, diffusion coefficients, phonon populations and hence scattering rates etc. In order to include these aspects comprehensively, it would be necessary to carry out a coupled electro-thermal modeling. Heat transport equations (based on Fickian diffusion) would need to be added to the present Monte Carlo model for self-consistency.

(f) Comparisons between AlGaAs/GaAs and AlGaN/GaN systems. Since, the AlGaAs-GaAs material system is better known and has been used for several years, its inclusion would provide a good baseline comparison.

REFERENCES

1. M. Bhatnager and B. J. Baliga, IEEE Trans. Electron. Dev. **40**, 645 (1993).
2. H. Morkoc, S. Strite, G. Geo, M. E. Lin, B. Sverdlov, and M. Burns, J. Appl. Phys. **76**, 1363 (1994).
3. R. J. Trew, J. B. Yen, and P. M. Mock, Proc. IEEE **79**, 598 (1991).
4. S. Pathak, in *Modeling and Simulations of High Field, High Temperature SiC Devices,* Ph.D. dissertation, Old Dominion University, Norfolk, VA (1998).
5. S. Nakamura, M. Senoh, and T. Mukai, Appl. Phys. Lett. 62, 1818 (1993).
6. M. Khan, D. Olson, and J. Van Hove, Appl. Phys. Lett. 58, 1515 (1991).
7. S. Strite and H. Morkov, J. Vac. Sci. Technol. B 19, 1237 (1992).
8. Y. F. Wu, B. P. Keller, S. Keller, D. Kapolnek, P. Kozodoy, S. P. Denbaars, and U. K. Mishra, Appl. Phys. Lett. 69, 1438 (1996).
9. S. N. Mohammad, A. Salvador, and H. Morkoc, Proc. IEEE 83, 1306 (1995).
10. H. Morkoc, in Nitride Semiconductors and Devices, (Springer-Verlag, Heidelberg, 1999).
11. R. P. Joshi, Appl. Phys. Lett. 64, 223 (1994); R. P. Joshi, A. N. Dharamsi and J. Mcadoo, Appl. Phy. Lett. 64, 3611 (1994).
12. S. Nakamura, T. Mukai, and M. Senoh, Appl. Phys. Lett. 64, 1687 (1994).
13. R. Gaska, Q. Chen, J. Yang, A. Osinky, M. A. Khan, and M. S. Shur, IEEE Electr. Dev. Lett. 18, 492 (1997).
14. S. Keller, G. Parish, P. T. Fini, S. Heikman, C. H. Chen, N. Zhang, S. P. Denbaars, and U. K. Mishra, J. Appl. Phys. 86, 5850 (1999).
15. R. Gaska, M. S. Shur, A. D. Bykhovski, A. O. Orlov, and G. L. Snider, Appl. Phys. Lett. 74, 287 (1999).
16. S. Nakamura, M. Senoh, S. Nagahama, N. Iwasa, T. Yamada, T. Matsushita, H. Kiyoku, Y. Sugimoto, T. Kozaki, H. Umemoto, M. Sano, and K. Chocho, Jpn. J. Appl. Phys. 38, 1578 (1997).
17. G. E. Bulman, K. Doverspike, S. T. Sheppard, T. W. Weeks, H. S. Kong, H. M. Dieringer, J. A. Edmond, J. D. Brown, J. T. Swindell, J. F. Schetzina, Electr. Lett. 33, 1556 (1997).

18. S. Nakamura, M. Senoh, N. Iwasa, S. Nagahama, T. Yamada, T. Mukai, Jpn. J. Appl. Phys. **34**, 1332 (1995).
19. M. Razeghi and A. Rogalski, J. Appl. Phys. 79, 7433 (1996).
20. I. J. Fritz and T. J. Drummond, Electr. Lett. 31, 68 (1995).
21. H. Morkoc and S. N. Mohammad, in Wiley Enclopedia of Electrical and Electronics Engineering (J. Wiley and Sons, New York, 1999).
22. L. Esaki and R. Tsu, IBM Res., Internal Rep. RC2418 (1969).
23. D. K. Ferry, in Gallium Arsenide Technology (H. W. Sams, Indianapolis, 1985).
24. H. Morkoc, IEEE J. Selected Topics in Quantum Electronics 4, 537 (1998).
25. K. Shenai, R. S. Scott and B. J. Baliga, IEEE Trans. Electr. Dev. 36, 1811 (1989).
26. U. Bhapkar and M. S. Shur, J. Appl. Phys. 82, 1649 (1997).
27. J. D. Albrecht, R. P. Wang, P. P. Ruden, M. Farahmand, and K. F. Brennan, J. Appl. Phys. 83, 4777 (1998).
28. W. F. Yu, B. P. Keller, P. Fini, J. Pusl, M. Le, N. Nguyen, C. Nguyen, D. Widman, 2.19.S. Keller, S. P. Denbaars, and U. K. Mishra, Electronics Lett. 33, 1742 (1997).
29. S. T. Sheppard, K. Doverspike, W. L. Pribble, S. T. Allen, J. W. Palmour, L. T. Kehias, and T. J. Jenkins, Electr. Dev. Lett. 20 161 (1999).
30. P. Das and D. K. Ferry, Solid-State Electron 19, 851 (1976).
31. M. Littlejohn, J. R. Hauser and T. H. Glisson, Appl. Phys. Lett. 26, 625 (1975).
32. N. S. Mansour, K. W. Kim and M. A. Litttlejohn, J. Appl. Phys. 77, 2834 (1995).
33. F. Brennan and Yang Wang, J. Appl. Phys. 78, 1033 (1995).
34. L. Kleinman and J. C. Philips, Phys. Rev. **118**, 1153 (1960).
35. M. L. Cohen and T. K. Bergstresser, Phys. Rev. **141**, 789 (1966).
36. P. O. Lowdin, J. Chem. Phys. **19**, 1396 (1951).
37. M. Fanciulli, T. Lei and T. D. Moustakas, Phys. Rev. B **48**, 15144 (1993).
38. W. J. Fan, M. F. Li, J. Appl. Phys. **79**, 188 (1996).
39. B. Gelmont, K. Kim, and M. Shur, J. Appl. Phys. **74**, 1818 (1993).
40. T. Ando, A. B. Fowler and F. Stern, Rev. Mod. Phys. **54**, 437 (1982).
41. S. M. Goodnick, D. K. Ferry, C. W. Wilmsen, Z. Lilienthal, D. Fathy, and O. L. Krivanek, Phys. Rev. B **32**, 8171 (1985).

42. J. R. Schrieffer, in *Semiconductor Surface Physics* (University of Pensylvania Press, Philadelphia, 1957).
43. K. Fuchs, Proc. R. Soc. **151**, 585 (1935).
44. D. Vasileska and D. K. Ferry, IEEE Trans. Electron Dev. **44**, 577 (1997).
45. R. P. Joshi, Appl. Phys. Lett. **72**, 2156 (1998).
46. T. Li, R. P. Joshi, and C. Fazi, J. Appl. Phys. **88**, 829 (2000).
47. L. Zhang and J. Singh, J. Appl. Phys. **85**, 587 (1999).
48. P. Lugli and D. K. Ferry, IEEE Trans. Elec. Dev. **32**, 2431 (1985).
49. O. Madelung, in *Introduction to Solid-State Physics* (Springer, Berlin, 1978).
50. T. Li, R. P. Joshi, and C. Fazi, J. Appl. Phys. (Sept., 2001).
51. O. Ambacher, J. Smart, J. R. Shealy, N. G. Weimann, K. Chu, M. Murphy, R. Dimitrov, L. Wittmer, M. Stutzmann, W. Rieger, and J. Hilsenbeck, J. Appl. Phys. **85**, 3222 (1999).
52. F. Bernardini, V. Fiorentini, and D. Vanderbilt, Phys. Rev. B **56**, 10024 (1997).
53. E. T. Yu, G. J. Sullivan, P. M. Asbeck, C. D. Wang, D. Qiao, and S. S. Lau, Appl. Phys. Lett. **71**, 2794 (1997).
54. S. Yu, D. J. Qiao, Q. J. Xing, S. S. Lau, K. S. Boutros, and J. M. Redwing, Appl. Phys. Lett. **73**, 238 (1998).
55. G. Martin, A. Botchkarev, A. Rockett, and H. Morkoc, Appl. Phys. Lett. **68**, 2541 (1996).
56. G. Martin, S. Strite, A. Botchhaev, A. Agarwal, A. Rockett, H. Markoc, W. R. L. Lambrecht, and B. Segall, Appl. Phys. Lett. **65**, 610 (1994).
57. F. Capasson, in *Gallium Arsenide Technology,* (SAMS, New York, 1985).
58. U. Mishra, Y. Wu, B. Keller, IEEE Trans. Microwave Theory and Techniques **16**, 756 (1998).
59. L. Hsu and W. Walukiewicz, Physical Review B **56**, 1520 (1997).
60. R. Wang, P. Ruden, J. Kolnik and I. Oguzman, J. Phys. Chem. Solids **58**, 913 (1997).
61. S. Tiwari, in *Compound Semiconductro Devices*, (Academic Press, New York, 1992).

62. M. Kurata, in *Numerical Analysis of Semiconductor Devices*, (D. C. Heath, Boston, 1985).

63. N. P. Buslenko and D. I. Golenko, in *The Monte Carlo Method: The Method of Statistical Trials*, (Pergamon Press, Oxford, 1966).

64. N. T. Son, O. Kordina, and A. O. Konstantinov, Appl. Phys. Lett. **65**, 3209 (1994).

65. C. Jacoboni and L. Reggiani, Rev. Mod. Phys. **55**, 645 (1983).

66. E. M. Conwell, Solid State Phys. **6**, 109 (1967).

67. H. G. Reik and H. Risken, Phys. Rev. **126**, 1737 (1962).

68. H. Budd, J. Phys. Soc. Japan **21**, 420 (1966).

69. T. Kurosawa, J. Phys. Soc. Japan **21**, 424 (1966).

70. W. Fawcett, in *Electron in Crystalline Solids,* (International Atomic Energy Agency, Vienna, 1973).

71. A. D. Boardman, in *Physics Programs*, (Wiley, New York, 1980).

72. H. D. Ree, J. Phys. Chem. Solids **30**, 643 (1969).

73. U. Ravaioli, *Ph.D Dissertation*, Arizona State University (1986).

74. A. D. Broadman, W. Fawcett and H. D. Rees, Solid State Commun. **6**, 305 (1968).

75. B. R. Nag, in *Electron Transport in Compound Semiconductors,* (Spring-Verlag, Berlin, 1980).

76. J. M. Hinckley and J. Singh, Appl. Phys. Letts. **53**, 75 (1988).

77. J. Singh, in *Physics of Semiconductors and Heterostructures,* (McGraw Hill, N. York, 1983).

78. K. Seeger, in *Semiconductor Physics,* (Springer-Verlag, Berlin, 1985).

79. E. Fermi, in *Nuclear Physics,* (University of Chicago Press, Chicago, 1950).

80. G. L. Bir and G. E. Pikus, in *Symmetry and Strain-Induced Effects in Semiconductors,* (Wiley, New York, 1974).

81. S. Mori and T. Ando, Phys. Rev. B **19**, 6433 (1979).

82. C. Chang, and F. Kai, in *GaAs High-Speed Devices,* (Wiley, New York, 1994).

83. E. M. Conwell and V. F. Weisskopf, Phys. Rev. **77**, 388 (1950).

84. H. Brooks and C. Herring, Phys. Rev. **83**, 879 (1951).

85. B. K. Ridley, in *Quantum Processes in* Semiconductors (Oxford University Press, Oxford, 1982).

86. F. Stern, CRC Critical Rev. in Solid State Science **4**, 499 (1974); F. Stern and W. E. Howard, Phys. Rev. **163**, 816 (1967).

87. K. Masaki, K. Taniguchi, C. Hamaguchi, and M. Iwase, Jap. J. Appl. Phys. **30**, 2734 (1991).

88. T. Ando, J. Phys. Soc. Jpn. **43**, 1616 (1977).

89. P. Price, Ann. Phys. **133**, 217 (1981).

90. F. Gamiz, J. Roldan, J. Lopez-Villanueva, and J. Carceller, J. Appl. Phys. **69**, 2219 (1996).

91. L. Reggiani, in *Topics in Applied Physics* (Springer-Verlag, Berlin, 1985).

92. R. Brunetti and C. Jacoboni, in *Hot Carriers in Semiconductors*, (Pergamon Press, 1987).

93. B. Doshi, K. F. Brennan, R. Bicknell-Tassius, and F. Grunthaner, Appl. Phys. Lett. 73, 2784 (1998).

94. A. J. Sierakowski and L. F. Eastman, J. Appl. Phys. 86, 3398 (1999).

95. J. Kolník, I. H. Oguzman, K. F. Brennan, R. Wang, P. P. Ruden, and Y. Wang, J. Appl. Phys. **78**, 1033 (1995).

96. A. G. Sabnis and J. T. Clemens, *IEDM Tech. Digest*, pp.18-21, (1979).

97. U. Ravaioli and D. K. Ferry, IEEE Trans. Elec. Dev. **33**, 677 (1986).

98. W. Walukiewicz, H. E. Ruda, J. Lagowski, and H. C. Gatos, Phys. Rev. B. **30**, 4571 (1984).

99. F. F. Fang and W. E. Howard, Phys. Rev. Lett. **16**, 797 (1966).

100. D. K. Ferry, Phys. Rev. B **14**, 1605 (1976).

101. S. Yamakawa, H. Ueno, K. Taniguchi, C. Hamaguchi, K. Miyatsuji, K. Masaki, and U. Ravaioli, J. Appl. Phys. **79**, 911 (1996).

102. Y. Zhang and J. Singh, J. Appl. Phys. **85**, 587 (1999).

103. J. L. Thobel, A. Sleiman, and R. Fauquembergue, J. Appl. Phys. **82**, 1220 (1997); P. Borowik and J. L. Thobel, J. Appl. Phys. **87**, 329 (2000).

104. T. Yamada, H. Miyata, J. R. Zhou, and D. K. Ferry, Phys. Rev. B **49**, 1875 (1994).

105. R. Dimitrov, L. Wittmer, H. P. Felsl, A. Mitchell, O. Ambacher, and M. Stutmann, Phys. Stat. Sol. A **168**, 7 (1998).

106. S. C. Binari, J. M. Redwing, G. Kelner, and W. Kruppa, Electr. Lett. **33**, 242 (1997).

107. C. Nguyen, N. X. Nguyen, M. Le, and D. E. Grider, Electr. Lett. **34**, 309 (1998).

108. L. W. Wong, S. J. Cai, K. Wang, H. W. Jiang, and M. Chen, Appl. Phys. Lett.**73**, 1391 (1998).

109. Y. Fu, K. B. Joelsson, K. J. Grahn, W. X. Ni, G. V. Hansson, and M. Willander, Phys. Rev. B **54**, 11317 (1996).

110. D. E. Grider, N. X. Nguyen, and C. Nguyen, Solid State Electr. **43**, 1473 (1999).

111. S. Rumyantsev, M. E. Levinshtein, R. Gaska, M. S. Shur, A. Khan, J. W. Yang, G. Simin, A. Ping, and T. Adesida, Phys. Stat. Sol. A **176**, 201 (1999).

112. G. J. Sullivan, M. Y. Chen, J. A. Higgins, J. W. Yang, Q. Chen, R. L. Pierson, and B. T. McDermott, IEEE Electr. Dev. Lett. **19**, 198 (1998).

113. E. A. Caridi, T. Y. Chang, K. W. Goosen, and L. F. Eastman, Appl. Phys. Lett. **56**, 659 (1990).

114. A. D. Bykhovski, V. V. Kaminski, M. S. Shur, Q. C. Chen, and M. A. Khan, Appl. Phys. Lett. **68**, 818 (1996).

115. M. J. Bailey, IEEE Transactions on Microwave Theory and Techniques **MTT-48**, 104 (2000).

116. C. Nguyen, N. X. Nguyen, and D. E. Grider, Electr. Lett. **35**, 1380 (1999).

117. For example, M. Schetzen, in *The Volterra and Wiener Theories of Nonlinear Systems,* (Wiley, New York, 1980).

118. J. C. Pedro and N. B. de Carvalho, IEEE Trans. Microwave Theory Tech. **MTT-47**, 2393 (1999).

119. J. A. Higgins and R. L. Kuvas, IEEE Trans. Microwave Theory Tech. **MTT-28**, 9 (1980).

120. A. Van Der Ziel, Proc. IEEE **76**, 233 (1988).

121. E. Yamaguchi, J. Appl. Phys. **56**, 1722 (1984).

122. D. H. Park and K. F. Brennan, J. Appl. Phys. **65**, 615 (1989).

123. K. Brennan and K. Hess, Solid-Sta te Electron. **27**, 347 (1984).

VITA

for

TAO LI

EDUCATION

Ph. D. Electrical Engineering, Old Dominion University, Norfolk, VA

M. S. Electrical Engineering, University of Electronic Science & Technology of China, China

B. S. Electrical Engineering, University of Electronic Science & Technology of China, China

PROFESSIONAL EXPERIENCE

LAN administrator, Old Dominion University, Norfolk, VA (06/00-05/01)

Provided administrative level support. Involved in LAN network organization, development and hardware/software troubleshooting. Also participated the issues pertinent to computer related technical support (Windows/UNIX/Novell) within the ODU campus community.

Research assistant, Old Dominion University, Norfolk, VA (01/99-05/01)

Developed Monte Carlo codes to simulate AlGaN/GaN heterojunctions HEMT.

Research assistant, Institute of Microelectronics at UESTC, Chengdu, China (09/95-06/98)

Applied famous circuits and devices simulation software (MEDICI, SPICE, PISICES) to investigate the characteristics of power devices (CMOS, IGBT).

Computer instructor, Sichuan Computer Application School, China (11/97-05/98)

Provided entry-level computer hardware/software training.

PAPERS PUBLISHED

"Monte Carlo evaluations of degeneracy and interface roughness effects on electron transport in AlGaN-GaN heterojunctions," T. Li, R. P. Joshi, C. Fazi, J. Appl. Phys., 88, 829 (2000)

"Monte Carlo simulation of transient electron transport in bulk GaN and GaN-AlGaN heterojunctions," T. Li, R. P. Joshi, C. Fazi, Proceeding of SPIE, Vol. 39 (Jan., 2000)

"Monte Carlo based analysis of intermodulation distortion behavior in GaN-AlGaN HEMTs for microwave applications," T. Li, R. P. Joshi and C. Fazi, J. Appl. Phys., (Sept., 2001)

The word processor for this thesis was Dr. Tao Li